Deformation along the subduction plate interface above and below the seismogenic zone

Caroline E. Seyler

Department of Earth and Planetary Sciences

McGill University, Montréal

A thesis submitted to McGill University in partial fulfillment of the requirements of the degree of Doctor of Philosophy

December, 2020

ACKNOWLEDGEMENTS

First, I would like to thank Jamie Kirkpatrick for providing excellent guidance throughout my research program, broadening my understanding of rocks, and helping me ask better questions. His encouragement and support made this thesis possible. I would also like to thank my supervisory committee members Yajing Liu and Vincent van Hinsberg for providing valuable insight and interesting scientific discussions. Thanks to my co-authors Heather Savage, Takehiro Hirose, Dan Faulkner, Alexis Licht, Dana Šilerovà, and Christine Regalla for their collaboration. Special thanks to Dana Šilerovà for filling our long field season with laughs, Heather Savage for hosting me during lab visits, and Hannah Rabinowitz for suffering through failed experiments with me. Thanks to the Friends of the Leech River for sharing the best outcrop locations and road maps. Thanks to my duly missed desk neighbors Kelian Dascher-Cousineau and Nick Ogasa for scientific chats and welcomed interruptions. Thanks to Noah Phillips for endless scientific chat, engaging with some of my whackier ideas, and putting up with me through everything. Thanks to Anne Kosowski and all the postdocs, graduate students, and undergraduates in the EPS department that created an incredibly friendly work environment. Finally, thanks to my family for their boundless support and total faith in me.

CONTRIBUTION OF AUTHORS

Unless indicated below, all work presented in this thesis was performed by the author, Caroline E. Seyler.

Dr. Jamie Kirkpatrick: Provided advising, financial support, editorial support, guidance in defining thesis questions, and helped conduct field work.

Dr. Heather Savage: Helped define research questions in chapter 2.

Dr. Takehiro Hirose: Provided laboratory space for conducting rotary shear experiments on Cascadia core samples at the Kochi Institute for Core Sample Research.

Dr. Daniel Faulkner: Conducted rotary shear experiments on individual clay species.

Takahiro Suzuki: Provided training for and assistance with conducting rotary shear experiments at the Kochi Institute for Core Sample Research

Dana Šilerová: Provided field assistance during field work and analyzed a subset of the garnet and biotite compositions.

Dr. Alexis Licht: Analyzed zircon grains for U-Pb geochronology.

Dr. Christine Regalla: Conducted initial field work in the field area.

Lang Shi: Assisted in operation of the scanning electron microscope and electron microprobe at McGill University.

Nicolas Brodusch: Assisted with ion polishing of thin sections for electron backscatter diffraction at McGill University.

ABSTRACT

Subduction zones host the world's largest earthquakes, but seismic slip is only one style of deformation along the subduction interface. The deformation processes above and below the seismogenic zone are equally fundamental to understanding how relative motion is accommodated during subduction. The plate interface updip from the seismogenic zone is commonly localized within seafloor sediments overlying the subducting slab. Whether or not an earthquake propagates through those sediments to the surface controls the likelihood tsunami generation, making the mechanical behavior of seafloor sediments essential to our understanding of shallow earthquake rupture. On the downdip portion below, high temperatures allow continuous sliding that progressively loads the seismogenic zone. This thesis investigates the deformation behavior of the updip and downdip subduction interface through experimental, field, and microstructural studies on the active Cascadia subduction system and an exhumed analog, the Leech River Fault.

At the Cascadia subduction zone, the oceanic Juan de Fuca plate is blanketed by a thick package of sediments with varying clay content, which strongly influences the mechanical properties of fault gouge. To investigate the likelihood of earthquakes rupturing to the surface, high velocity rotary shear experiments were conducted over a range of normal stresses on three samples of Ocean Drilling Program core retrieved from Cascadia input sediments and a suite of individual clay species to measure their frictional properties and fracture energy. The Cascadia input sediment cores show little variation in fracture energy between samples. Clay species were tested under wet and dry conditions, and difference between extremely low fracture energy wet gouges and moderately low fracture energy dry gouges was more significant than the differences between species. Comparing these results with a global compilation of fracture energy estimates, wet clay-

rich gouges have the lowest fracture energy of all lithologies, which may enhance earthquake rupture to the trench. Yet Cascadia sediments have a fracture energy that is nearly an order of magnitude higher than input sediments from other subduction zones, possibly inhibiting shallow earthquake rupture propagation and tsunamigenesis.

The Leech River Fault (LRF) is a terrane-bounding structure on southern Vancouver Island that separates the Late Cretaceous-Paleocene Leech River Schist and the Eocene Metchosin Basalt. My field, petrological, microstructural, and geochronological data rewrite the history of the LRF as a subduction interface shear zone. The shear zone is defined by mylonites developed along the contact between the schist and metamorphosed basalt, whose strong, steeply dipping foliation, downdip lineation, and kinematic indicators indicate sinistral-reverse motion. Garnet and amphibole chemical zoning in the schist and metabasalt, respectively, indicate prograde, syn-kinematic growth. Syn-kinematic metamorphic conditions of ~575 °C and ~800 MPa were determined from the schist mylonite, which match the qualitative P-T conditions of amphibolite facies determined from amphibole rim compositions in the metabasalt mylonite. The structural and metamorphic history of the shear zone confirm that it was active as the downdip portion of the subduction interface.

The strength of the subduction interface downdip is an important parameter for understanding subduction dynamics that cannot be determined geophysically. Integrating microstructural observations of the mylonites with experimentally derived flow laws, I determined the controls on shear zone rheology and estimated bulk rock strength under *in situ* conditions. Multiple deformation mechanisms operating in the schist and metabasalt mylonites were required to accommodate deformation, and the available flow laws indicate that the bulk strength of these rocks was significantly reduced by hydrous phases like phyllosilicates and amphibole. These observations suggest that hydration and metamorphic reactions play an essential role in weakening rocks and allowing the plate interface to creep aseismically at low stresses. Together, these new observations place important constraints on the dynamics of deformation above and below the seismogenic zone.

RÉSUMÉ

Si les plus grands tremblements de terre se produisent dans les zones de subduction, le glissement sismique ne représente qu'un des styles de déformation le long d'interfaces de subduction. Les processus de déformation au-dessus et en dessous de la zone sismogène sont d'importance tout aussi fondamentale pour comprendre comment le déplacement relatif est réparti durant la subduction. L'interface des plaques en amont-pendage de la zone sismogène se trouve généralement dans des sédiments du fond marin reposant sur la plaque subduite. La propagation ou non vers la surface d'un tremblement de terre dans ces sédiments contrôle la probabilité de production de tsunamis, de sorte que le comportement mécanique des sédiments du fond marin est d'importance clé pour comprendre le processus de rupture de séismes peu profonds. Sur la portion en aval-pendage, des températures élevées permettent un glissement continu qui charge progressivement la zone sismogène. Le présent mémoire se penche sur le comportement de déformation de l'interface de subduction en amont-pendage et en aval-pendage de la zone sismogène par l'entremise d'études expérimentales, microstructurales et de terrain portant sur le système de subduction active de Cascadia et sur un analogue exhumé, la faille de Leech River.

Dans la zone de subduction de Cascadia, la plaque de Juan de Fuca est recouverte d'une épaisse séquence de sédiments aux teneurs variables en minéraux argileux qui exercent une forte influence sur les propriétés mécaniques des argiles de faille. Afin d'examiner la probabilité de propagation de la rupture de tremblements de terre jusqu'à la surface, des expériences de cisaillement rotatif à haute vitesse ont été réalisées pour une fourchette de contraintes normales sur trois échantillons de carottes de l'Ocean Drilling Program prélevées de sédiments déposés dans la zone de subduction de Cascadia et sur une série de différents minéraux argileux, afin de mesurer leurs propriétés en

frottement et leur énergie de rupture. Les carottes de sédiments de Cascadia montrent peu de variations entre échantillons en ce qui concerne l'énergie de rupture. Des essais sur les minéraux argileux ont été menés dans des conditions sèches et humides, et la différence entre des argiles de faille humides d'énergie de rupture extrêmement faible et des argiles de faille sèches d'énergie de rupture modérément faible était plus importante que la différence entre différentes minéraux argileux. La comparaison de ces résultats à une compilation planétaire d'estimations de l'énergie de rupture révèle que, de tous les types de roches, les argiles de faille humides riches en minéraux argileux présentent la plus faible énergie de rupture, ce qui pourrait favoriser la propagation de la rupture de tremblements de terre jusqu'à la fosse. Cela dit, les sédiments de Cascadia ont une énergie de rupture de presque un ordre de grandeur supérieure à celle des sédiments d'autres zones de subduction, ce qui pourrait prévenir la propagation de la rupture de tremblements de terre peu profonds et la formation de tsunamis.

La faille de Leech River (LRF) est une structure limitrophe de terranes dans le sud de l'île de Vancouver qui sépare le schiste de Leech River, d'âge crétacé tardif-paléocène, du basalte éocène de Metchosin. Mes données pétrologiques, microstructurales, géochronologiques et de terrain redéfinissent l'histoire de la LRF en tant que zone de cisaillement d'interface de subduction. La zone de cisaillement est définie par des mylonites formées le long du contact entre le schiste et le basalte métamorphosé, dont la foliation marquée fortement inclinée, la linéation parallèle au pendage et les indicateurs cinématiques indiquent un déplacement inverse-senestre. La zonation chimique des grenats et amphiboles dans le schiste et le métabasalte, respectivement, témoigne de leur croissance syncinématique prograde. Des conditions métamorphiques syncinématiques de ~575°C et ~800 MPa ont été obtenues pour le schiste mylonitisé, qui correspondent aux conditions de P-T qualitatives du faciès des amphibolites obtenues à partir de la composition des bordures d'amphiboles dans le métabasalte mylonitisé. L'histoire structurale et métamorphique de la zone de cisaillement confirme que cette dernière était active et formait la partie aval-pendage de l'interface de subduction.

La résistance de l'interface de subduction en aval-pendage est un paramètre d'importance pour la compréhension de la dynamique de subduction, qui ne peut toutefois être déterminé par des méthodes géophysiques. En intégrant des observations microstructurales sur les mylonites à des lois de fluage obtenues de manière expérimentale, j'ai cerné les facteurs qui contrôlent la rhéologie de la zone de cisaillement et estimé la résistance volumique des roches dans les conditions *in situ*. Différents mécanismes de déformation ont dû intervenir dans les schistes et basaltes mylonitisés pour permettre la déformation, et les lois de fluage disponibles indiquent que des phases hydratées comme des phyllosilicates ou des amphiboles ont causé une réduction significative de la résistance volumique de ces roches. Ces observations donnent à penser que l'hydratation et les réactions métamorphiques jouent un rôle central en réduisant la résistance des roches et en permettant à l'interface des plaques de fluer de manière asismique sous de faibles contraintes. Collectivement, ces nouvelles observations définissent d'importantes contraintes régissant la dynamique de la déformation au-dessus ou en dessous de la zone sismogène.

TABLE OF CONTENTS

LIST OF FIGURES

LIST OF TABLES

CITATIONS TO PREVIOUSLY PUBLISHED WORK

Chapter 2 is based on the following paper:

Seyler, C. E., Kirkpatrick, J. D., Savage, H. M., Hirose, T., Faulkner, D. R., 2020. Rupture to the trench? Frictional properties and fracture energy of incoming sediments at the Cascadia subduction zone. *Earth and Planetary Science Letters*, 546, 116413, https://doi.org/10.1016/j.epsl.2020.116413

CHAPTER 1

Introduction

1.1 Mechanical behavior in subduction zones

Subduction of oceanic lithosphere drives plate tectonics (Bercovici, 2003; Chapple and Tullis, 1977; Forsyth and Uyeda, 1975; Schellart, 2004) and causes the world's largest earthquakes, which produce devastating releases of radiated seismic energy. Seismic slip on subduction faults accounted for approximately 90% of the seismic moment released in the 20th century (Pacheco and Sykes, 1992) and 90-95% of all tsunamis (Bilek and Lay, 2018). Yet, earthquake rupture is only one of many styles of deformation along the subduction plate interface, and the behavior above and below the seismogenic zone is essential to understanding how relative plate motion is accommodated at plate boundaries and for constructing better seismic hazard models.

Deformation and slip style are controlled by the constitutive behavior of the plate interface, which varies with mineralogy, temperature, pressure, and fluid conditions as rocks at the interface evolve downdip during progressive deformation and metamorphism (e.g., Lay et al., 2012). At subduction zones, deformation along the plate interface is divided into three regimes: aseismic slip updip, seismic slip within the seismogenic zone, and aseismic slip downdip. These regimes are based on the distribution of earthquakes (Sibson, 1982) and depth of interplate locking as measured from surface deformation (e.g., Hyndman and Wang, 1995; Wallace et al., 2004), which define the seismogenic zone. Temperature is hypothesized to control the deformation style within each regime (Hyndman and Wang, 1993; Oleskevich et al., 1999). The updip limit of the seismogenic zone occurs at ~100-150 °C due to changes in frictional properties and increasing pore pressure during the onset of diagenesis and dewatering of clay minerals. The downdip limit transitions to ductile creep between ~300-350 °C (quartz) and 450°C (feldspar) due to the onset of crystal plastic deformation. The depth of these transitions depends on the geothermal gradient at the subduction zone, which is controlled by age of the oceanic plate, plate convergence rate, thickness of sediment cover, subduction dip angle, and thermal properties of the overlying accretionary prism (Hyndman and Wang, 1995). However, the importance of these thermal constraints on deformation style are still debated (Fagereng and Ellis, 2009; Hyndman, 2007).

In the updip and downdip aseismic slip regimes, the plate interface continuously creeps at near-tectonic rates either through stable frictional sliding on the shallow megathrust or viscous deformation at depth (Scholz, 1998). In the seismogenic zone, the plate interface does not slip between earthquakes, instead accumulating elastic strain energy due to loading by continuous slip in the creeping regimes updip and downdip, which is released during unstable seismic slip (stick-slip behavior). At the transition between these stable and unstable regimes, there is a zone of conditional stability where transitional behavior arises (Scholz, 1998). This transitional behavior exhibits a spectrum of slip rates between earthquake slip and aseismic creep that have been identified on subduction interfaces in the last few decades, collectively termed slow earthquakes (Ide et al., 2007; Jolivet and Frank, 2020; Peng and Gomberg, 2010; Schwartz and Rokosky, 2007).

Earthquake propagation into the aseismic zone updip also constitutes a type of conditional stability. Continuous slip on the shallow plate interface updip should preclude seismic slip (Avouac, 2015), but large amounts of coseismic slip on the shallow subduction interface during the 2004 Sumatra (Bletery et al., 2016; Lay et al., 2005) and 2011 Tohoku-Oki (Ide et al., 2011; Lay, 2018) megathrust earthquakes demonstrate the possibility of rupture propagation and large coseismic slip in the updip portion of subduction zones. Numerical modeling explains the unexpected shallow slip with a velocity-dependent transition from stable, creeping behavior at low slip rates to dynamic weakening and unstable behavior at coseismic slip rates (Noda and Lapusta, 2013). Experimental studies postulate that the low shear stress during coseismic slip (Ujiie et al., 2013) and extremely low fracture energy (Sawai et al., 2014) of clay-rich fault gouge likely present along the shallow interface allowed rupture propagation to the trench. Given the seismic and tsunami hazard of shallow coseismic slip, more work is needed to measure the fracture energy of fault gouges at other subduction margins and evaluate the potential for rupture to the trench.

Downdip from the seismogenic zone, aseismic creep loads the seismogenic megathrust, sets the maximum size of megathrust earthquakes (e.g., Hyndman, 2013), and accommodates a spectrum of slip rates (e.g., Peng and Gomberg, 2010). Despite its importance, the rheology of the downdip plate interface is poorly constrained due to the scarcity of deeply exhumed examples. Instead, it is often approximated by dislocation creep in quartz, then olivine at depths below the crust-mantle boundary (e.g., Bürgmann and Dresen, 2008; Kohlstedt et al., 1995). However, subduction interface shear zones contain metasedimentary and metamafic lithologies composed of multiple mineral phases, and recent work has shown that metamorphosed oceanic basalts play an important role in determining plate interface rheology over a range of depths (Kotowski and Behr, 2019; Phillips et al., 2020; Tulley et al., 2020). Further constraints from natural examples of plate interface shear zones are needed to provide better insight to the deformation processes at depth in subduction zones.

1.2 Earthquake energy budget

Earthquake slip is a frictional instability, which develops when the strength of a fault diminishes more rapidly than the tectonic forces that are loading the system are relaxed. During an earthquake, the elastic strain energy stored during tectonic loading is released and dissipated as radiated energy (i.e., seismic waves), thermal energy (i.e., frictional heating), and fracture energy. The earthquake energy budget describes the partitioning of energy between these energy sinks during earthquake slip.

The slip weakening model is widely used to represent the earthquake rupture process and relate the macro-scale energy budget of an earthquake to the physical processes controlling the strength of the slipping fault (Fig. 1-1; Andrews, 1976; Kanamori and Rivera, 2006). In the slip weakening model, slip is initiated when the static strength of the fault is exceeded by the tectonic load. As slip progresses, the strength of the fault decreases to a steady-state dynamic value and remains at that value until the driving forces are relaxed to levels below the dynamic shear strength of the fault and slip stops. The rate of strength decrease is characterized by a critical amount of slip, the slip-weakening distance (D_c). Strength decrease is facilitated by slip weakening mechanisms, such as thermal pressurization and melt lubrication, which are thermally activated mechanisms that reduce the resistance to shear (Di Toro et al., 2011). To achieve the physical breakdown in strength of a fault, an energy input is required to break material bonds and create a rupture surface. This energy is the fracture energy, E_G. Seismological and geological definitions of fracture energy encompass the dissipative processes at and around the rupture tip, such as the formation of cracks, making fracture energy a material property that dictates the relative difficulty

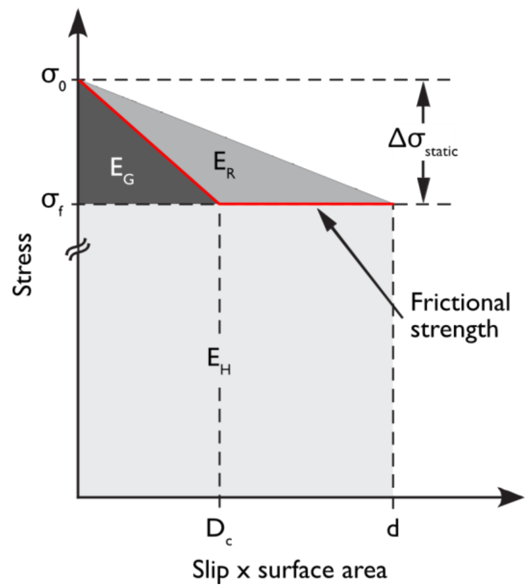

Figure 1-1: Earthquake energy budget. The upper boundary of the shaded regions represents the stress decrease from the initial strength of the fault (σ_0) to the final fictional strength (σ_f) during earthquake slip. Shaded regions represent the partitioning of energy between fracture energy (E_G), radiated energy (E_R), and frictional heating (E_H) (adapted from Chester et al., 2005).

of rupture propagation and controls the local accelerations on a fault plane (Cocco and Tinti, 2008; Kanamori and Rivera, 2006). The energy budget of a fault (E_T) is thus partitioned as $E_T = \Delta W = E_R + E_H + E_G$, where E_R is the radiated energy and E_H is the energy dissipated as heat on the fault plane.

1.3 Rheology from natural rocks

Deformation mechanisms control the rheology of rocks during continuous, viscous deformation, which is applicable to the downdip portion of the plate interface, dictating its slip behavior and its strength. At a given set of environmental conditions (i.e., pressure, temperature, strain rate, fluid chemistry, pore pressure, water fugacity, grain size, etc.) a material will deform by the deformation mechanism that requires the least amount of stress. Generally, deformation evolves from frictional sliding (brittle) to crystal plasticity (ductile) with increasing temperature and pressure and/or strain rate (e.g., Kohlstedt et al., 1995). Deformation mechanisms can be evaluated from characteristic microstructures observed with optical, scanning, and transmission electron microscopy and fabric analysis (e.g., electron backscatter diffraction). For example, dynamic recrystallization of quartz during dislocation creep produces distinctive grain boundary morphologies, subgrain structures, and strong lattice preferred orientations (LPO) (e.g., Hirth and Tullis, 1992; Stipp et al., 2002). These deformation mechanisms can then be translated to rheology through the extrapolation of experimentally derived constitutive laws.

Rock rheology is described by constitutive laws (i.e., flow laws) that relate stress and strain rate and have the generalized form of an Arrhenius equation

$$\dot{\varepsilon} = A\sigma^n {f_{H2O}}^r d^m \exp\left({}^{-Q}/_{RT}\right) \qquad (1-1)$$

where $\dot{\varepsilon}$ is strain rate (s^{-1}), A is an empirical constant, σ is the differential stress (MPa), n is the stress exponent, f_{H2O} is the fugacity of water (MPa), r is the fugacity exponent, d is the grain size (µm), m is the grain size exponent, Q is the activation energy (J mol^{-1}), R is the gas constant (J mol^{-1} K^{-1}), and T is temperature (K) (Paterson, 2013). To convert flow laws into plane strain, the prefactor A must be multiplied by $\frac{1}{2}(3^{(n+1)/2})$ (Tullis et al., 1991). These laws are constructed from experiments on a single mineral or lithology deforming via a specific deformation mechanism. For dislocation creep, dislocation mobility accommodates strain as dislocations slip along crystallographic planes and volume diffusion allows dislocations to move across planes (i.e., dislocation climb), the power law exponent is expected to be n > 3, and there is no dependence on grain size (m = 0) (e.g., Hirth et al., 2001). For dislocation glide, dislocations are able to slip along crystallographic planes, but are unable to climb due either to a lack of slip systems in the crystal structure or low temperatures insufficient for volume diffusion (e.g., Kronenberg et al., 1990; Paterson, 2013). For diffusion creep, the power law exponent is n = 1 and there is a dependence on grain size ($m \geq 1$) (e.g., Rutter and Brodie, 2004).

Application of flow laws to natural systems to estimate rock strength requires independent constraints on input variables, which typically include pressure, temperature, activity of water, strain rate, and grain size. For polymineralic rocks, bulk strength can be approximated with mixing laws that combine flow laws for individual minerals (Handy, 1994; Tullis et al., 1991). Bulk strength also depends on the strength contrast between strong and weak phases and the degree of interconnection on stress and strain rate partitioning, i.e., whether the microstructure is best described as a load-bearing framework or controlled by an interconnected weak phase (Handy, 1994; Holyoke and Tullis, 2006).

1.4 Study area: the Cascadia subduction zone and an ancient analog

The Cascadia subduction zone, where the Juan de Fuca plate subducts beneath North America, is a hot subduction endmember (Peacock, 1996; Penniston-Dorland et al., 2015) that regularly hosts slow earthquakes (Bartlow, 2020; Gomberg and Group, 2010; Rogers and Dragert, 2003) and large, tsunamigenic earthquakes (Adams, 1990; Atwater and Hemphill-Haley, 1997; Goldfinger et al., 2003; Goldfinger et al., 2012; Leonard et al., 2010). The last large magnitude event ($M_w \sim$ 9.0) occurred in 1700 A.D. and ruptured 1100 km along the margin (Satake et al., 2003). A large magnitude event today would produce devastating releases of seismic energy and potentially trigger tsunami waves, resulting in billions of dollars of damage and thousands of fatalities (Cascadia Region Earthquake Workgroup, 2013). Geodetic measurements indicate strain

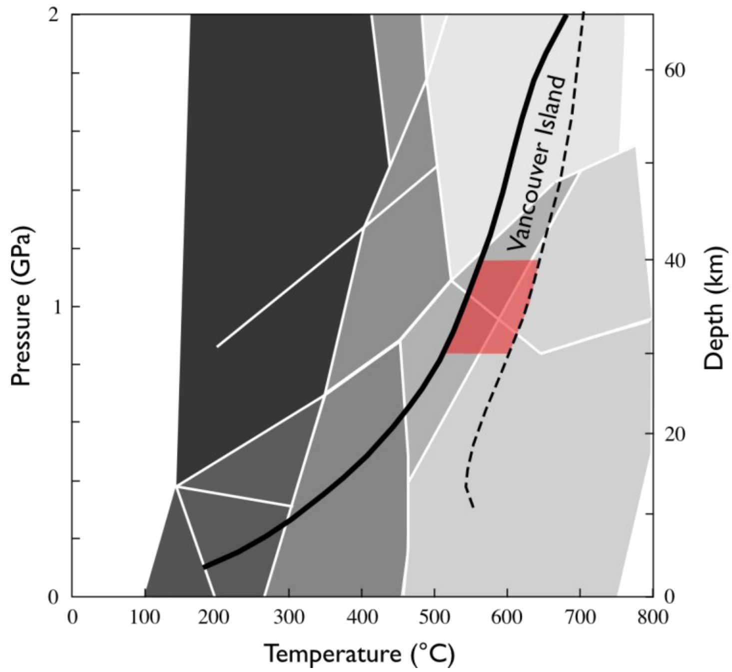

Figure 1-2: Thermal model of the Cascadia subduction zone. Solid and dashed black lines are the modeled P-T conditions of the top and base of the subducting oceanic crust, respectively. Shaded fields correlate to metamorphic facies predicted for metamafic rocks. Red box represents the region downdip from the seismogenic zone (adapted from Peacock, 2009).

accumulation consistent with locking of the seismogenic zone (Dragert et al., 1994; McCaffrey et al., 2013; McCaffrey et al., 2007; Savage et al., 1981). However, the mechanical behavior of the shallow portion of the subduction zone is not well understood. Few earthquake hypocenters are located updip (McGuire et al., 2018), and the oceanic crust at the trench is young and overlain by a ~2 km-thick section of sedimentary rocks resulting in temperature estimates of ~200 °C on the plate interface at the trench (Oleskevich et al., 1999). This implies that the seismogenic zone extends to the trench, but frictional controls on the potential for very shallow seismic slip are untested.

The Leech River Fault (LRF) in the Cascadia forearc on Vancouver Island possibly represents a suitable analog for the downdip portion of the Cascadia subduction zone. The LRF is a terrane boundary juxtaposing the Leech River Complex (Fairchild and Cowan, 1982; Groome et al., 2003) and the Metchosin Igneous Complex (Massey, 1986; Timpa et al., 2005). The Leech River Complex is comprised of a package of pelitic to psammitic near-trench sediments, and the Metchosin Igneous Complex represents an oceanic pseudostratigraphy interpreted as an underplated portion of an oceanic plateau (Phillips et al., 2017; Wells et al., 2014). Previously reported amphibolite facies metamorphism of the Leech River Complex near the terrane boundary matches the ~550 °C temperatures at the downdip transition of the seismogenic zone in Cascadia (Fig. 1-2; Peacock, 2009). The configuration of the fault, with submarine sedimentary rocks thrust over oceanic crust, suggests the fault was a subduction thrust, but previous work has emphasized a strike-slip component to the fault kinematics (Fairchild and Cowan, 1982). Establishing the tectonic context of the LRF is a priority as it will allow future work to interrogate the strength and rheology of a paleo-subduction interface.

1.5 Thesis outline

This thesis is composed of three chapters that investigate deformation along the subduction plate interface above and below the seismogenic zone. In Chapter 2, the high velocity frictional behavior of sediments from the Cascadia subduction margin is tested with rotary shear experiments and compared with the behavior of individual clay species and a compilation of high velocity experimental data. These are the first measurements of frictional properties for subduction materials from northern Cascadia. This chapter also contains the first global compilation of high velocity experiments focusing on clay-bearing fault gouge, the material that best represents the shallow subduction interface. I find that the sediments from Cascadia have the largest fracture energy relative to other subduction zones, which may inhibit dynamic overshoot during the next large earthquake. Chapter 2 is published in Earth & Planetary Science Letters.

Chapter 3 presents a study of the terrane-bounding shear zone between the Leech River Complex and the Metchosin Igneous Complex. I combine field, microstructural, and geochronological datasets to construct a new tectonic interpretation for the "Leech River Shear Zone" (LRSZ), the ancient structure that predates recent fault activity on the LRF. I conclude that the LRSZ is an exhumed subduction interface. This study focuses on deformation and metamorphism of the Leech River Schist and Metchosin Basalt mylonites that define the shear zone. This chapter also establishes the geologic setting for the microstructural study of deformation mechanisms undertaken in the next chapter. Chapter 3 is in preparation for submission to Tectonics.

Chapter 4 investigates the grain-scale deformation mechanisms operating within the mylonites of the LRSZ to estimate the strength of a subduction plate interface. Using microstructural evidence and available flow laws, I determine the dominant deformation mechanism for each constituent mineral phase in the schist and metabasalt mylonites and estimate the bulk strength of the shear zone. These results provide an endmember constraint for hot subduction (i.e., geothermal gradients of ~20 °C/km). Chapter 4 is in preparation for submission to Earth & Planetary Science Letters.

Together, this work investigates the deformation processes above and below the seismogenic zone to provide new rheological constraints on the subduction interface. Constraints on the high velocity frictional behavior of sediments from Cascadia and on the strength of the deep plate interface will prove useful in seismic and tsunami hazard modeling and numerical modeling of subduction dynamics, respectively.

1.6 References

Adams, J., 1990. Paleoseismicity of the Cascadia Subduction Zone: Evidence from turbidites off the Oregon-Washington Margin. Tectonics 9, 569-583. https://doi.org/10.1029/TC009i004p00569.

Andrews, D.J., 1976. Rupture propagation with finite stress in antiplane strain. J. Geophys. Res. 81, 3575-3582. https://doi.org/10.1029/JB081i020p03575.

Atwater, B.F., Hemphill-Haley, E., 1997. Recurrence Intervals for Great Earthquakes of the Past 3,500 Years at Northeastern Willapa Bay, Washington. U.S. Geological Survey, p. 108.

Avouac, J.-P., 2015. From geodetic imaging of seismic and aseismic fault slip to dynamic modeling of the seismic cycle. Annual Review of Earth and Planetary Sciences 43, 233-271. https://doi.org/10.1146/annurev-earth-060614-105302.

Bartlow, N., 2020. A long-term view of episodic tremor and slip in Cascadia. Geophys. Res. Lett. 47, e2019GL085303. https://doi.org/10.1029/2019GL085303.

Bercovici, D., 2003. The generation of plate tectonics from mantle convection. Earth Planet. Sci. Lett. 205, 107-121. https://doi.org/10.1016/S0012-821X(02)01009-9.

Bilek, S.L., Lay, T., 2018. Subduction zone megathrust earthquakes. Geosphere 14, 1468-1500. https://doi.org/10.1130/GES01608.1.

Bletery, Q., Sladen, A., Jiang, J., Simons, M., 2016. A Bayesian source model for the 2004 great Sumatra-Andaman earthquake. J. Geophys. Res. Solid Earth 121, 5116-5135. https://doi.org/10.1002/2016JB012911.

Bürgmann, R., Dresen, G., 2008. Rheology of the lower crust and upper mantle: Evidence from rock mechanics, geodesy, and field observations. Annual Review of Earth and Planetary Sciences 36, 531-567. https://doi.org/10.1146/annurev.earth.36.031207.124326.

Cascadia Region Earthquake Workgroup, 2013. Cascadia Subduction Zone Earthquakes: A Magnitude 9.0 Earthquake Scenario, pp. 1-30.

Chapple, W.M., Tullis, T.E., 1977. Evaluation of the forces that drive the plates. J. Geophys. Res. 82, 1967-1984. https://doi.org/10.1029/JB082i014p01967.

Chester, J.S., Chester, F., Kronenberg, A.K., 2005. Fracture surface energy of the Punchbowl fault, San Andreas system. Nature 437, 133-136. https://doi.org/10.1038/nature03942.

Cocco, M., Tinti, E., 2008. Scale dependence in the dynamics of earthquake propagation: Evidence from seismological and geological observations. Earth Planet. Sci. Lett. 273, 123-131. https://doi.org/10.1016/j.epsl.2008.06.025.

Di Toro, G., Han, R., Hirose, T., De Paola, N., Nielsen, S., Mizoguchi, K., Ferri, F., Cocco, M., Shimamoto, T., 2011. Fault lubrication during earthquakes. Nature 471, 494-498. https://doi.org/10.1038/nature09838.

Dragert, H., Hyndman, R., Rogers, C., Wang, K., 1994. Current deformation and the with of the seismogenic zone of the northern Cascadia subduction thrust. J. Geophys. Res. Solid Earth 99, 653-668. https://doi.org/10.1029/93JB02516.

Fagereng, Å., Ellis, S., 2009. On factors controlling the depth of interseismic coupling on the Hikurangi subduction interface, New Zealand. Earth Planet. Sci. Lett. 278, 120-130. https://doi.org/10.1016/j.epsl.2008.11.033.

Fairchild, L.H., Cowan, D.S., 1982. Structure, petrology, and tectonic history of the Leech River complex northwest of Victoria, Vancouver Island. Can. J. Earth Sci. 19, 1817-1835. https://doi.org/10.1139/e82-161.

Forsyth, D., Uyeda, S., 1975. On the relative importance of the driving forces of plate motion. Geophys. J. Int. 43, 163-200. https://doi.org/10.1111/j.1365-246X.1975.tb00631.x.

Goldfinger, C., Nelson, C.H., Johnson, J.E., 2003. Holocene earthquake records from the Cascadia Subduction Zone and Northern San Andreas Fault based on precise dating of offshore turbidites. Annual Review of Earth and Planetary Sciences 31, 555-577. https://doi.org/10.1146/annurev.earth.31.100901.141246.

Goldfinger, C., Nelson, C.H., Morey, A.E., Johnson, J.E., Patton, J.R., Karabanov, E., Gutierrez-Pastor, J., Eriksson, A., Gracia, E., Dunhill, G., Enkin, R., Dallimore, A., Vallier, T., 2012. Turbidite Event History - Methods and Implications for Holocene Paleoseismicity of the Cascadia Subduction Zone. U.S. Geological Survey, p. 170.

Gomberg, J., Group, C.a.B.W., 2010. Slow-slip phenomena in Cascadia from 2007 and beyond: A review. Geol. Soc. Am. Bull. 122, 963-978. https://doi.org/10.1130/B30287.1.

Groome, W.G., Thorkelson, D.J., Friedman, R.M., Mortensen, J.K., Massey, N.W.D., Marshall, D.D., Layer, P.W., 2003. Magmatic and tectonic history of the Leech River Complex, Vancouver Island, British Columbia: Evidence for ridge-trench intersection and accretion of the Crescent Terrane. Special Papers-Geological Society of America 371, 327-353. https://doi.org/10.1130/0-8137-2371-X.327.

Handy, M.R., 1994. Flow laws for rocks containing two non-linear viscous phases: a phenomenological approach. J. Struct. Geol. 16, 287-301. https://doi.org/10.1016/0191-8141(94)90035-3.

Hirth, G., Teyssier, C., Dunlap, W.J., 2001. An evaluation of quartzite flow laws based on comparisons between experimentally and naturally deformed rocks. Int. J. Earth Sci. 90, 77-87. https://doi.org/10.1007/s005310000152.

Hirth, G., Tullis, J., 1992. Dislocation creep regimes in quartz aggregates. J. Struct. Geol. 14, 145-159. https://doi.org/10.1016/0191-8141(92)90053-Y.

Holyoke, C.W., Tullis, J., 2006. Mechanisms of weak phase interconnection and the effects of phase strength contrast on fabric development. J. Struct. Geol. 28, 621-640. https://doi.org/10.1016/j.jsg.2006.01.008.

Hyndman, R., 2007. The seismogenic zone of subduction thrust faults: what we know and don't know, in: Dixon, T.H., Moore, J.C. (Eds.), The Seismogenic Zone of Subduction Thrust Faults. Colombia University Press, New York, pp. 15-41.

Hyndman, R.D., 2013. Downdip landward limit of Cascadia great earthquake rupture. J. Geophys. Res. Solid Earth 118, 5530-5549. https://doi.org/10.1002/jgrb.50390.

Hyndman, R.D., Wang, K., 1993. Thermal constraints on the zone of major thrust earthquake failure: The Cascadia Subduction Zone. J. Geophys. Res. Solid Earth 98, 2039-2060. https://doi.org/10.1029/92JB02279.

Hyndman, R.D., Wang, K., 1995. The rupture zone of Cascadia great earthquakes from current deformation and the thermal regime. J. Geophys. Res. Solid Earth 100, 22133-22154. https://doi.org/10.1029/95JB01970.

Ide, S., Baltay, A., Beroza, G.C., 2011. Shallow dynamic overshoot and energetic deep rupture in the 2011 Mw 9.0 Tohoku-Oki earthquake. Science 332, 1426-1429. https://doi.org/10.1126/science.1207020.

Ide, S., Beroza, G.C., Shelly, D.R., Uchide, T., 2007. A scaling law for slow earthquakes. Nature 447, 76-79. https://doi.org/10.1038/nature05780.

Jolivet, R., Frank, W.B., 2020. The transient and intermittent nature of slow slip. AGU Advances 1, e2019AV000126. https://doi.org/10.1029/2019AV000126.

Kanamori, H., Rivera, L., 2006. Energy partitioning during an earthquake, in: Abercrombie, R., McGarr, A., Di Toro, G., Kanamori, H. (Eds.), Earthquakes: Radiated Energy and the Physics of Faulting. American Geophysical Union, Washington, D.C., pp. 3-13.

Kohlstedt, D.L., Evans, B., Mackwell, S.J., 1995. Strength of the lithosphere: Constraints imposed by laboratory experiments. J. Geophys. Res. Solid Earth 100, 17587-17602. https://doi.org/10.1029/95JB01460.

Kotowski, A.J., Behr, W.M., 2019. Length scales and types of heterogeneities along the deep subduction interface: Insights from exhumed rocks on Syros Island, Greece. Geosphere 15, 1038-1065. https://doi.org/10.1130/GES02037.1.

Kronenberg, A.K., Kirby, S.H., Pinkston, 1990. Basal slip and mechanical anisotropy of biotite. J. Geophys. Res. Solid Earth 95, 19257-19278. https://doi.org/10.1029/JB095iB12p19257.

Lay, T., 2018. A review of the rupture characteristics of the 2011 Tohoku-oki Mw 9.1 earthquake. Tectonophysics 733, 4-36. https://doi.org/10.1016/j.tecto.2017.09.022.

Lay, T., Kanamori, H., Ammon, C.J., Koper, K.D., Hutko, A.R., Ye, L., Yue, H., Rushing, T.M., 2012. Depth-varying rupture properties of subduction zone megathrust faults. J. Geophys. Res. Solid Earth 117, B04311. https://doi.org/10.1029/2011JB009133.

Lay, T., Kanamori, H., Ammon, C.J., Nettles, M., Ward, S.N., Aster, R.C., Beck, S.L., Bilek, S.L., Brudzinski, M.R., Butler, R., DeShon, H.R., Ekström, G., Satake, K., Sipkin, S., 2005. The

Great Sumatra-Anadaman Earthquake of 26 December 2004. Science 308, 1127-1133. https://doi.org/10.1126/science.1112250.

Leonard, L.J., Currie, C.A., Mazzotti, S., Hyndman, R.D., 2010. Rupture area and displacement of past Cascadia great earthquakes from coastal coseismic subsidence. Geol. Soc. Am. Bull. 122, 2079-2096. https://doi.org/10.1130/B30108.1.

Massey, N.W.D., 1986. Metchosin Igneous Complex, southern Vancouver Island: Ophiolite stratigraphy developed in an emergent island setting. Geology 14, 602-605. https://doi.org/10.1130/0091-7613(1986)14%3C602:MICSVI%3E2.0.CO;2.

McCaffrey, R., King, R.W., Payne, S.J., Lancaster, M., 2013. Active tectonics of northwestern U.S. inferred from GPS-derived surface velocities. J. Geophys. Res. Solid Earth 118, 709-723. https://doi.org/10.1029/2012JB009473.

McCaffrey, R., Qamar, A.I., King, R.W., Wells, R., Khazaradze, G., Williams, C.A., Stevens, C.W., Vollick, J.J., Zwick, P.C., 2007. Fault locking, block rotation and crustal deformation in the Pacific Northwest. Geophys. J. Int. 169, 1315-1340. https://doi.org/10.1111/j.1365-246X.2007.03371.x.

McGuire, J.J., Collins, J.A., Davis, E., Becker, K., Heesemann, M., 2018. A lack of dynamic triggering of slow slip and tremor indicates that the shallow Cascadia megathrust offshore Vancouver Island is likely locked. Geophys. Res. Lett. 45, 1-9. https://doi.org/10.1029/2018GL079519.

Noda, H., Lapusta, N., 2013. Stable creeping fault segments can become destructive as a result of dynamic weakening. Nature 493, 518-521. https://doi.org/10.1038/nature11703.

Oleskevich, D.A., Hyndman, R.D., Wang, K., 1999. The updip and downdip limits to great subduction earthquakes: Thermal and structural models of Cascadia, south Alaska, SW

Japan, and Chile. J. Geophys. Res. Solid Earth 104, 14965-14991. https://doi.org/10.1029/1999JB900060.

Pacheco, J.F., Sykes, L.R., 1992. Seismic moment catalog of large shallow earthquakes, 1900 to 1989. Bull. Seismol. Soc. Am. 82, 1306-1349.

Paterson, M.S., 2013. Materials Science for Structural Geology. Springer, Berlin.

Peacock, S.M., 1996. Thermal and petrologic structure of subduction zones, in: Bebout, G.E., Scholl, D.W., Kirby, S.H., Platt, J.P. (Eds.), Subduction: Top to Bottom. Geophysical Monograph Series, pp. 119-133.

Peacock, S.M., 2009. Thermal and metamorphic environment of subduction zone episodic tremor and slip. J. Geophys. Res. Solid Earth 114, B00A07. https://doi.org/10.1029/2008JB005978.

Peng, Z., Gomberg, J., 2010. An integrated perspective of the continuum between earthquakes and slow-slip phenomena. Nat. Geosci. 3, 599-607. https://doi.org/10.1038/ngeo940.

Penniston-Dorland, S.C., Kohn, M.J., Manning, C.E., 2015. The global range of subduction zone thermal structures from exhumed blueschists and eclogites: Rocks are hotter than models. Earth Planet. Sci. Lett. 428, 243-254. http://doi.org/10.1016/j.epsl.2015.07.031.

Phillips, B.A., Kerr, A.C., Mullen, E.K., Weis, D., 2017. Oceanic mafic magmatism in the Siletz terrane, NW North America: Fragments of an Eocene oceanic plateau? Lithos 274-275, 291-303. https://doi.org/10.1016/j.lithos.2017.01.005.

Phillips, N.J., Motohashi, G., Ujiie, K., Rowe, C.D., 2020. Evidence of localized failure along altered basaltic blocks in tectonic mélange at the updip limit of the seismogenic zone: Implications for the shallow slow earthquake source. Geochem. Geophys. Geosyst. 21, e2019GC008839. https://doi.org/10.1029/2019GC008839.

Rogers, G., Dragert, H., 2003. Episodic tremor and slip on the Cascadia subduction zone: The chatter of silent slip. Science 300, 1942-1943. https://doi.org/10.1126/science.1084783.

Rutter, E.H., Brodie, K.H., 2004. Experimental grain size-sensitive flow of hot-pressed Brazilian quartz aggregates. J. Struct. Geol. 26, 2011-2023. https://doi.org/10.1016/j.jsg.2004.04.006.

Satake, K., Wang, K., Atwater, B.F., 2003. Fault slip and seismic moment of the 1700 Cascadia earthquake inferred from Japanese tsunami descriptions. J. Geophys. Res. Solid Earth 108, 2535. https://doi.org/10.1029/2003JB002521.

Savage, J.C., Lisowski, M., Prescott, W.H., 1981. Geodetic strain measurements in Washington. J. Geophys. Res. Solid Earth 86, 4929-4940. https://doi.org/10.1029/JB086iB06p04929.

Sawai, M., Hirose, T., Kameda, J., 2014. Frictional properties of incoming pelagic sediments at the Japan Trench: implications for large slip at a shallow plate boundary during the 2011 Tohoku earthquake. Earth Planets Space 66, 65. https://doi.org/10.1186/1880-5981-66-65.

Schellart, W.P., 2004. Quantifying the net slab pull force as a driving mechanism for plate tectonics. Geophys. Res. Lett. 31, L07611. https://doi.org/10.1029/2004GL019528.

Scholz, C.H., 1998. Earthquakes and friction laws. Nature 391, 37-42. https://doi.org/10.1038/34097.

Schwartz, S.Y., Rokosky, J.M., 2007. Slow slip events and seismic tremor at circum-Pacific subduction zones. Reviews of Geophysics 45, 1-32. https://doi.org/10.1029/2006RG000208.

Sibson, R.H., 1982. Fault zone models, heat flow, and the depth distribution of earthquakes in the continental crust of the United States. Bull. Seismol. Soc. Am. 72, 151-163.

Stipp, M., Stünitz, H., Heilbronner, R., Schmid, S.M., 2002. The eastern Tonale fault zone: A 'natural laboratory' for crystal plastic deformation of quartz over a temperature range from 250 to 700 ˚C. J. Struct. Geol. 24, 1861-1884. https://doi.org/10.1016/S0191-8141(02)00035-4.

Timpa, S., Gillis, K.M., Canil, D., 2005. Accretion-related metamorphism of the Metchosin Igneous Complex, southern Vancouver Island, British Columbia. Can. J. Earth Sci. 42, 1467-1479. https://doi.org/10.1139/e05-043.

Tulley, C.J., Fagereng, Å., Ujiie, K., 2020. Hydrous oceanic crust hosts megathrust creep at low shear stresses. Sci. Adv. 6, eaba1529. https://doi.org/10.1126/sciadv.aba1529.

Tullis, T., Horowitz, F.G., Tullis, J., 1991. Flow laws of polyphase aggregates from end-member flow laws. J. Geophys. Res. Solid Earth 96, 8081-8096. https://doi.org/10.1029/90JB02491.

Ujiie, K., Tanaka, H., Saito, T., Tsutsumi, A., Mori, J.J., Toczko, S., Scientists, E.a.T., 2013. Low coseismic shear stress on the Tohoku-Oki megathrust determined from laboratory experiments. Science 342, 1211-1214. https://doi.org/10.1126/science.1243485.

Wallace, L., Beavan, J., McCaffrey, R., Darby, D., 2004. Subduction zone coupling and tectonic block rotations in the North Island, New Zealand. J. Geophys. Res. Solid Earth 109, B12406. https://doi.org/10.1029/2004JB003241.

Wells, R., Bukry, D., Friedman, R., Pyle, D., Duncan, R., Haeussler, P., Wooden, J., 2014. Geologic history of Siletzia, a large igneous province in the Oregon and Washington Coast Range: Correlation to the geomagnetic polarity time scale and implications for a long-lived Yellowstone hotspot. Geosphere 10, 692-719. https://doi.org/10.1130/GES01018.1.

CHAPTER 2

Rupture to the trench? Frictional properties and fracture energy of incoming sediments at the Cascadia subduction zone

Seyler, C.E., Kirkpatrick, J.D., Savage, H.M., Hirose, T., Faulkner, D. R., 2020. Rupture to the trench? Frictional properties and fracture energy of incoming sediments at the Cascadia subduction zone, Earth and Planetary Science Letters 549, 116413. https://doi.org/10.1016/j.epsl.2020.116413.

Abstract

The mechanical properties of sediment inputs to subduction zones are important for understanding rupture propagation through the accretionary prism during megathrust earthquakes. Clay minerals strongly influence the frictional behavior of fault gouges, and the clay content of subduction input materials varies through a stratigraphic section as well as for subduction margins globally. To establish the frictional properties of the shallow Cascadia subduction zone and place the results in a global context, we conducted high velocity rotary shear experiments on ODP core samples retrieved from Cascadia input sediments (35-45% clay) and a suite of individual clay species. We compared our results to a compilation of published high velocity experiments conducted on samples of wet gouge, dry gouge, and intact rock. For each sample type, three trends were identified with increasing normal stress: 1) the stress drop ($\tau_p - \tau_{ss}$) increases linearly, 2) the characteristic thermal weakening distance (D_{th}) decreases as a power law function except for wet clay-rich gouges, and 3) the fracture energy (W_b) shows no dependence. However, fracture energy does vary with sample type. Clay-rich gouges under wet conditions have the lowest fracture energy, and fracture energy for both dry and wet gouges is at least an order of magnitude lower

than estimates from intact rocks. Therefore when clay-rich lithologies are present, they may minimize spatial variations in frictional behavior, allowing earthquakes to propagate to the trench. For Cascadia input sediments, there is little variation in the fracture energy between lithologies, but the fracture energy of Cascadia sediments is around an order of magnitude higher than input sediments from other subduction margins. The high fracture energy of Cascadia sediments relative to other subduction margins may inhibit large amounts of shallow earthquake slip and dynamic overshoot.

2.1 Introduction

The 2004 Sumatra (M_w 9.1-9.3) and 2011 Tohoku-Oki (M_w 9.1) earthquakes emphasized that damaging tsunamis are promoted by large amounts of shallow coseismic slip during megathrust earthquakes (Bletery et al., 2016; Lay, 2018). Shallow slip requires rupture to propagate through the accreted sediments updip of the seismogenic zone. Clay-rich pelagic and hemipelagic sediments host the décollement zone at many subduction margins, such as Barbados, Costa Rica, the Japan Trench, and northern Cascadia (Han et al., 2017; Ikari et al., 2018; Moore et al., 2015; Vrolijk, 1990). The frictional properties of clay-rich sediments, particularly at high velocity, are therefore a primary control on earthquake propagation near the trench (Faulkner et al., 2011; Ikari and Kopf, 2017). For example, slip during the 2011 Tohoku-Oki earthquake most likely localized into clay-rich sediments (Chester et al., 2013; Kirkpatrick et al., 2015; Rabinowitz et al., 2020). Existing laboratory rock friction measurements indicate that at fast (~m/s) sliding velocities, clay-rich sediments weaken rapidly with slip and are characterized by low fracture energy (e.g., Faulkner et al., 2011; Sawai et al., 2014; Ujiie et al., 2013).

Earthquake fracture energy has been defined as the work done during dynamic weakening (Palmer and Rice, 1973) that includes an unknown partitioning between energy dissipated during fracturing and/or plastic deformation and heat dissipation during frictional sliding (Tinti et al., 2005). Fracture energy dictates the energy required for rupture propagation and the local accelerations on a fault during slip, and low fracture energy may encourage propagation to the trench during large megathrust earthquakes. The slip-weakening model describes the shear stress at a point on a fault during an earthquake as it evolves with slip. Shear stress increases to a peak, then decays to a steady state shear stress over a characteristic amount of slip, the slip weakening distance (Ida, 1972; Palmer and Rice, 1973). In this model, fracture energy (*G*) is defined as the work performed as shear stress decays linearly over the slip weakening distance and is written as

$$G = \frac{1}{2}(\tau_p - \tau_{ss})D_c \qquad (2-1)$$

where τ_p is the peak shear stress prior to the onset of weakening, τ_{ss} is the steady state shear stress, and D_c is the slip weakening distance. A general expression for fracture energy that does not rely on a particular shear stress evolution was defined by Abercrombie and Rice (2005) as

$$G(\delta) = \int_0^{\delta} [\tau(\delta') - \tau(\delta)]d\delta' \qquad (2-2)$$

where τ is shear stress, δ' is slip and δ is final slip. On the shallow portions of subduction zones, where the lithostatic load is low, incremental depth changes result in relatively significant changes in normal stress when compared to the total lithostatic load. Thus, the energy budget for shallow earthquake slip may be sensitive to depth depending on how fracture energy, frictional heating, and radiated energy change with normal stress.

Seismological estimates of fracture energy (hereafter G') are derived from seismic waveforms rather than direct measurements of shear stress on a fault. Estimates of seismological fracture energy indicate that total fracture energy for an earthquake scales as a power law function of the total slip (Abercrombie and Rice, 2005; Nielsen et al., 2016). Tsunami earthquakes, which occur on the shallow parts of some subduction zones, deviate from this general trend. These earthquakes can have significant amounts of slip but lack high frequency radiated energy, instead dissipating a larger fraction of their total energy as fracture energy relative to ordinary earthquakes (Kanamori, 1972; Venkataraman and Kanamori, 2004). The causes of tsunami earthquakes remain unclear, but the significant differences in the dynamics of tsunami earthquakes suggest fracture energy of sediments in the accretionary prism has important implications for rupture propagation.

At the Cascadia subduction zone, little is currently known about the frictional behavior of the shallow part of the megathrust. Paleoseismic records indicate a history of M_w 8 and M_w 9 earthquakes that ruptured all or significant portions of the subduction zone, suggesting rupture to the trench may be a common feature of large events at this margin (Goldfinger et al., 2012), though there are few small to moderate earthquakes to define the seismogenic zone limits. Geodetic measurements and heat flow data that indicate the thermally defined updip limit to the seismogenic zone is near the trench (Li et al., 2018; Oleskevich et al., 1999). At low velocity, sediments from the input section along the southern Cascadia margin have relatively high coefficients of friction of 0.4-0.5 (Ikari and Kopf, 2017), which increases the potential for stored elastic strain energy at shallow depth. However, the high velocity frictional behavior of sediments from Cascadia has not been measured, so the implications for rupture propagation are not fully defined. In this study, we conducted high velocity friction experiments on drill core samples of sediments from the Juan de

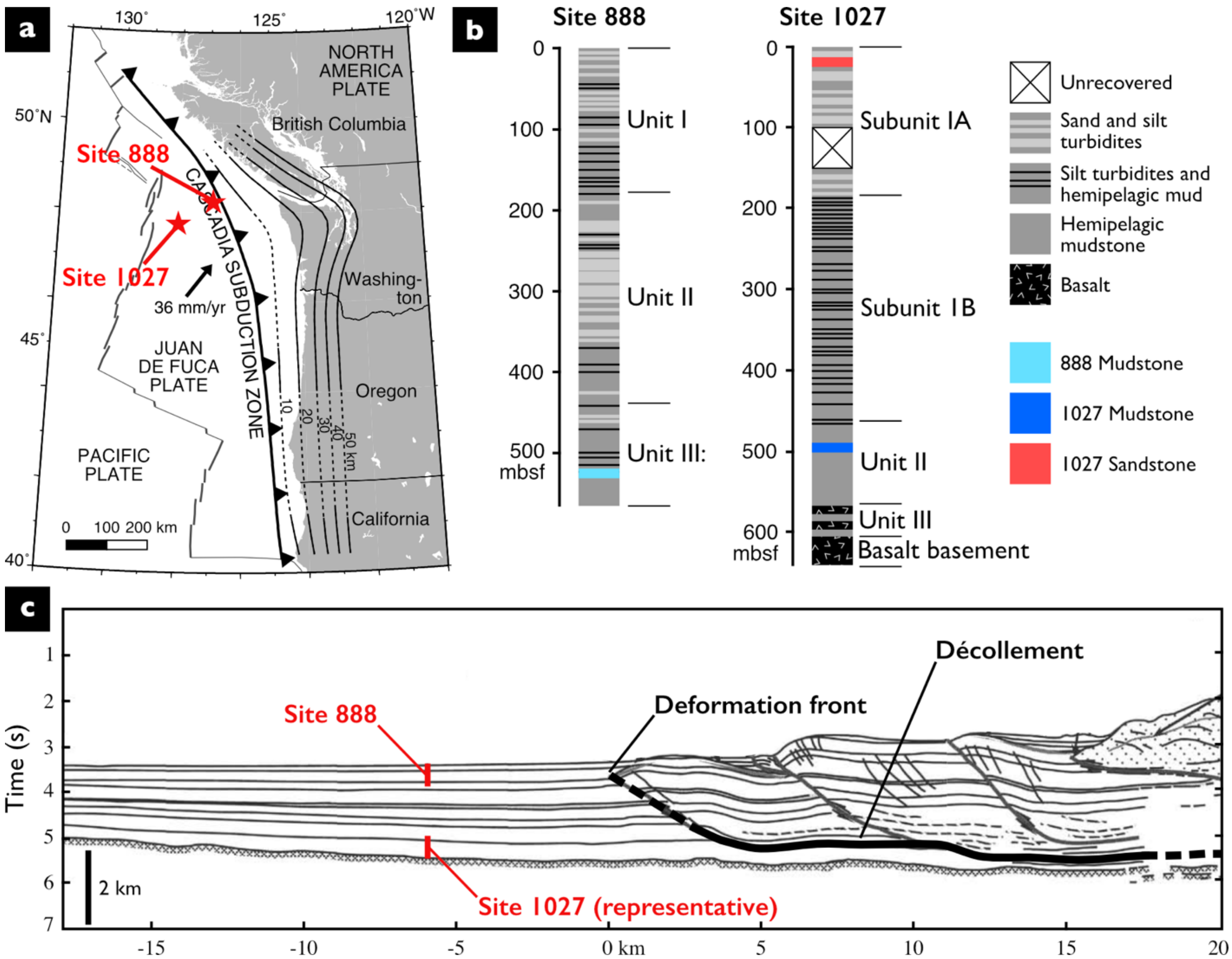

Figure 2-1: Location and stratigraphy of ODP sites. (a) Locations of ODP sites (red stars) relative to the Cascadia subduction zone, note the sites are in a transect near parallel to the plate convergence direction (adapted from Satake et al. (2003)). **(b)** Schematic stratigraphy at ODP sites with units as defined in expedition reports (adapted from Carson et al. (1995) and Fisher et al. (2000)). Core samples selected for experiments are highlighted with colored bars. Core samples include one sample of a sand turbidite (red bar) and two samples of hemipelagic mudstones (light blue and dark blue bars). **(c)** Sketch of seismic reflection data at Site 888 showing the location of the décollement, the deformation front, and the relative depth of stratigraphy in each hole (actual depth of Site 888 and representative depth of Site 1027) (adapted from Carson et al. (1995) and Fisher et al. (2000)).

Fuca plate that are the input to the Cascadia subduction zone to explore the effects of clay content and normal stress on their frictional behavior. We also measured the frictional behavior of individual clay species and compare our results to previously reported studies on gouges from other plate boundary faults to investigate whether Cascadia may be more prone to rupture to the trench than other margins.

2.2 Materials and Methods

2.2.1 Cascadia sample characterization

Core samples were obtained from two Ocean Drilling Program (ODP) sites near the Cascadia subduction zone: Site 888 of Leg 146 (Carson et al., 1995) and Site 1027 of Leg 168 (Fisher et al., 2000) (Fig. 2-1a). Though neither site sampled the complete input stratigraphic section immediately seaward of the trench, when combined, cores from these sites capture the lithologic variation expected throughout the input stratigraphic section overlying the basalt basement. Three similar stratigraphic units are present at both sites (Fig. 2-1b): interbedded sand and silt turbidites (Subunit 1A at Site 1027/Unit II at Site 888), interbedded silt turbidites and hemipelagic mud (Subunit 1B at Site 1027/Unit III at Site 888), and hemipelagic mudstone (Unit II at Site 1027). An additional unit of indurated mudstone, basalt talus, and diabase sills is present at Site 1027 (Unit III) (Carson et al., 1995; Fisher et al., 2000). At Site 1027, where the mineralogy has been previously characterized, clay content varies by lithology, and includes smectite, illite, chlorite, and kaolinite (Fisher et al., 2000). When the stratigraphy documented at Site 1027 is projected beneath the hole at Site 888, Site 1027 represents a relatively deep section of the stratigraphy near the trench. The hemipelagic mudstone present at Site 1027 represents the material most likely to be present at the décollement based on interpretation of seismic reflection data (Fig. 2-1c).

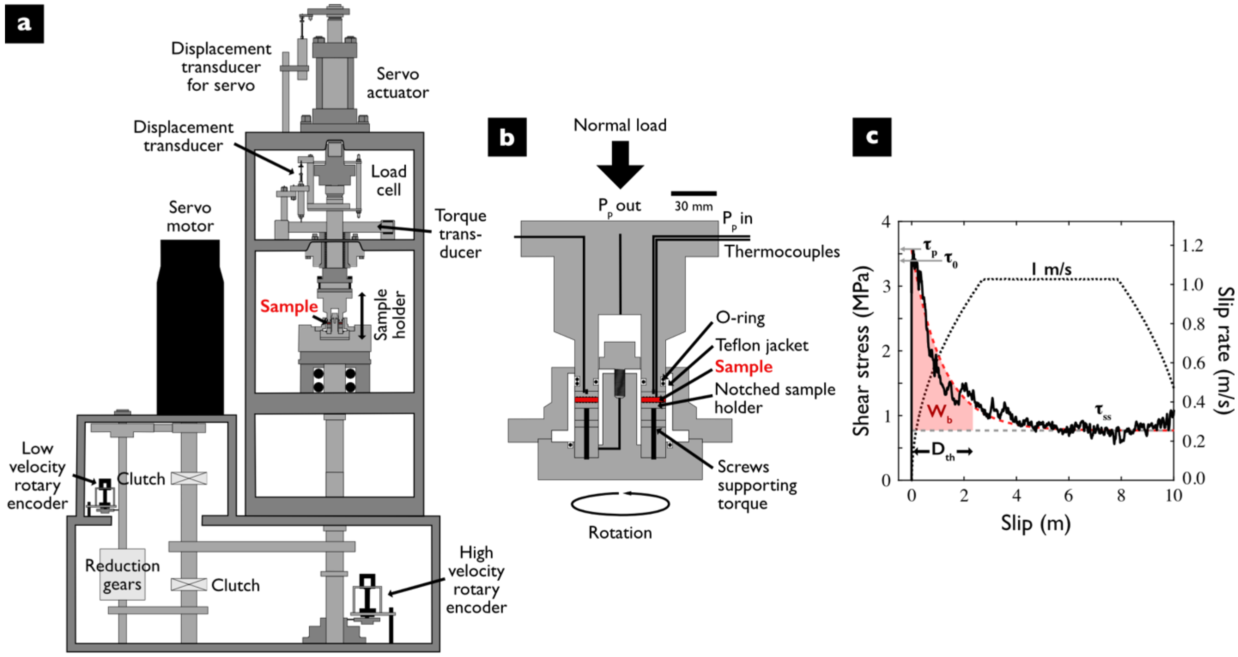

Figure 2-2: Experimental apparatus. (a) Schematic cross-sectional diagram of low to high velocity rotary shear apparatus (PHV) at the Kochi Core Center. **(b)** Schematic cross-sectional diagram of sample assembly. **(c)** Representative mechanical data for a high velocity rotary shear experiment (black solid line), model of shear stress evolution (red dashed line), residual shear stress (grey dashed line), and slip rate (black dotted line). τ_0 is the initial shear stress before the acceleration ramp, τ_p is the peak shear stress after acceleration begins, and τ_{ss} is the steady state shear stress achieved during slip at 1 m/s. Red shaded area represents the breakdown work (W_b) estimated from the model between slip at the onset of acceleration and the thermal weakening distance (D_{th}).

Three samples were selected for high velocity friction experiments to represent the input section to the Cascadia subduction zone: 1) core sample 146-888B-62X-2 (Leg-Site-hole-core-section) is a hemipelagic mudstone recovered from an approximate depth of 534.17 m beneath seafloor (mbsf), 2) core sample 168-1027B-03H-3 is from a layer with sand-sized grains within the interbedded turbidites (17.45 mbsf), and 3) core sample 168-1027B-53X-2 is a hemipelagic mudstone (493.55 mbsf). Sample composition was determined from X-ray diffraction and Rietveld refinement (see supplement for methods) and shows all three samples contain the same clay species, but there are variations in the clay content between lithologies (Table A-1; Fig. A-1). The Site 1027 sandstone contains 35% clay-sized fraction with the remainder split between quartz (30%) and feldspar (35%), while the Site 888 and 1027 mudstones both contain 45% clay-sized fraction, 20% quartz, and 35% feldspar. The uncertainty of these percentages is on the order of 5%. Smectite (montmorillonite), illite, and chlorite were identified in the clay fraction of all three samples (Fig. A-2), but the lack of crystallinity prohibits a quantitative analysis of the proportions of phases in the clay fraction.

2.2.2 Experimental procedure for tests on Cascadia samples

Friction experiments were conducted in the servo-controlled low to high velocity rotary shear apparatus (Fig. 2-2) at Kochi/JAMSTEC (Tanikawa et al., 2012). High velocity tests were conducted on synthetic gouges prepared from the three ODP core samples at 2, 5, and 8 MPa normal stress. Samples were dried in a 60 ˚C oven overnight before being disaggregated in a mortar and pestle and sieved to <250 μm. For each experiment, 15 g of sample powder was combined with 2 ml of distilled water to produce wet synthetic gouges. These gouges were placed between two annular steel sample holders with inner and outer radii of 15 and 30 mm, respectively, and then surrounded by an inner and outer Teflon jacket. The mechanical contribution of the Teflon was tested by conducting an experiment with no applied normal load and a gap between the sample holders. The shear stress contributed by the Teflon jacket was near zero (see supplement and Fig. A-3), and we did not correct for the negligible mechanical influence of the Teflon jacket or o-ring. Gouge samples were pre-compacted by a combination of three manual rotations at <1 MPa normal stress followed by a 40-minute hold at the normal stress condition of the experiment, producing an initial gouge zone thickness of approximately 2-3 mm. All tests were conducted at room temperature (25.5 ˚C) and humidity (31-34%).

For the annular sample holder, linear slip velocity varies from the inner to the outer diameter, so an equivalent slip velocity may be defined for analysis. Assuming shear stress is not dependent on velocity, the total frictional work on a fault is $W = \tau v_{eq} A$, where A is the cross-sectional area and v_{eq} is the equivalent slip velocity. The v_{eq} is then defined as

$$v_{eq} = \frac{4\pi R(r_1^2 + r_1 r_2 + r_2^2)}{3(r_1^2 + r_2^2)} \qquad (2-3)$$

where R is the revolution rate of the motor and r_1 = 15 mm and r_2 = 30 mm are the inner and outer radii of the sample holder, respectively (Hirose and Shimamoto, 2005). Samples were first deformed at a nominal v_{eq} of 0.5 to 100 µm/s over a total displacement of approximately 100 mm to establish a deformation fabric. Then, samples were deformed at a nominal v_{eq} of 500 µm/s for 0.2 rotations, then accelerated at a rate of 0.2 m/s^2 to the target nominal v_{eq} of 1 m/s for 35 rotations for a constant total displacement of 10.5 m (Fig. A-4a). At the end of the experiment, v_{eq} was decelerated at the same rate to 500 µm/s before terminating the experiment.

2.2.3 Experimental procedure for tests on individual clay species

High velocity experiments were also conducted on five samples of commercially available clay-rich materials. The principal clay components for these powders are illite, pyrophyllite, montmorillonite, sericite and talc. The purity, accessory components, and the sources for each gouge type are listed in Table A-2. All mineralogical components were identified by X-ray diffraction using Rietveld refinement. The uncertainty of the percentages is on the order of 5%.

Individual clay species experiments were conducted on a high velocity rotary shear apparatus at Kochi/JAMSTEC (for details see supplement and Tsutsumi and Shimamoto (1997)) at normal loads ranging from 0.7 to 3.25 MPa. A layer of gouge was produced from 1 g of the sample material placed between two solid gabbro slider blocks of a nominal 25 mm diameter. The surfaces of the slider blocks in contact with the gouge were prepared using SiC #80 powder. The layers of gouge were contained by a Teflon sleeve that was manufactured to fit tightly on the slider blocks, the same arrangement used by Mizoguchi et al. (2007). The mechanical contribution of the Teflon was tested by running an experiment with no applied normal load. The shear stress of the Teflon was below the measured shear stresses of the synthetic gouges at their lowest level (see supplement and Fig. A-3), and we have not corrected the data for the negligible mechanical influence of the Teflon sleeve. Prior to running the tests at high velocity, the normal load was applied to the sample and the sliding blocks were rotated relative to one another to pre-compact the gouge. The pre-compaction resulted in a gouge layer of approximately 1 mm thickness and porosity of ~50%. For the tests conducted under wet conditions, 0.5 ml of de-ionized water was added to the gouge prior to assembly.

All tests were run at a nominal v_{eq} of 1.3 m/s with an initial acceleration ramp of ~10 m/s^2 (Fig. A-4b). The motor was first accelerated to the desired speed, then engaged with the sample via the magnetic clutch assembly. This accelerated the rotating side of the sample assembly to 1.3 m/s over a slip distance of around 10 cm. When the desired slip distance for an experiment was achieved, the motor was switched off and the sample decelerated due to friction.

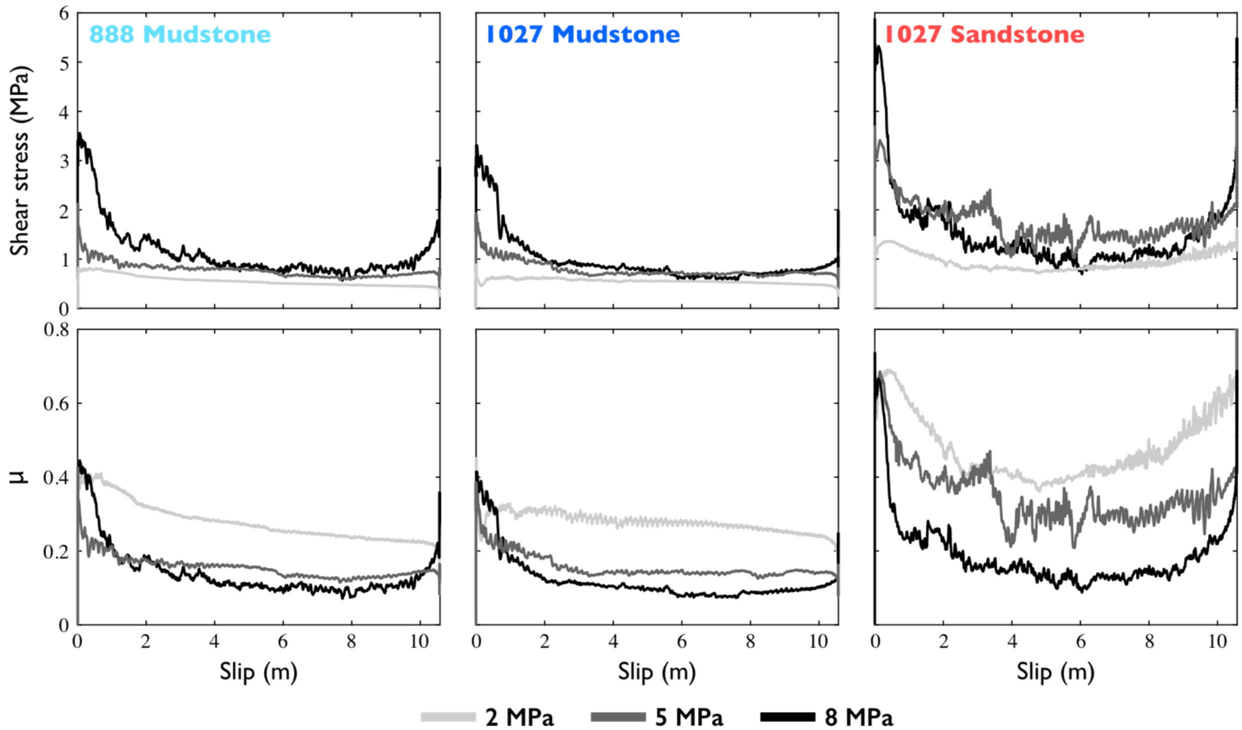

Figure 2-3: Mechanical data from experiments on Cascadia core samples. Top row: Mechanical data plotted as shear stress versus slip showing that the steady state shear stress is consistent across normal stress conditions for each sample. **Bottom row:** Mechanical data plotted as apparent friction coefficient versus slip showing that peak friction coefficient is consistent across normal stresses while the steady state friction coefficient decreases.

2.2.4 Estimation of fracture energy from high velocity experiments

Fracture energy can be estimated from high velocity friction experiments as proportional to the product of shear stress and slip weakening distance. We estimated the breakdown work (W_b) and the thermal weakening distance (D_{th}) directly from the shear stress evolution recorded on the experimental fault (Fig. 2-2c). W_b is the work associated with dynamic weakening from peak (τ_p) to steady state shear stress (τ_{ss}), equivalent to fracture energy (G), and is considered comparable to seismological estimates of fracture energy (G') (Tinti et al., 2005). W_b is dependent on the breakdown stress drop ($\tau_p - \tau_{ss}$) and the thermal weakening distance (D_{th}), a characteristic slip weakening distance. D_{th} represents the amount of slip necessary for the shear stress to be reduced to 1/e of $\tau_p - \tau_{ss}$. Previous definitions for the slip weakening distance (D_c) defined the characteristic distance based on a 95% reduction of the initial $\tau_p - \tau_{ss}$ value (Mizoguchi et al., 2007). We prefer D_{th} because it captures the significant initial phase of weakening triggered by thermally induced weakening mechanisms (Di Toro et al., 2011). To estimate these parameters, the shear stress curve from each experiment was fit with a least-squares approach to the following exponential decay equation as defined by Di Toro et al. (2011)

$$\tau = \tau_{ss} + (\tau_p - \tau_{ss})e^{-\frac{\delta}{D_{th}}} \qquad (2-4)$$

where τ_{ss} is the steady state shear stress (MPa), τ_p is the peak shear stress (MPa), D_{th} is the thermal weakening distance (m), and δ is the slip accumulated after the peak shear stress (m). W_b was then estimated by integrating under the modeled shear stress curve from the slip at τ_p to D_{th}

$$W_b = \int_0^{D_{th}} (\tau_p - \tau_{ss})e^{-\frac{\delta}{D_{th}}}\, d\delta \qquad (2-5)$$

for each experiment.

2.3 Experimental results

2.3.1 Cascadia core samples

All of the high velocity experiments (Fig. 2-3) exhibited a similar stress evolution to previously published results for gouges (e.g., Mizoguchi et al., 2007). Following the run-in phase, v_{eq} was accelerated from 500 μm/s to 1 m/s, which resulted in an increase in shear stress from the initial (τ_0) up to a peak (τ_p), followed by a decay to a lower steady state value (τ_{ss}). τ_0 and τ_p are higher for the Site 1027 sandstone than the Site 888 and 1027 mudstones, however nearly all experiments across the range of normal stresses tested have τ_{ss} around 1-2 MPa (Table 2-1). Experiments

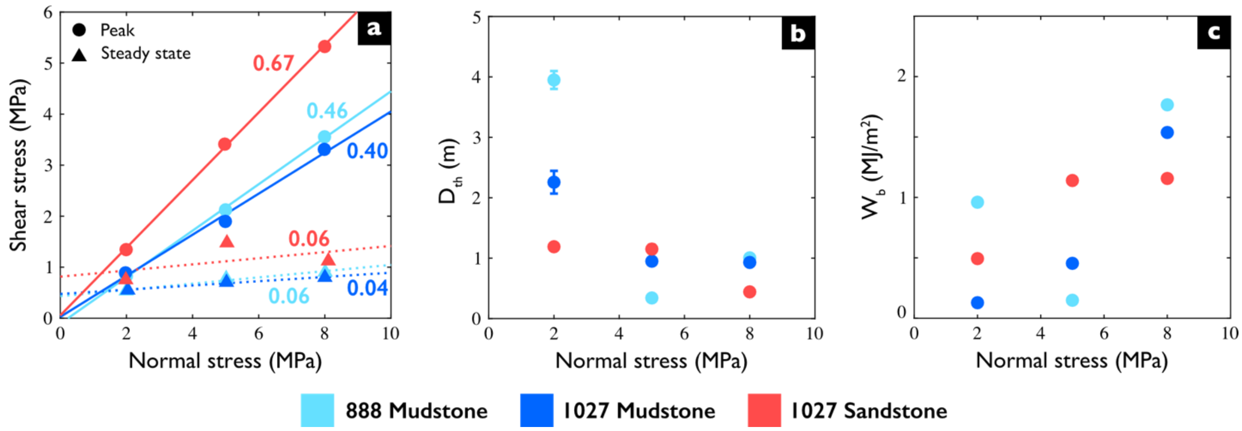

Figure 2-4: Friction and fracture energy parameters from experiments on Cascadia core samples. (a) Shear stress scaling with normal stress for peak shear stress (circles) and steady state shear stress (triangles). Friction coefficients for each sample are defined as the linear scaling between shear stress and normal stress and are determined from the peak shear stress (solid lines) and steady state shear stress (dotted lines). **(b)** Thermal weakening distance (D_{th}) decreases with normal stress for all lithologies. Error bars from the model fit are plotted for all data points, but most do not extend beyond the circles. **(c)** Breakdown work (W_b) does not vary significantly between lithologies.

conducted on the Site 1027 sandstone at all normal stresses and the Site 888 and 1027 mudstones at a normal stress of 8 MPa saw an increase of shear stress at the end of the experiment during deceleration, possibly related to dynamic healing or a loss of pore fluids.

For all three samples, τ_p scales linearly with normal stress and the friction coefficients at peak stress (μ_p) are 0.67 for the 1027 sandstone and 0.40-0.46 for the mudstones (Fig. 2-4a). These friction coefficients are higher than those observed at slower slip velocities (Fig. A-3) because of the increase in shear stress associated with increasing slip velocity (e.g., Cocco and Bizzarri, 2002). τ_{ss} did not change significantly with normal stress and the friction coefficients at steady state (μ_{ss}) are 0.04-0.06 for all samples (Fig. 2-4a). This small variation in the steady state behavior between

Table 2-1: Experimental conditions, mechanical results, and fracture energy estimates for Cascadia samples

Run Number	Sample/ Sample name	σ_n [MPa]	τ_0 [MPa]	τ_p [MPa]	τ_{ss} [MPa]	D_{th} [m]	W_b [MJ/m^2]
PHV462	888 mudstone 888B-62X-2	2	0.49	0.83	0.54	3.949	0.960
PHV463	888 mudstone 888B-62X-2	5	1.88	2.12	0.78	0.341	0.149
PHV464	888 mudstone 888B-62X-2	8	2.92	3.56	0.90	1.005	1.766
PHV465	1027 mudstone 1027B-53X-2	2	0.61	0.89	0.55	2.257	0.129
PHV466	1027 mudstone 1027B-53X-2	5	1.49	1.90	0.70	0.949	0.455
PHV467	1027 mudstone 1027B-53X-2	8	2.74	3.31	0.80	0.929	1.537
PHV468	1027 sandstone 1027B-03H-3	2	1.27	1.36	0.75	1.189	0.494
PHV469	1027 sandstone 1027B-03H-3	5	3.34	3.41	1.48	1.150	1.140
PHV470	1027 sandstone 1027B-03H-3	8	5.30	5.33	1.12	0.442	1.157

the samples indicates viscous-type deformation in each experiment, similar to what was observed at the Japan Trench Fast Drilling Project (JFAST) by Ujiie et al. (2013). As a consequence of the minimal change in τ_{ss} with normal stress, $\tau_p - \tau_{ss}$ increases linearly with normal stress and is larger for the sandstone sample (Fig. 2-4a). However, the thermal weakening distance (D_{th}) decreases with normal stress and is larger for the mudstone samples (Fig. 2-4b; Table 2-1). As a result of the

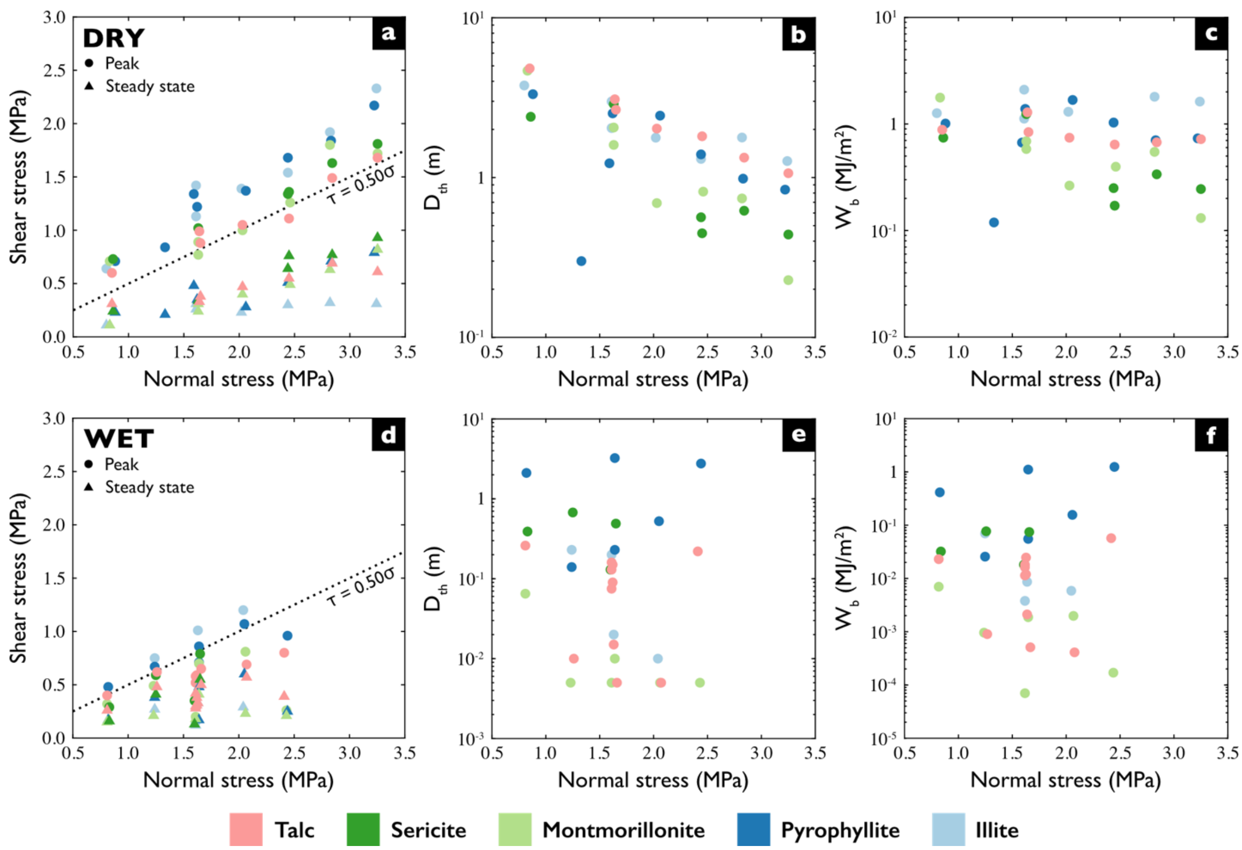

Figure 2-5: Friction and fracture energy parameters from dry (a-c) and wet (d-f) experiments on individual clay species. (a,d) Shear stress scaling with normal stress for peak shear stress (circles) and steady state shear stress (triangles). Dashed lines show a friction coefficient of 0.50 for reference. Dry experiments have a higher peak friction coefficient than wet experiments, and steady state shear stress during dry experiments has a stronger dependence on normal stress than wet experiments. **(b,e)** Thermal weakening distance (D_{th}) decreases with normal stress for dry experiments but has no dependence on normal stress for wet experiments. **(c,f)** Breakdown work (W_b) does not vary systematically with normal stress for dry or wet experiments. Note that y-axis limits for D_{th} and W_b are different between the wet and dry conditions.

opposite dependence on normal stress for these two parameters, there is only a small variation in the breakdown work (W_b) (Fig. 2-4c; Table 2-1), which varies by <2 MJ/m^2 for each sample.

2.3.2 Individual clay species

Experiments conducted on samples of individual clay species followed the same overall trends in mechanical behavior as the Cascadia samples and the frictional behavior of each clay species was generally similar (also see Faulkner et al. (2011)). Under dry conditions, τ_p and τ_{ss} increase linearly with normal stress for each clay species (Fig. 2-5a-c). Under wet conditions, τ_p increases linearly, but τ_{ss} does not significantly increase, again suggesting viscous-type deformation (Fig. 2-5d-f). In both dry and wet experiments, the friction coefficients at peak and steady state are highest for illite and pyrophyllite and lowest for talc and montmorillonite (Fig. A-6). For all clay species, $\tau_p - \tau_{ss}$ is smaller for the wet experiments. D_{th} decreases with normal stress under dry conditions for each clay species, but there is no apparent trend under wet conditions with the exception of montmorillonite. Instead, under wet conditions D_{th} ranges over approximately three orders of magnitude. Generally, montmorillonite has the lowest breakdown work (W_b) while pyrophyllite has the highest. W_b shows no dependence on normal stress for most clay species, but there is a possible weak dependence for sericite and montmorillonite under dry conditions and illite under wet conditions. Overall, W_b varies in magnitude between different clay species by up to three orders of magnitude and does not appear to vary systematically with normal stress.

2.4 Discussion

2.4.1 Data compilation of high velocity friction experiments

The experiments on Cascadia core samples demonstrate that the breakdown stress drop ($\tau_p - \tau_{ss}$) and thermal weakening distance (D_{th}) are dependent on normal stress, but the breakdown work (W_b) shows little variation. Additionally, of the three Cascadia samples, the Site 1027 sandstone has the highest τ_p and τ_{ss}, suggesting clay content plays a role in determining the overall frictional

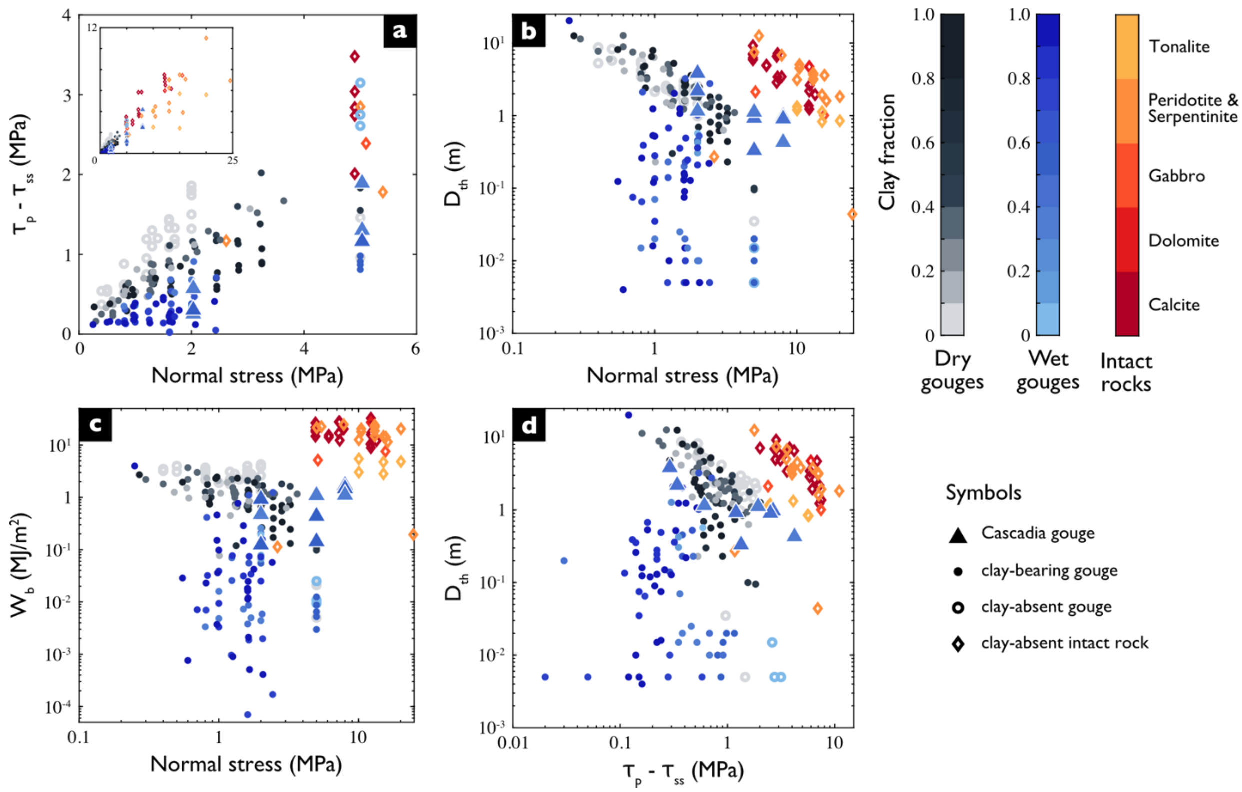

Figure 2-6: Compilation of high velocity rotary shear experimental data. (a) Breakdown stress drop ($\tau_p - \tau_{ss}$), with inset displaying the full normal stress range, **(b)** thermal weakening distance (D_{th}), and **(c)** breakdown work (W_b) scaling with normal stress. **(d)** Thermal weakening distance (D_{th}) scaling with breakdown stress drop ($\tau_p - \tau_{ss}$).

behavior. Individual clay species deformed under wet conditions have extremely low values for D_{th} and W_b with no clear dependence on normal stress. Together, the two sets of experiments suggest W_b may be independent of normal stress, and that clay content and the presence of water may be significant controls on the overall frictional behavior and fracture energy of a rock, as noted previously (e.g., Faulkner et al., 2011; Ikari et al., 2009).

To further explore the effect of normal stress and understand the role of clay content in the frictional behavior of fault rocks at high slip rates, we compiled laboratory estimates of peak and

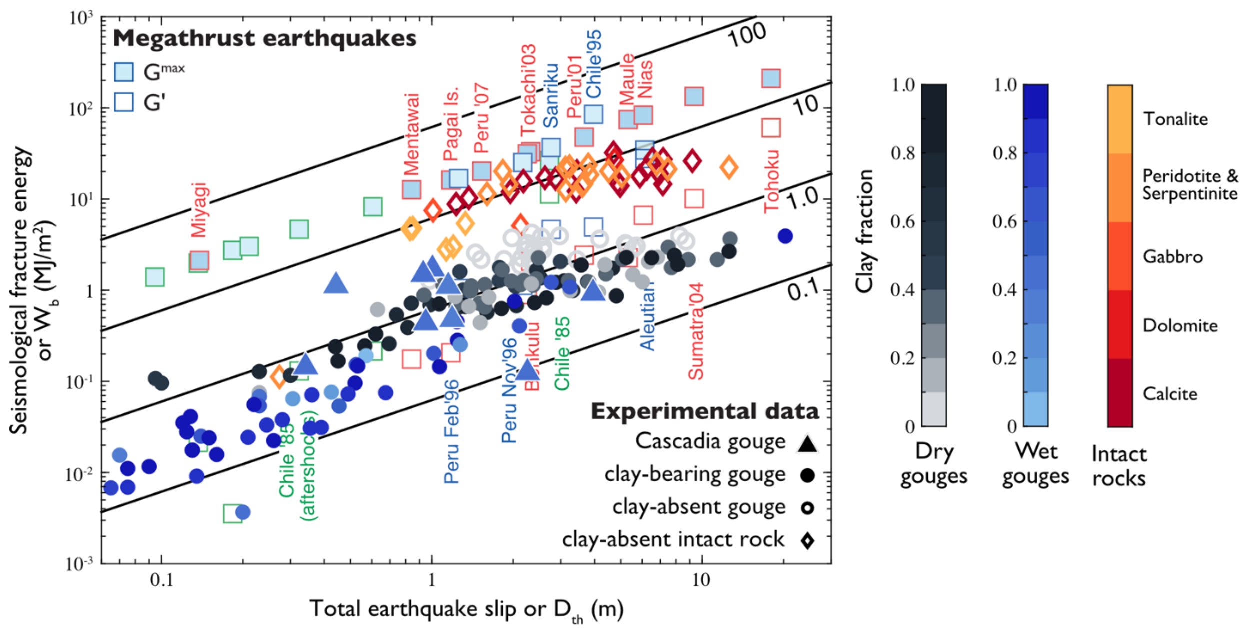

Figure 2-7: Comparison between experimental and seismological estimates of fracture energy. Compilation of W_b evaluated at $\delta = D_{th}$ for high velocity rotary shear experimental data from wet gouges, dry gouges, and intact rocks imposed on the compilation of seismological estimates of fracture energy for megathrust earthquakes (Viesca and Garagash, 2015). Note that the experimental data overlies the G' fracture energy estimates for megathrust earthquakes. Black curves represent W_b calculated with Eq. 2-5 for constant breakdown stress drops of 0.1 to 100 MPa.

steady state shear stress, slip weakening distance, and fracture energy from 233 experiments conducted on 5 different machines reported in 20 previous studies (Fig. 2-6; Table A-3). The compiled data were separated into three categories: 1) gouges deformed under wet conditions, 2) gouges deformed under dry conditions, and 3) intact rocks deformed under dry conditions.

Previously reported slip weakening distance and fracture energy values were converted to D_{th} and W_b (see supplement Section A3 and Fig. A-5 for details).

The linear scaling of $\tau_p - \tau_{ss}$ with normal stress is a common feature of all datasets (Fig 6a). Most of the compiled gouge experiments were conducted at a normal stress of 5 MPa or less. The data at these low normal stresses show that the constant of proportionality between $\tau_p - \tau_{ss}$ and normal stress decreases with increasing clay content for both wet and dry gouges. Notably, the wet gouges generally have lower slopes than the dry gouges. Intact rocks have a similar range for constants of proportionality as the dry gouges. These results show the $\tau_p - \tau_{ss}$ scaling is a material property dictated by τ_p scaling with normal stress (μ_p) and is not significantly modified by smaller increases in τ_{ss} with increasing normal stress.

D_{th} decreases as a power law function of normal stress for dry gouges and intact rocks, but there is no clear variation with clay content (Fig. 2-6b). The power law exponents (i.e., the slopes) appear similar for dry gouges and intact rocks. The wet gouges do not exhibit any clear dependence of D_{th} on normal stress, with values ranging over three orders of magnitude. Within wet gouges, D_{th} behaves systematically for some individual clay species, such as montmorillonite, while others show no trend with normal stress (Fig. 2-5). Lack of a systematic dependence on normal stress is representative of most wet gouges (e.g., Sawai et al., 2014) and there is also no clear relationship between D_{th} and clay content.

W_b exhibits no scaling with normal stress for any of the categories (Fig. 2-6c). The absence of a relationship between fracture energy and normal stress has been reported previously (Nielsen et al., 2016). Within the wet gouges, illite demonstrates a possible weak dependence on normal stress (Fig. 2-5), but most datasets under wet or dry conditions show no such dependence, including datasets compiled from the literature as well as those from this study (e.g., Cascadia results in Fig.

2-4; other phases in Fig. 2-5; French et al., 2014; Mizoguchi et al., 2007; Sawai et al., 2014). W_b values for dry gouges overlap with the highest W_b values for wet gouges, but the smallest W_b values for wet gouges are three orders of magnitude lower than the other two categories. Neither wet nor dry gouges show any clear trends with clay content, but the magnitude of W_b does vary with clay species (Fig. 2-5).

Finally, there is a strong dependence between $\tau_p - \tau_{ss}$ and D_{th} for dry gouges and intact rocks, but there is no such dependence for wet gouges (Fig. 2-6d). This represents a fundamentally different behavior for wet and dry conditions. A correlation between $\tau_p - \tau_{ss}$ and D_{th} is expected for dry conditions where both of these two parameters were observed to vary with normal stress. As effective normal stress was not measured in the slip zone during the experiments, a trend with normal stress for wet gouges might be hidden in the normal stress uncertainty. However, the absence of a correlation between D_{th} and $\tau_p - \tau_{ss}$ suggests the lack of scaling with applied normal stress for wet gouges is robust despite not measuring pore fluid pressure or effective normal stress during experiments conducted under wet conditions.

The compiled data suggest that W_b is independent of normal stress, despite $\tau_p - \tau_{ss}$ and D_{th} having strong dependencies on normal stress for intact rocks and dry gouges. We developed an expression for W_b derived from the expressions for $\tau_p - \tau_{ss}$ and D_{th} to validate the lack of scaling for W_b. We fit the observed linear relationship between normal stress and $\tau_p - \tau_{ss}$ following the equation

$$\tau_p - \tau_{ss} = a_1 \sigma_n \qquad (2-6)$$

where a_1 is a coefficient and σ_n is normal stress. We also fit the observed power law relationship between normal stress and D_{th} following the equation

$$D_{th} = a_2 \sigma_n^{-b} \tag{2-7}$$

where a_2 is a coefficient and b is the power law exponent (Di Toro et al., 2011). Using equations 2-6 and 2-7, the equation for estimating W_b (Eq. 2-1; Di Toro et al., 2011) can be re-written as

$$W_b = \frac{1}{2} a_1 a_2 \sigma_n^{1-b} \tag{2-8}$$

with b expected to be near 1 to cancel the dependence on normal stress. For each dataset or subset, we used a nonlinear least-squares fit and report a 95% confidence interval for equations 2-6 and 2-7 (Table 2-2). The wet and dry gouges were separated into three groups by clay content due to the strong influence of clay on the friction coefficient and therefore the magnitude of $\tau_p - \tau_{ss}$, resulting in different values for a_1. The wet gouge categories are too scattered for any reasonable model fit for D_{th} or W_b. Most of these fits are associated with large uncertainty due to the spread of data in each category, but all resulting exponents for the relationship between normal stress and W_b are near zero, reflecting no dependence on normal stress due to the tradeoff between increasing $\tau_p - \tau_{ss}$ and decreasing D_{th}. Projecting the results for dry gouges and intact rocks to seismogenic depths of ~10 km by approximating the normal stress as lithostatic stress suggests $\tau_p - \tau_{ss}$ would range from 10s of MPa near the surface to 100s of MPa at seismogenic depths, D_{th} would vary from meters near the surface to centimeters or millimeters at seismogenic depths, yet W_b would not vary significantly.

The majority of the compiled experiments were conducted on the high velocity rotary shear machine at Kochi/JAMSTEC ("HVR"), but some experiments were conducted on other machines at Kochi/JAMSTEC, Kyoto University, Hiroshima University, and INGV in Italy. Significant differences in boundary conditions between rotary shear machines, such as sample dimension and thermal conductivity and permeability of sample holders, may lead to some variation in the

Table 2-2: Power law fits to compiled data

		a_1	a_2	b	$W_b \propto \sigma_n^x$
Wet gouges	*0% clay*	0.57 ± 0.14			
	<30% clay	0.26 ± 0.06			
	>30% clay	0.19 ± 0.02			
Dry gouges	*0% clay*	0.77 ± 0.14	3.35 ± 0.40	0.90 ± 0.18	0.10
	<30% clay	0.52 ± 0.02	3.66 ± 0.67	1.00 ± 0.25	0.00
	>30% clay	0.39 ± 0.04	3.75 ± 0.47	0.98 ± 0.14	0.02
Intact rocks		0.43 ± 0.04	36.84 ± 24.94	1.03 ± 0.35	-0.03

experimental results (Savage et al., 2018; Yao et al., 2016). Additionally, differences in the acceleration path will increase τ_p and decrease D_{th}, but not affect τ_{ss} (Sone and Shimamoto, 2009). These combined acceleration effects may cancel each other and produce a small effect on W_b. Though we have not controlled for these differences, there are still clear trends that emerge from the compilation, suggesting these trends are robust despite the data being sourced from various machines at multiple labs.

2.4.2 Comparison of gouges and intact rocks

The compiled data indicate that, in general, dynamic weakening during seismic slip is influenced by the clay content, the presence of water, and the material state (i.e., gouge or intact rock). Clay content controls the initial strengthening (τ_p) for gouge samples (Fig. 2-6a), which is expressed by a_1 in Eq. 2-8 and decreases with increasing clay fraction (Table 2-2). Results for intact rocks vary with rock type (e.g., a_1 = 0.57 for calcite, a_1 = 0.45 for peridotite), but wet clay-rich gouges have the smallest values of a_1 (0.19). The rate of weakening (D_{th}) does not systematically vary with clay content for wet or dry gouges (Fig. 2-6b). The length of D_{th} appears to depend more on the presence of water and the material state of the sample than clay content (e.g., a_2 for intact rocks is an order of magnitude greater than dry gouges, but we found no clear variation of a_2 with clay content within the dry gouges). These characteristics control the porosity, permeability, and thermal diffusivity of the experimental fault, which dictate the pore fluid pressure in the sample (Faulkner et al., 2011; Rice, 2006; Yao et al., 2016). For example, the very small values of D_{th} for wet gouges imply the reduced permeability of wet, particularly clay-bearing, gouges promotes rapid weakening due to the efficacy of thermal pressurization as a weakening mechanism (e.g., Ujiie and Tsutsumi, 2010). Additionally, differences between gouges and intact rocks may also be due to the ability of granular materials to facilitate weakening via non-thermal effects (e.g., shear-enhanced compaction leading to pore pressurization or rolling of grains) (Aretusini et al., 2019; Reches and Lockner, 2010).

Breakdown work (W_b) is dependent on τ_p, τ_{ss}, and D_{th} and thus also influenced by the material properties of the sample and the experimental fault system. These influences manifest as the notable difference in the magnitudes of W_b for each of the three categories (Fig. 2-6c). W_b for wet gouges ranges two orders of magnitude lower than the range for dry gouges, and W_b for most intact rocks ranges an order of magnitude higher than dry gouges. Differences in W_b are a measure of the efficiency of the weakening mechanism, again suggesting that thermal pressurization (invoked for wet gouges) is more efficient at reaching the necessary temperature for weakening (~150 °C for thermal pressurization) (French et al., 2014; Kitajima et al., 2010) than the mechanisms for dry gouges or intact rocks (e.g., powder lubrication and flash heating) (Di Toro et al., 2011). Overall, the effects of water and material state outweigh clay content in determining D_{th}, but clay content still influences W_b.

2.4.3 Comparison of laboratory and seismological estimates of fracture energy

Seismological fracture energy (G') is a measure of the energy per unit area for the propagation of the rupture tip and is estimated from earthquake source spectra and the earthquake energy budget (Abercrombie and Rice, 2005). The velocity step from the run-in stage to 1 m/s during the experiments may not be a good representation of the transition from pre-rupture to sliding at a rupture tip for a variety of reasons. However, the magnitudes of lab estimates overlap with seismological estimates of G' (Nielsen et al., 2016; Selvadurai, 2019 and references therein). Though the lab does not directly replicate an earthquake, many of the energy sinks associated with breakdown work during both natural and experimental events are the same (e.g., frictional resistance, comminution, melting, heating of pore fluid, and heat dissipation), suggesting that the lab and seismological estimates are comparable.

The experimental data we compiled exhibits a scaling between W_b and D_{th} that is strikingly similar to the positive scaling between seismological estimates of fracture energy and earthquake size (total slip during the earthquake) (Fig. 2-7) (Abercrombie and Rice, 2005; Viesca and Garagash, 2015). A similar relationship between fracture energy and earthquake size has also been reproduced in the lab by calculating fracture energy for increments of accumulating slip rather than at D_{th} (Nielsen et al., 2016). Viesca and Garagash (2015) estimated fracture energy based on two definitions: 1) for crack-like ruptures, fracture energy is defined as $G' = \left(\frac{\Delta\tau}{2} - \tau_a\right)\delta$ where $\Delta\tau$ is the static stress drop, τ_a is the apparent stress, and δ is slip, and 2) for pulse-like ruptures, fracture energy is defined as $G^{\max} = G' + \tau_f\delta$ where τ_f is the final fault strength and δ is slip. W_b for wet and dry clay gouges overlap with G' estimates for large earthquakes at subduction zones and major crustal fault zones. Despite the heterogeneity over a rupture area and the importance of acceleration for determining seismological estimates of fracture energy (Tinti et al., 2005), any variation in the acceleration ramp for experiments and natural earthquakes does not overshadow the scaling relationships. In our data, W_b is based on the dynamic stress drop measured at steady state so there is no over- or undershoot. In other words, W_b does not increase further with slip once weakening is complete. The similarity in the experimental and seismological values that arises when D_{th} is equated with total slip therefore supports the idea that ruptures are crack-like on average and may be well explained by a simple slip-weakening model. This also indicates that D_{th} scales with total slip, such that larger earthquakes have larger W_b values on average. The distinction between crack-like vs. pulse-like behavior depends on the background stress level and slip zone thickness, and the agreement between experimental and seismic data supporting crack-like behavior indicates these earthquakes had either high background stress levels or thin slip zones resulting from rapid localization (Noda et al., 2009).

2.4.4 Implications for the Cascadia subduction zone and other natural faults

The possibility of rupture to the trench at the Cascadia subduction zone depends on the degree of locking at the margin as well as the frictional behavior of the sediments hosting the décollement. The upper limit of the seismogenic zone is thought to extend to the trench based on elevated temperatures at the deformation front exceeding the 100 °C smectite-illite transition (Oleskevich et al., 1999). Locking to the trench is supported by current geodetic fault locking models (Li et al., 2018) and a lack of earthquake epicenters or slow earthquake activity near the trench in northern Cascadia (McGuire et al., 2018; Obana et al., 2015). Offshore of Vancouver Island and Washington state, the décollement is located just above the oceanic basement (Fig. 2-1; Carson et al., 1995; Han et al., 2017), suggesting that the décollement is likely hosted in hemipelagic mudstones near the base of the thick package of incoming sediments. Friction coefficients of 0.36 and 0.41 (based on pre-acceleration v_e of 500 µm/s, see Fig. A-3) for the core samples of hemipelagic mudstones in this study are consistent with previous studies that characterize northern Cascadia as a relatively mechanically strong subduction zone (Cubas et al., 2016; Han et al., 2017). The compiled experimental data show that the fracture energy of the Cascadia input samples under wet conditions is relatively high compared to that of samples representative of other subduction margins such as the Japan Trench and Costa Rica (Fig. 2-8), likely because the Cascadia samples are relatively clay poor. A lithologic control on subduction zone behavior has been proposed by previous workers (Moore et al., 2015).

Using our measurements from Cascadia samples and the compiled data, we are able to compare the frictional behavior of a diverse set of subduction zone sediments and other fault rocks in detail. Breakdown work (W_b), which is a primary control on rupture dynamics, varies by two orders of magnitude between major plate boundary faults, and by around one order of magnitude for subduction margins (Fig. 2-8). Clay-rich pelagic rocks have low W_b (e.g., samples retrieved from the Japan Trench; Sawai et al., 2014; Ujiie et al., 2013), whereas clay-poor mudstones dominated by terrigenous input have moderate W_b (e.g., Cascadia and the Nankai Trough; this study; Ujiie and Tsutsumi, 2010). However, there are exceptions to the relationship between clay content and W_b that suggest this relationship is not systematic, such as the moderate W_b of smectite-rich SAFOD fault gouge (Fig. 2-8). Although paleoseismic records for Cascadia document tsunamis caused by megathrust earthquakes in the past, the moderate W_b of the Cascadia core samples (0.1 to 2 MJ/m^2) compared to other subduction zones may suggest that Cascadia is less susceptible to

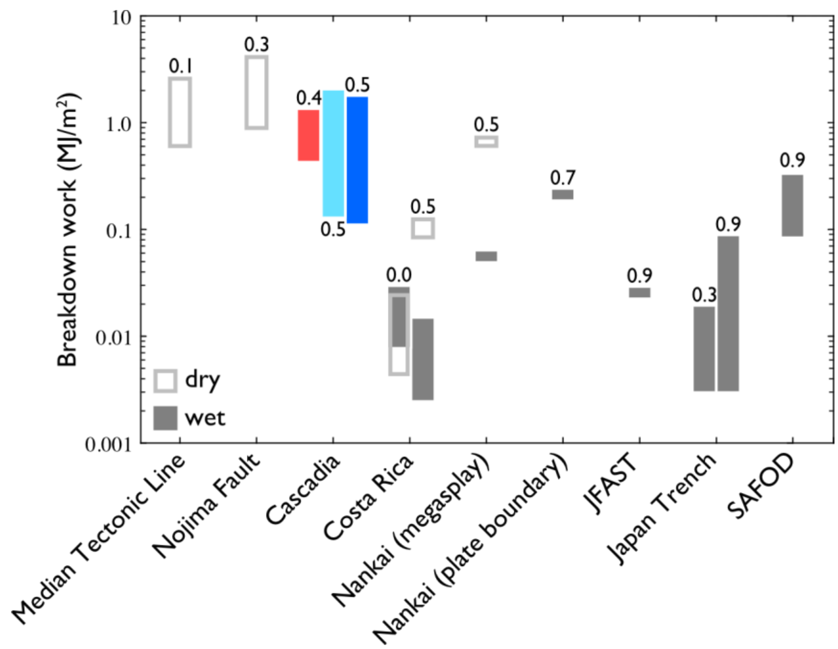

Figure 2-8: Breakdown work (W_b) estimates from natural samples, including fault gouge from the Median Tectonic Line in Japan, fault gouge from the Nojima Fault in Japan, smectite-rich fault gouge from SAFOD core retrieved from the San Andreas Fault in California, sand turbidite and hemipelagic mudstones from ODP core retrieved from the input section of the Cascadia subduction zone (this study; colors are the same as in Fig. 2-4), megasplay and plate boundary fault gouge from IODP core retrieved from the Nankai subduction zone, smectite-rich fault gouge from IODP core retrieved from the décollement zone of the Japan Trench, pelagic sediments from DSDP core retrieved from the input section of the Japan Trench, silty clays and biogenic oozes from IODP core retrieved from the input section of the Costa Rica subduction zone. Breakdown work estimates from dry experiments (light grey) and wet experiments (dark grey) are plotted as rectangles encompassing the range of values. Numbers above or below each sample indicate the clay fraction. Data sources are listed in the supplement and Table A-3.

large amounts of shallow slip and dynamic overshoot. Alternatively, as the Cascadia megathrust is thought to be late in the seismic cycle (Wang et al., 2012), our results raise the possibility that the high frictional strength of the Cascadia core samples, and therefore likely the décollement, may result in higher resolved shear stress on the interface prior to rupture, enhancing the potential for ruptures to propagate to the trench. Additionally, any lithological control on rupture propagation at Cascadia will be limited due to both the lack of variability in the incoming sediment composition and the lack of variability in the frictional behavior between the hemipelagic mudstones and the sandstone samples.

Tsunami earthquakes rupture slowly beneath the shallow part of accretionary prisms at some margins and are characterized by low radiation efficiencies, $\eta_R < 0.25$ ($\eta_R = \frac{E_R}{E_R+G'}$, where E_R is the radiated energy and G' is the seismologically observed fracture energy), relative to ordinary earthquakes (Kanamori, 1972; Venkataraman and Kanamori, 2004). Low radiation efficiency requires an earthquake to dissipate more energy during fault propagation (i.e., W_b) relative to the energy radiated as seismic waves. The compiled results are relevant to tsunami earthquakes because they rupture the shallow portions of subduction zones, where the plate boundary fault zone may contain similar materials to samples from input stratigraphic sections. Although we are not able to evaluate η_R in the experiments because E_R is not measured (and we lack τ_0 for many experiments), in general, high W_b (as a proxy for G') materials may experience tsunami-type events, but low W_b materials would not. As subduction décollements are likely fluid-saturated, Figure 6 suggests that the primary characteristic that might explain tsunami earthquake slip is how well-drained the fault zone is (Ma, 2012), rather than lithology or clay content. If wet gouges predominate in subduction décollements, W_b dissipated on-fault is unlikely to be large, suggesting off-fault damage is also important. Cascadia input materials that contain relatively less clay and exhibit moderately large W_b may therefore be good candidates for hosting tsunami-type events.

2.5 Conclusions

High velocity rotary shear experiments on input sediments from Cascadia, individual clay species, and experiments on other gouges and intact rocks compiled from the literature have shown that:

1. Mudstones and sandstone from the input sediments at Cascadia are relatively strong (μ_p = 0.40-0.46 and μ_p = 0.67, respectively) and have similar breakdown work values (0.1-2 MJ/m^2) over a range of normal stresses
2. For all sample types, breakdown stress drop increases linearly with normal stress and thermal weakening distance decreases according to a power law dependence on normal stress
3. For all sample types, breakdown work is independent of normal stress due to a tradeoff between increasing breakdown stress drop and decreasing thermal weakening distance
4. Breakdown work varies by several orders of magnitude between wet gouges (0.0001-4 MJ/m^2), dry gouges (0.1-5 MJ/m^2), and intact rocks (2-40 MJ/m^2)

There is an order of magnitude difference in the frictional behavior of input sediments from different subduction margins where wet, clay-present gouges show both the greatest range of breakdown work as well as the lowest values. At Cascadia, lithology plays a limited role in discriminating the structural level in which an earthquake is likely to propagate due to the lack of variability in the frictional behavior and breakdown work between mudstones and sandstones. The relatively high frictional strength and moderate breakdown work of the input sediments from the Cascadia margin suggest that it may be less susceptible to hosting very large amounts of shallow slip or dynamic overshoot, although this may be mediated by more frictionally unstable behavior of the gouge and a greater amount of elastic stored energy at shallow depth due to the higher strength of the gouges.

2.6 References

Abercrombie, R.E., Rice, J.R., 2005. Can observations of earthquake scaling constrain slip weakening? Geophys. J. Int. 162, 406-424. https://doi.org/10.1111/j.1365-246X.2005.02579.x.

Aretusini, S., Spagnuolo, E., Dalconi, M.C., Di Toro, G., Rutter, E.H., 2019. Water availability and deformation processes in smectite-rich gouges during seismic slip. J. Geophys. Res. Solid Earth 124, 10,855-810,876. https://doi.org/10.1029/2019JB018229.

Bletery, Q., Sladen, A., Jiang, J., Simons, M., 2016. A Bayesian source model for the 2004 great Sumatra-Andaman earthquake. J. Geophys. Res. Solid Earth 121, 5116-5135. https://doi.org/10.1002/2016JB012911.

Carson, B., Westbrook, G.K., Musgrave, R.J., Suess, E., 1995. Proceedings of the Ocean Drilling Program, Scientific Results, Vol.146 (Part 1). Ocean Drilling Program, College Station, TX.

Chester, F.M., Rowe, C., Ujiie, K., Kirkpatrick, J., Regalla, C., Remitti, F., Moore, J.C., Toy, V., Wolfson-Schwehr, M., Bose, S., Kameda, J., Mori, J.J., Brodsky, E.E., Eguchi, N., Toczko, S., Expedition 343 and 343T Scientists, 2013. Structure and composition of the plate-boundary slip zone for the 2011 Tohoku-Oki earthquake. Science 342, 1208-1211. https://doi.org/10.1126/science.1243719.

Cocco, M., Bizzarri, A., 2002. On the slip-weakening behavior of rate- and state dependent constitutive laws. Geophys. Res. Lett. 29, 1516. https://doi.org/10.1029/2001GL013999.

Cubas, N., Souloumiac, P., Singh, S.C., 2016. Relationship link between landward vergence in accretionary prisms and tsunami generation. Geology 44, 787-790. https://doi.org/10.1130/G38019.1.

Di Toro, G., Han, R., Hirose, T., De Paola, N., Nielsen, S., Mizoguchi, K., Ferri, F., Cocco, M., Shimamoto, T., 2011. Fault lubrication during earthquakes. Nature 471, 494-498. https://doi.org/10.1038/nature09838.

Faulkner, D.R., Mitchell, T.M., Behnsen, J., Hirose, T., Shimamoto, T., 2011. Stuck in the mud? Earthquake nucleation and propagation through accretionary forearcs. Geophys. Res. Lett. 38, 1-5. http://doi.wiley.com/10.1029/2011GL048552.

Fisher, A., Davis, E.E., Escutia, C., 2000. Proceedings of the Ocean Drilling Program, Scientific Results, Vol.168. Ocean Drilling Program, College Station, TX.

French, M.E., Kitajima, H., Chester, J.S., Chester, F.M., Hirose, T., 2014. Displacement and dynamic weakening processes in smectite-rich gouge from the Central Deforming Zone of the San Andreas Fault. J. Geophys. Res. Solid Earth 119, 1777-1802. https://doi.org/10.1002/2013JB010757.

Goldfinger, C., Nelson, C.H., Morey, A.E., Johnson, J.E., Patton, J.R., Karabanov, E., Gutierrez-Pastor, J., Eriksson, A., Gracia, E., Dunhill, G., Enkin, R., Dallimore, A., Vallier, T., 2012. Turbidite Event History - Methods and Implications for Holocene Paleoseismicity of the Cascadia Subduction Zone. U.S. Geological Survey, p. 170.

Han, S., Bangs, N.L., Carbotte, S.M., Saffer, D.M., Gibson, J.C., 2017. Links between sediment consolidation and Cascadia megathrust slip behaviour. Nat. Geosci. 10, 954-959. https://doi.org/10.1038/s41561-017-0007-2.

Hirose, T., Shimamoto, T., 2005. Growth of molten zone as a mechanism of slip weakening of simulated faults in gabbro during frictional melting. J. Geophys. Res. Solid Earth 110, B05202. https://doi.org/10.1029/2004JB003207.

Ida, Y., 1972. Cohesive force across the tip of a longitudinal-shear crack and Griffith's specific surface energy. J. Geophys. Res. 77, 3796-3805. https://doi.org/10.1029/JB077i020p03796.

Ikari, M., Kopf, A.J., 2017. Seismic potential of weak, near-surface faults revealed at plate tectonic slip rates. Sci. Adv. 3, e1701269. https://doi.org/10.1126/sciadv.1701269.

Ikari, M., Kopf, A.J., Hüpers, A., Vogt, C., 2018. Lithologic control of frictional strength variations in subduction zone sediment inputs. Geosphere 12, 604-625. https://doi.org/10.1130/GES01546.1.

Ikari, M.J., Saffer, D.M., Marone, C., 2009. Frictional and hydrologic properties of clay-rich fault gouge. J. Geophys. Res. Solid Earth 114, B05409. https://doi.org/10.1029/2008JB006089.

Kanamori, H., 1972. Mechanism of tsunami earthquakes. Phys. Earth Planet. Inter. 6, 346-359. https://doi.org/10.1016/0031-9201(72)90058-1.

Kirkpatrick, J.D., Rowe, C.D., Ujiie, K., Moore, J.C., Regalla, C., Remitti, F., Toy, V., Wolfson-Schwehr, M., Kameda, J., Bose, S., Chester, F.M., 2015. Structure and lithology of the Japan Trench subduction plate boundary fault. Tectonics 34, 53-69. https://doi.org/10.1002/2014TC003695.

Kitajima, H., Chester, J.S., Chester, F., Shimamoto, T., 2010. High‐speed friction of disaggregated ultracataclasite in rotary shear: Characterization of frictional heating, mechanical behavior, and microstructure evolution. J. Geophys. Res. 115, B08408. https://doi.org/10.1029/2009JB007038.

Lay, T., 2018. A review of the rupture characteristics of the 2011 Tohoku-oki Mw 9.1 earthquake. Tectonophysics 733, 4-36. https://doi.org/10.1016/j.tecto.2017.09.022.

Li, S., Wang, K., Wang, Y., Jiang, Y., Dosso, S.E., 2018. Geodetically inferred locking state of the Cascadia megathrust based on a viscoelastic earth model. J. Geophys. Res. Solid Earth 123, 8056-8072. https://doi.org/10.1029/2018JB015620.

Ma, S., 2012. A self‐consistent mechanism for slow dynamic deformation and tsunami generation for earthquakes in the shallow subduction zone. Geophys. Res. Lett. 39, L11310. https://doi.org/10.1029/2012GL051854.

McGuire, J.J., Collins, J.A., Davis, E., Becker, K., Heesemann, M., 2018. A lack of dynamic triggering of slow slip and tremor indicates that the shallow Cascadia megathrust offshore Vancouver Island is likely locked. Geophys. Res. Lett. 45, 1-9. https://doi.org/10.1029/2018GL079519.

Mizoguchi, K., Hirose, T., Shimamoto, T., Fukuyama, E., 2007. Reconstruction of seismic faulting by high-velocity friction experiments: An example of the 1995 Kobe earthquake. Geophys. Res. Lett. 34, L01308. https://doi.org/10.1029/2006GL027931.

Moore, J.C., Plank, T.A., Chester, F.M., Polissar, P.J., Savage, H.M., 2015. Sediment provenance and controls on slip propagation: Lessons learned from the 2011 Tohoku and other great earthquakes of the subducting northwest Pacific plate. Geosphere 11, 533-541. https://doi.org/10.1130/GES01099.1.

Nielsen, S., Spagnuolo, E., Smith, S.A.F., Violay, M., Di Toro, G., Bistacchi, A., 2016. Scaling in natural and laboratory earthquakes. Geophys. Res. Lett. 43, 1504-1510. https://doi.org/10.1002/2015GL067490.

Noda, H., Dunham, E.M., Rice, J.R., 2009. Earthquake ruptures with thermal weakening and the operation of major faults at low overall stress levels. J. Geophys. Res. 114, B07302. https://doi.org/10.1029/2008JB006143.

Obana, K., Scherwath, M., Yamamoto, Y., Kodaira, S., Wang, K., Spence, G., Riedel, M., Kao, H., 2015. Earthquake activity in northern Cascadia subduction zone off Vancouver Island revealed by ocean-bottom seismograph observations. Bull. Seismol. Soc. Am. 105, 489-495. https://doi.org/10.1785/0120140095.

Oleskevich, D.A., Hyndman, R.D., Wang, K., 1999. The updip and downdip limits to great subduction earthquakes: Thermal and structural models of Cascadia, south Alaska, SW Japan, and Chile. J. Geophys. Res. Solid Earth 104, 14965-14991. https://doi.org/10.1029/1999JB900060.

Palmer, A.C., Rice, J.R., 1973. The growth of slip surfaces in the progressive failure of over-consolidated clay. Proc. Roy. Soc. Lond. A. 332, 527-548. https://doi.org/10.1098/rspa.1973.0040.

Rabinowitz, H.S., Savage, H.M., Polissar, P.J., Rowe, C.D., Kirkpatrick, J.D., 2020. Earthquake slip surfaces identified by biomarker thermal maturity within the 2011 Tohoku-Oki earthquake fault zone. Nat. Comm. 11, 1-9. https://doi.org/10.1038/s41467-020-14447-1.

Reches, Z., Lockner, D.A., 2010. Fault weakening and earthquake instability by powder lubrication. Nature 467, 452-455. https://doi.org/10.1038/nature09348.

Rice, J.R., 2006. Heating and weakening of faults during earthquake slip. J. Geophys. Res. Solid Earth 111, B05311. https://doi.org/10.1029/2005JB004006.

Satake, K., Wang, K., Atwater, B.F., 2003. Fault slip and seismic moment of the 1700 Cascadia earthquake inferred from Japanese tsunami descriptions. J. Geophys. Res. Solid Earth 108, 2535. https://doi.org/10.1029/2003JB002521.

Savage, H.M., Rabinowitz, H.S., Spagnuolo, E., Aretusini, S., Polissar, P.J., Di Toro, G., 2018. Biomarker thermal maturity experiments at earthquake slip rates. Earth Planet. Sci. Lett. 502, 253-261. https://doi.org/10.1016/j.epsl.2018.08.038.

Sawai, M., Hirose, T., Kameda, J., 2014. Frictional properties of incoming pelagic sediments at the Japan Trench: implications for large slip at a shallow plate boundary during the 2011 Tohoku earthquake. Earth Planets Space 66, 65. https://doi.org/10.1186/1880-5981-66-65.

Selvadurai, P.A., 2019. Laboratory insight into seismic estimates of energy partitioning during dynamic rupture: An observable scaling breakdown. J. Geophys. Res. Solid Earth 124, 1-30. https://doi.org/10.1029/2018JB017194.

Sone, H., Shimamoto, T., 2009. Frictional resistance of faults during accelerating and decelerating earthquake slip. Nat. Geosci. 2, 705-708. https://doi.org/10.1038/ngeo637.

Tanikawa, W., Mukoyoshi, H., Tadai, O., 2012. Experimental investigation of the influence of slip velocity and temperature on permeability during and after high-velocity fault slip. J. Struct. Geol. 38, 90-101. https://doi.org/10.1016/j.jsg.2011.08.013.

Tinti, E., Spudich, P., Cocco, M., 2005. Earthquake fracture energy inferred from kinematic rupture models on extended faults. J. Geophys. Res. 110, B12303. https://doi.org/10.1029/2005JB003644.

Tsutsumi, A., Shimamoto, T., 1997. High-velocity frictional properties of gabbro. Geophys. Res. Lett. 24, 699-702. https://doi.org/10.1029/97GL00503.

Ujiie, K., Tanaka, H., Saito, T., Tsutsumi, A., Mori, J.J., Toczko, S., Expedition 343 and 343T Scientists, 2013. Low coseismic shear stress on the Tohoku-Oki megathrust determined from laboratory experiments. Science 342, 1211-1214. https://doi.org/10.1126/science.1243485.

Ujiie, K., Tsutsumi, A., 2010. High‐velocity frictional properties of clay‐rich fault gouge in a megasplay fault zone, Nankai subduction zone. Geophys. Res. Lett. 37, L24310. https://doi.org/10.1029/2010GL046002.

Venkataraman, A., Kanamori, H., 2004. Observational constraints on the fracture energy of subduction zone earthquakes. J. Geophys. Res. Solid Earth 109, B05302. https://doi.org/10.1029/2003JB002549.

Viesca, R.C., Garagash, D.I., 2015. Ubiquitous weakening of faults due to thermal pressurization. Nat. Geosci. 8, 875-879. https://doi.org/10.1038/ngeo2554.

Vrolijk, P., 1990. On the mechanical role of smectite in subduction zones. Geology 18, 703-707. https://doi.org/10.1130/0091-7613(1990)018<0703:OTMROS>2.3.CO;2.

Wang, K., Hu, Y., He, J., 2012. Deformation cycles of subduction earthquakes in a viscoelastic Earth. Nature 484, 327-332. https://doi.org/10.1038/nature11032.

Yao, L., Ma, S., Platt, J.D., Niemeijer, A., Shimamoto, T., 2016. The crucial role of temperature in high-velocity weakening of faults: Experiments on gouge using host blocks with different thermal conductivities. Geology 44, 63-66. https://doi.org/10.1130/G37310.1.

CHAPTER 3

Structural and metamorphic history of the Leech River Shear Zone, Vancouver Island, British Columbia

Seyler, C.E., Kirkpatrick, J.D., Licht, A., Šilerová, D., Regalla, C., Structural and metamorphic history of the Leech River Shear Zone, Vancouver Island, British Columbia, in preparation for submission to Tectonics.

Abstract

The Leech River Shear Zone (LRSZ) on southern Vancouver Island separates the metasedimentary schists of the Leech River Complex from the Siletz-Crescent Terrane, an oceanic plateau formed near the Kula/Resurrection-Farallon Ridge. Previous work links the formation of the Siletz-Crescent Terrane to the Yellowstone Hotspot, implying that the LRSZ presents an opportunity to examine plate interface conditions and deformation during subduction of thick, hot oceanic crust. We present field, microstructural, petrological, and geochronological observations that constrain the structural and metamorphic history of LRSZ. The mylonitic LRSZ straddles the lithologic contact between the Leech River Schist and basalts of the Siletz-Crescent Terrane. Foliation orientations, a steeply plunging stretching lineation, and kinematic indicators all suggest sinistral-reverse motion. Compositions of garnet in the schist and amphibole in the metabasalt record syn-kinematic prograde growth at peak temperature and pressure conditions of ~600 °C and ~850 MPa. The peak metamorphic conditions require elevated geotherms that are consistent with models of plate motions that position the Farallon-Kula/Resurrection Ridge and Yellowstone Hotspot in the Pacific Northwest in the early Eocene (~50 Ma). Detrital zircon U-Pb age distributions for the Leech River Schist correlate with Mesozoic volcanic arcs and the Upper Nanaimo Group that

unconformably overlies the Wrangellia Terrane to the north. Our ages support Late Cretaceous deposition of the schist as an accretionary complex in the near-trench environment and indicate the schist originated near the Nanaimo Group and Wrangellia Terrane and is therefore not allochthonous to most of Vancouver Island. Our observations establish the LRSZ as the downdip portion of a paleo-plate interface representing an Eocene subduction zone.

3.1 Introduction

The northern Cordillera in Canada and the U.S.A. is the classic example of an accretionary orogen, consisting of an assemblage of distinct tectonostratigraphic terranes. Faults and shear zones define the contacts between the majority of terranes, so terrane-bounding structures are common. Because many of the terranes represent allochthonous Paleozoic to Cenozoic magmatic arcs, microcontinents, and oceanic plate fragments that were incorporated into the orogen through a series of collisional and accretionary episodes, many of the terrane bounding structures must represent paleo-plate boundaries. If tectonic contexts can be established for these structures, they can be used to interrogate the mechanical conditions and processes active in modern systems as well as to develop important constraints on the tectonic history of the surrounding regions.

Accretion of the Siletz-Crescent Terrane to the North American margin occurred during subduction of the Farallon oceanic plate and impacted the deformation of the subduction forearc and regional tectonics of the upper plate. The Siletz-Crescent Terrane, which extends from Vancouver Island in British Columbia to Oregon, consists of a tens of kilometers-thick sequence of basaltic volcanics and intrusive suites. Trace element and rare earth element geochemistry of the basalts are consistent with minimal crustal contamination and a slightly enriched mantle source

(Phillips et al., 2017). These characteristics, along with the thickness of the mafic units, indicate the terrane represents a portion of a large igneous province that formed above a mantle plume, potentially the Yellowstone Hotspot, near the Kula/Resurrection-Farallon Ridge (Phillips et al., 2017; Wells et al., 2014). The compositions and ages of forearc intrusions on southern Vancouver Island and the geochemically diagnostic intrusive suites in eastern Washington and British Columbia are evidence for the development of a slab window at ~50 Ma (Breitsprecher et al., 2003), soon after the eruption of the Siletz-Crescent volcanics. The Siletz-Crescent Terrane rocks were therefore likely developed on young, overthickened oceanic crust, which was hot and relatively buoyant and consequently underplated rather than subducted. Underplating of the Siletz-Crescent Terrane caused renewed fault activity and uplift in the upper plate (Eddy et al., 2016) and likely coincided with the onset of oroclinal bending in the forearc (Johnston and Acton, 2003), which continues today (Li et al., 2018; Morell et al., 2017).

The Leech River Fault (LRF), exposed on southern Vancouver Island, is the terrane-bounding fault that juxtaposes the Leech River Complex (LRC) of the Pacific Rim Terrane to the north and the Metchosin Igneous Complex (MIC) of the Siletz-Crescent Terrane to the south. The recent work that established the Siletz-Crescent represents part of an oceanic plate (Phillips et al., 2017) implies that this fault represents a former subduction interface. However, the structural record of accretion is poorly constrained and the kinematics and relative timing of deformation along the LRF still need to be reconciled with this tectonic history. Seismic reflection images show the contact between the LRC and MIC dips to the north under Vancouver Island and projects to the surface trace of the Leech River Fault (Clowes et al., 1987). Combined with the ages of the LRC (inferred Mesozoic; Fairchild and Cowan, 1982) and MIC (Eocene based on radiometric ages of pillow

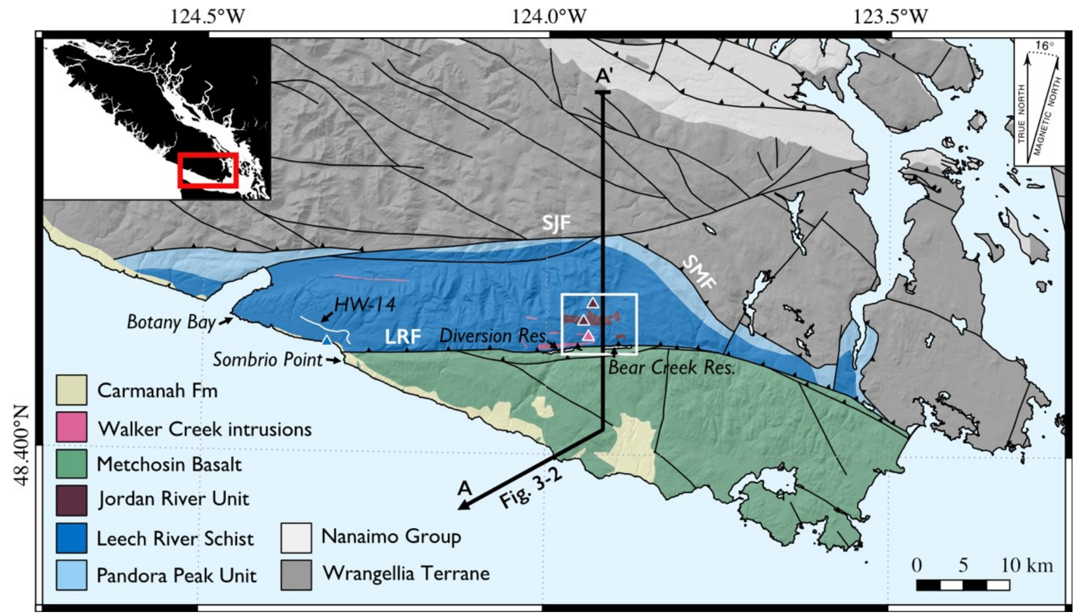

Figure 3-1: Geologic map of field area. Simplified geologic map of southern Vancouver Island (adapted from Cui et al., 2017; Groome et al., 2003; Muller, 1980; Rusmore, 1982). White box outlines primary study area. Triangles represent locations of samples collected for U-Pb zircon geochronology. LRF—Leech River Fault; SJF—San Juan Fault; SMF—Survey Mountain Fault.

basalts; Duncan, 1982; McCrory and Wilson, 2013), this geometry suggests the LRF is a thrust fault. However, previous field data suggested dominantly strike-slip motion (Fairchild and Cowan, 1982) and previous work on the inboard contact of the Siletz-Crescent Terrane has concentrated on southern exposures (e.g., Eddy et al., 2016; McCrory and Wilson, 2013; Wells et al., 2014).

In this study, we use field and petrological observations of the LRF and surrounding Leech River Schist and Metchosin Basalt to establish the tectonic history of the LRF. Field and microstructural observations are used to establish the kinematics of the deformation within the rocks deformed by the LRF, which provide a direct test of a thrust vs. strike-slip regime. We use a suite of geothermometers and petrological indicators to develop thermal histories for the rocks and determine whether they are consistent with subduction-related burial. We also measured the ages of detrital zircons in the Leech River Schist to establish the age of its deposition and place constraints on the timing of the tectonic activity involved in docking of the Siletz-Crescent Terrane, as represented by the Metchosin Basalt on Vancouver Island. The results establish the LRF as an underplated paleo-subduction megathrust, which was active in the Eocene, consistent with plate reconstruction models that treat the Metchosin Basalt as an underplated portion of the subducted Farallon plate.

3.2 Geologic setting

3.2.1 Leech River Complex

The Leech River Fault (LRF) is bounded on the north by the Leech River Complex (LRC). The LRC, together with the Pandora Peak Unit and Pacific Rim Complex, collectively make up the Pacific Rim Terrane, a southern correlative of the Chugach-Prince William composite terrane in Alaska (Cowan, 2003; Cowan et al., 1997). The LRC is an approximately 10 km-thick package of metasedimentary rocks that crop out in an east-west band on southern Vancouver Island (Fig. 3-1). The LRC is bounded to the north by the San Juan and Survey Mountain faults, which juxtapose the LRC with the Pandora Peak Unit of the Pacific Rim Terrane and the Wrangellia Terrane of the Insular Belt, and to the south by the Leech River Fault against the Metchosin Igneous Complex. Because the LRC is fault-bounded, its tectonic origin and kinematic relationship to deformation on the LRF are debated.

The LRC is composed of the Leech River Schist (LRS), the Jordan River Unit, the Tripp Creek Metabasite, and the Walker Creek intrusions. The LRS is a light to dark grey schist composed of intercalated metapelitic and metapsammitic layers. Based on the assemblage of discontinuous layers of metamorphosed shales and sandstones with minor chert and basaltic volcanics, the LRS was interpreted as a submarine, near-continental margin turbidite sequence deposited near a source of basalt, such as a spreading ridge (Fairchild and Cowan, 1982; Muller, 1977b, 1980). Fairchild and Cowan (1982) reported transposed sedimentary layering, aligned metapsammitic lenses within a metapelitic matrix, and two generations of folds with strong axial planar foliation parallel to the compositional layering. These features were interpreted to result from regional north-south shortening, though second-generation folds were reported as more strongly developed in the southern part of the unit (Fairchild and Cowan, 1982).

The Jordan River Unit is a quartz-feldspar-biotite schist that has been inconsistently interpreted as both the largest body of metasandstone in the LRS (i.e., the Valentine metasandstone in Fairchild and Cowan, 1982; Muller, 1980), and as a plagioclase-rich peraluminous metagranodiorite intrusion derived from anatexis of the LRS with a titanite U-Pb crystallization age of 88 Ma (Groome et al., 2003). The Tripp Creek Metabasite is an actinolite-plagioclase-quartz-garnet schist interpreted as an intrusive unit due to the presence of foliated LRS xenoliths (Groome et al., 2003). The Jordan River Unit and Tripp Creek Metabasite have a schistosity parallel to the foliation in the LRS, suggesting their formation is pre- to syn-kinematic with deformation of the complex. The Walker Creek intrusions are a suite of tonalite, trondhjemite, and granodiorite dikes and sills present in the southern portion of the LRS. Deformation of these intrusions is non-uniform, with some dikes displaying schistosity parallel to the foliation in the LRS while others remain undeformed, suggesting syn- to post-kinematic magmatism (Groome et al., 2003). These intrusions have zircon U-Pb crystallization ages ranging from 51-47 Ma, and their geochemical signatures suggest they are derived from anatexis of the LRS (Groome et al., 2003).

The depositional age and metamorphic conditions of the LRS are under-constrained by the available geochronologic and petrologic data. The LRS has a reported maximum depositional age of 103 Ma derived from the youngest detrital zircon (Groome et al., 2003). This age estimate is limited by the small number of grains analyzed (n = 8), and a sedimentary origin of the Jordan River Unit also requires re-evaluation of its previously reported age. The metamorphic grade of the LRS has been shown to increase from greenschist facies in the north to amphibolite facies in the south, with peak conditions syn- to post-kinematic with regional deformation (Fairchild and Cowan, 1982; Groome et al., 2003). The pressure and temperature experienced by the schist are estimated at <350 MPa based on the presence of andalusite and up to 500-600 °C within contact aureoles around intrusive units (Groome et al., 2003).

3.2.2 Metchosin Igneous Complex

The LRF is bounded on the south by the Metchosin Igneous Complex (MIC). The MIC is part of the Siletz-Crescent Terrane, which includes the MIC on southern Vancouver Island, the Crescent Formation of Washington, the Coast Range Volcanic Province of Washington and Oregon, and the Siletz River Volcanics of Oregon (Duncan, 1982; Irving, 1979; McCrory and Wilson, 2013; Simpson and Cox, 1977). The MIC consists of a 3 km-thick ophiolite pseudostratigraphy consisting of gabbro stock (Sooke Gabbros), sheeted dikes, and a sequence of basalt flows that transitions from submarine to subaerial up-section (Massey, 1986). Whole rock trace element geochemistry is transitional between N-MORB and E-MORB signatures, suggesting both spreading ridge- and mantle plume- related magmatism (Duncan, 1982; Phillips et al., 2017; Timpa et al., 2005). The age of the complex ranges from 58-52 Ma based on Ar-Ar fusion dates and U-Pb zircon dates (Duncan, 1982; Massey, 1986; Yorath et al., 1999). Temperature estimates from amphibole compositions and Al^{iv}-in-chlorite geothermometry suggest the metamorphic facies in the complex increases from prehnite-actinolite grade in the east to amphibolite grade in the west along a ~5-10 °C/km gradient (Timpa et al., 2005). This gradient was interpreted as the result of metamorphism during tectonic emplacement of the MIC followed by differential exhumation (Timpa et al., 2005).

Duncan (1982) proposed an oceanic plateau origin for the terrane based on the age progression from youngest dates in the center and oldest dates to the north and south and the transitional geochemical signature. This age pattern suggests the Siletz-Crescent Terrane represents a chain of seamounts that formed as part of a hotspot track produced by the Yellowstone Hotspot beneath the Kula-Farallon Ridge (Duncan, 1982). This hypothesis was previously rejected in favor of an extensional volcanism origin for the terrane based on the anomalous thickness of the terrane revealed by seismic transects, which ranges from 6-10 km offshore and beneath Vancouver Island (Hyndman et al., 1990; Tréhu et al., 1994) and up to 27±5 km beneath Oregon (Fleming and Tréhu, 1999), and the incompatibility between the age range (64-47 Ma) and the fast spreading rate of the Kula-Farallon Ridge (Babcock et al., 1992; Wells et al., 1984). However, more recent age dating and a re-evaluation of previously published ages has revised the age range for the terrane to 55-49 Ma (Eddy et al., 2017; McCrory and Wilson, 2013; Wells et al., 2014 and references therein). The oceanic plateau origin has also been supported by additional geologic mapping and plate reconstruction modelling (McCrory and Wilson, 2013; Wells et al., 2014), and geochemistry (Phillips et al., 2017). These data support the hypothesis that the Siletz-Crescent Terrane represents an accreted oceanic plateau that was formed near the Kula/Resurrection-Farallon Ridge by a near-ridge mantle plume, most likely the Yellowstone Hotspot (Duncan, 1982; Eddy et al., 2016; Eddy et al., 2017; McCrory and Wilson, 2013; Phillips et al., 2017; Wells et al., 2014). Shortly after its formation, the Washington and Oregon portion of the terrane docked to North America by 51-48 Ma based on the coccolithophores present in the overlying strata (Wells et al., 2014) and the sedimentary record of changing paleoflow direction (Eddy et al., 2016). On Vancouver Island, the terrane docked prior to 45-42.5 Ma based on $^{40}Ar/^{39}Ar$ cooling ages in mica that record exhumation of the Leech River Schist (Groome et al., 2003).

3.2.3 Leech River Fault

The Leech River Fault is a north-dipping thrust fault that juxtaposes the Leech River Complex against the Metchosin Igneous Complex (Fig. 3-2a) (Clowes et al., 1987; Matharu et al., 2014). This structure has been previously reported as a fault zone with two to four discrete strike slip faults, lacking any fault gouge, breccia, or mylonitization (Fairchild and Cowan, 1982) as well as a left-lateral shear zone composed of mylonites ("Bear Creek Shear Zone" in Groome, 2000). Quaternary reactivation of the Leech River Fault as a wide zone of strike-slip faults has been documented through fault scarp identification (Morell et al., 2017), microseismicity (Li et al., 2018), and paleoseismic trenching (Harrichhausen et al., 2021). Here, we focus on the ancient structure that established the tectonic contact between the LRS and MIC. For clarity, we will term this structure the “Leech River Shear Zone” (LRSZ) to differentiate it from the recently active Leech River Fault.

3.3 Methods

Polished thin sections were prepared perpendicular to the foliation and parallel to the lineation as well as perpendicular to the lineation from oriented samples. Geochemical analyses were conducted on representative samples of the schist and metabasalt mylonites from the LRSZ and measured with 5 wavelength-dispersive spectrometers on either a JEOL 8900 electron microprobe or Cameca SX100 Five-FE electron microprobe. Garnet compositions were measured on the JEOL microprobe with an accelerating voltage of 20 kV, a beam current of 30 nA, and a beam diameter of 5 µm. Biotite compositions from samples CS15-DR21 and CS15-SW06 were measured on the JEOL microprobe with an accelerating voltage of 15 kV, a beam current of 20 nA, and a beam diameter = 10 µm. Biotite from samples CS18-25 and CS18-32 were measured on the Cameca microprobe with an accelerating voltage of 15 kV, a beam current of 20 nA, and a beam diameter of 5 µm. Amphibole compositions were measured on the Cameca microprobe with an accelerating voltage of 20 kV, a beam current of 4 nA, and a beam diameter of 5 µm. Amphibole compositions were calculated based on the recommendations and classification scheme approved by the Commission on New Minerals Nomenclature and Classification (CNMNC) of the International Mineralogical Association (Hawthorne et al., 2012; Locock, 2014). Plagioclase compositions were measured on the Cameca microprobe with an accelerating voltage of 15 kV, a beam current of 20 nA, and a beam diameter of 5 µm. Pseudosection modeling was conducted with Perple_X 6.8.3 (Connolly, 2005) using the internally consistent thermodynamic database of Holland and Powell (1998), revised by the authors in 2004. Bulk composition was input from whole rock fusion XRF analyses conducted by Actlabs on a representative sample.

Detrital zircon ages were determined for samples of the Leech River Schist, Jordan River Unit, and Walker Creek intrusions. Detailed data acquisition and reduction protocols are described in Shekut and Licht (2020). Zircons were extracted by heavy mineral separation, including concentration with a Holman-Wilfley™ gravity table, density separation with methylene iodide, and magnetic separation with a Frantz™ Magnetic Barrier separator. Data was collected using a laser-ablation inductively-coupled-plasma mass-spectrometry (LA-ICP-MS), using an iCAP-RQ Quadrupole ICP-MS coupled to an Analyte G2 excimer laser at the University of Washington, using a spot diameter of 25 microns and Plešovice zircons as calibration reference material (Sláma et al., 2008). Data reduction was conducted with *Iolite* (Version 3.5), using their *U_Pb_Geochron4* Data Reduction Scheme to calculate U-Pb dates uncorrected for common lead (Paton et al., 2010). Uncertainties for all samples were calculated using a modified version of the method of Matthews and Guest (2017) that takes into account the impact of ^{207}Pb beam intensity on date uncertainties (Horstwood et al., 2016). The dates used for plotting are $^{206}Pb/^{238}U$ for dates <1400 Ma and $^{207}Pb/^{206}Pb$ for dates >1400 Ma. Dates >300 Ma were screened for concordance using a discordance filter at >20% discordance (<80% concordance) and >5% reverse discordance (>105% concordance); we used the $^{206}Pb/^{238}U$ vs $^{207}Pb/^{235}U$ ratio to calculate discordance for dates <1300 Ma, and the $^{206}Pb/^{238}U$ vs. $^{207}Pb/^{206}Pb$ ratio for older dates. A subset of zircon grains from each sample were imaged using cathodoluminescence to assess their growth textures (Fig. B-1). Maximum depositional ages (MDA) were calculated from the youngest age population of overlapping dates ($n \geq 3$) using the *TuffZirc* application within IsoPlot (Ludwig, 2003).

3.4 Field and microstructural observations

The Leech River Shear Zone (LRSZ) follows the lithologic contact between the Leech River Schist and the Metchosin Basalt, which extends from Sombrio Point to Leechtown (Fig. 3-1). At map-scale, the LRSZ strikes east-west and dips steeply to the north, consistent with observations from reflection seismology. Our observations and data were collected from a study area that extends

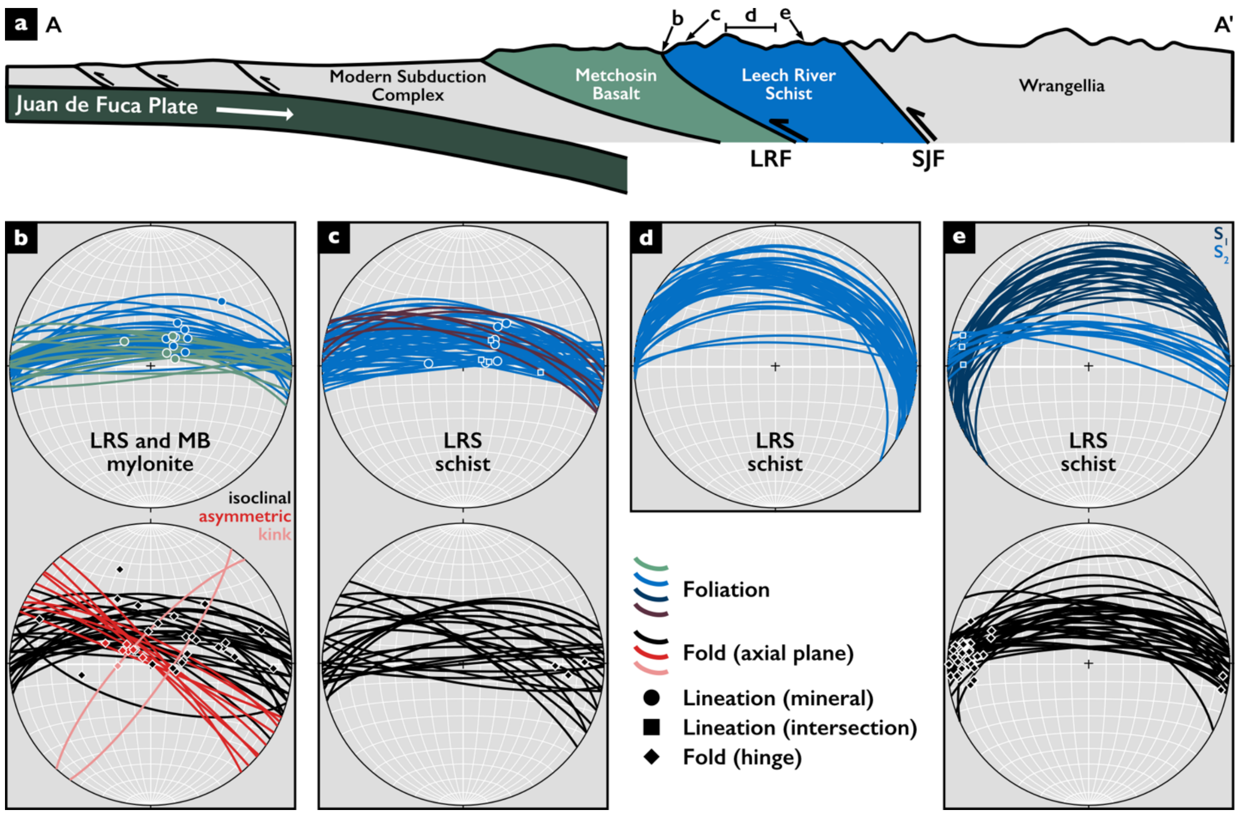

Figure 3-2: Geologic cross-section and structural data. a) Simplified geologic cross-section (adapted from Clowes et al., 1987; Hyndman et al., 1990). Stereonet projections of foliation, lineation, and fold orientations: **b)** Foliation, lineation, and three sets of fold orientations within the Leech River Schist and Metchosin Basalt mylonites (Note that isoclinal folds with shallowly plunging hinges are underrepresented due to lack of subvertical exposures); **c)** Foliation, lineation, and fold orientations within the Leech River Schist directly north of the Diversion and Bear Creek reservoirs; **d)** Foliation orientations within the Leech River Schist along a north-south transect on HW-14 between Botany Bay and Sombrio Point; **e)** Foliation, lineation, and fold orientations in the Leech River Schist near Botany Bay. Foliation and lineation colors coordinated to map legend colors of Fig. 3-1.

from the west coast south of Port Renfrew to the center of the island near the Diversion and Bear Creek reservoirs.

3.4.1 Leech River Schist (hanging wall)

In this section, we describe the structural fabrics of the schist on a north-south transect to differentiate between regional deformation and deformation related to motion on the LRSZ. As noted by Fairchild and Cowan (1982), the schist contains at least two distinct foliations. However, the deformation varies spatially, so we describe the schist along the transect in two regions: Botany Bay (Fig 3-2e) and north of the Diversion and Bear Creek reservoirs (Fig. 3-2c). The distance from the shear zone for both of these regions is shown on Figure 3-2a.

Near Botany Bay, the schist is characterized by a block-in-matrix fabric with quartz- and plagioclase-rich metapsammitic blocks hosted in a phyllosilicate-rich metapelitic matrix (Fig. 3-3a-d). Some larger blocks contain evidence for graded bedding and crossbeds indicating that the lithologic variation represents primary sedimentary bedding (S_0), which included interbedded sand-, silt-, and clay-sized layers. The present-day layer discontinuity and strong deformation fabrics in the matrix imply that bedding was tectonically disrupted and transposed into the block-in-matrix fabric. Block sizes range from centimeter- to meter-scale and larger blocks commonly contain quartz veins that terminate at the block edges. Two foliation orientations are present, with the dominant foliation (S_1) defined by parallel long axes of blocks forming an apparent layering that is parallel to a continuous cleavage in the metapelitic matrix, and a less pronounced, spaced cleavage (S_2) in the metapelitic matrix (Fig. 3-3a). Both S_1 and S_2 strike approximately east-west, but S_2 is more steeply dipping (Fig. 3-2e and 3-3a). These two foliations locally produce an intersection lineation that plunges shallowly to the west. Some quartz veins within the blocks are tightly folded with axial surfaces parallel to the S_1 foliation. Asymmetric isoclinal folds of thin metapsammitic blocks intrafolial with S_1 are also observed, which indicate that S_1 is parallel to S_0

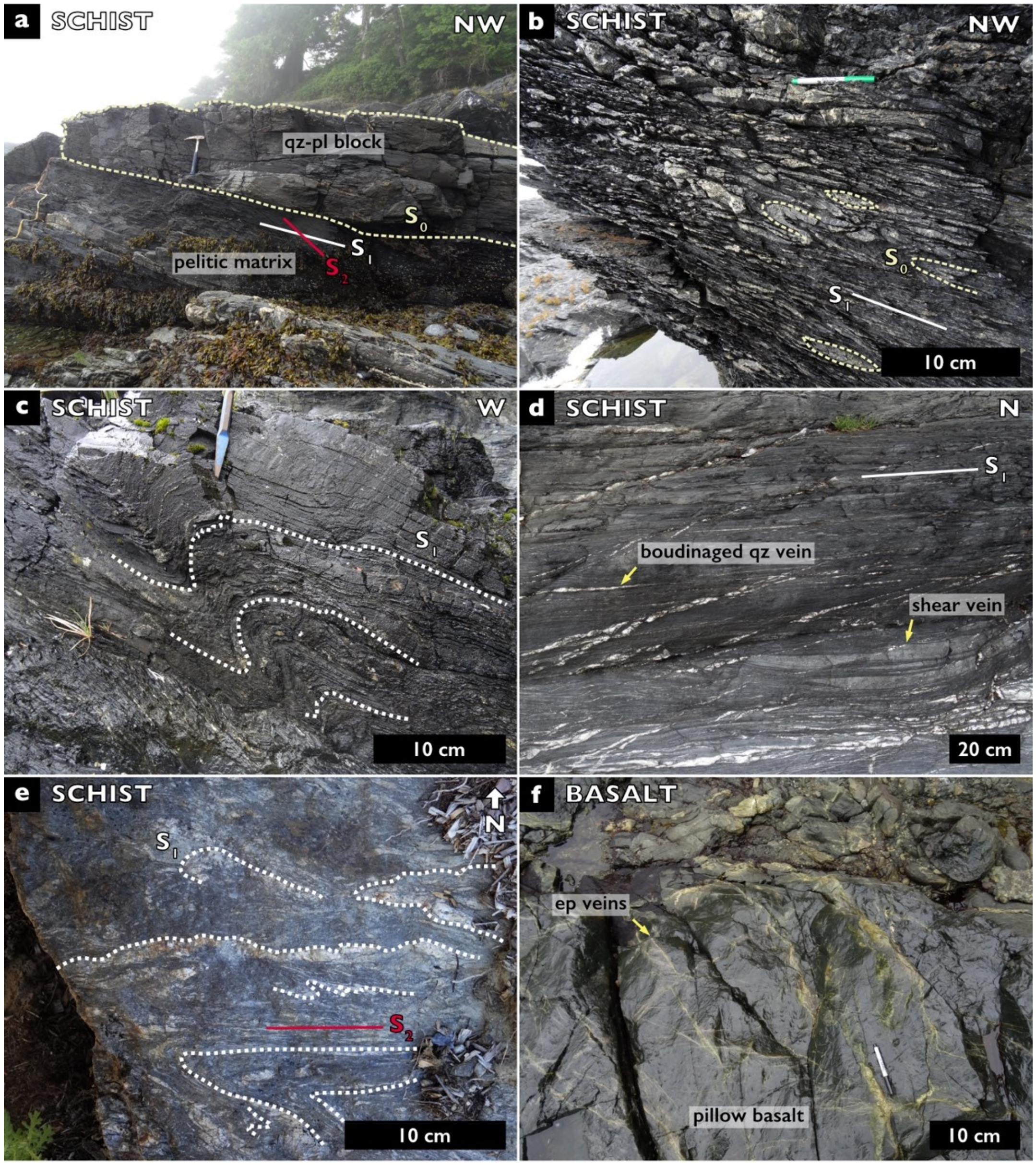

Figure 3-3: Field photos of structures in the hanging wall and footwall. a) Leech River Schist at Botany Bay contains centimeter- to meter-scale quartz-plagioclase blocks within a phyllosilicate-rich matrix, which defines a block-in-matrix texture and preserves original bedding (S_0) between sandstone layers and shale. The matrix has two foliation orientations (S_1 and S_2), with S_1 subparallel to the long axes of blocks. **b)** Isoclinal folding of the S_1 foliation with subparallel axial planes. **c)** Asymmetric, disharmonic folding of the S_1 foliation with axial planes subparallel to the S_2 foliation. **d)** Quartz veins within the LRS are oriented 0-30° from the S_1 foliation. Some shear veins host small amounts of displacement, while the veins

subparallel to foliation are offset along S_1. **e)** Leech River Schist directly north of the Diversion and Bear Creek reservoirs is composed of discontinuous quartz-plagioclase layers and micaceous layers. The S_1 foliation is transposed into parallel with the dominant S_2 foliation and tightly folded into disharmonic and often asymmetric folds. **f)** Metchosin Basalt at Sombrio Point contains pillow basalts with abundant epidote veins.

where S_0 is transposed (Fig. 3-3b). The S_2 foliation is axial planar to upright, tight to isoclinal, asymmetric, disharmonic folding of the S_1 foliation, which exhibits a top-to-the-south vergence direction (Fig. 3-3c). Later quartz veins crosscut both the blocks and matrix at a low angle to S_1 foliation and are moderately deformed into the S_1 foliation (Fig. 3-3d).

North of the Diversion and Bear Creek reservoirs, the schist no longer has a block-in-matrix structure, but instead it is characterized by disordered and discontinuous deformation fabrics (Fig. 3-3e). Dismembered S_0 compositional layering between metapsammitic and metapelitic layers (millimeters to 2-3 cm-thick) defines the dominant foliation, along with alignment of phyllosilicate minerals. This foliation is wavy and irregular, strikes roughly east-west, and dips steeply to the north (Fig. 3-2c). Asymmetric, tight folds of the layering with parasitic folding are common in both subhorizontal or subvertical sections with top-to-the-west and top-to-the-south vergence, respectively. Where observed, isoclinal folding is confined to individual quartz-plagioclase layers. Quartz veins crosscut the foliation at low and high angles and are often boudinaged and folded with the foliation. The similar attitudes of the dominant foliation in this region to the S2 foliation near Botany Bay, along with the similar vergence direction of asymmetric folds, suggests foliations formed under the same shortening direction. We interpret the dominant foliation as an S_2 foliation that has transposed and folded the S_1 foliation. Overall, the highly dismembered compositional layers, smaller scale of quartz-plagioclase boudins, and transposition of the S_1 foliation suggests that this region is relatively higher strain compared to the schist at Botany Bay.

3.4.2 Metchosin Basalt (footwall)

The Metchosin Basalt is a light to dark green very fine-grained to aphanitic massive amygdaloidal basalt composed of pyroxene or amphibole + plagioclase + epidote + titanite ± chlorite ± quartz. Near Sombrio Point, south of the shear zone, the basalt is massive with volcanic textures, including several meters-scale pillows which contain amygdules. Pillows and interstitial regions between them contain patches of epidote-rich rock as well as abundant epidote veins (Fig. 3-3f). There is no grain-scale or distributed foliation, so there is little evidence of pervasive deformation, but small faults with no preferred orientation are observed locally. The lack of consistent deformation fabrics in the basalt away from the LRSZ suggest that the basalt has experienced negligible distributed internal deformation.

3.4.3 Leech River Shear Zone

3.4.3.1 Structure and kinematics

The LRSZ is an approximately 600-meter wide mylonitic shear zone that deformed both the Leech River Schist and the Metchosin Basalt. We define the LRSZ as a high strain zone that contains distinct mylonitic fabrics and kinematic indicators compared to the surrounding rocks. In the schist, the shear zone is defined by a reduction in grain size, notably of porphyroblasts, planar and composite foliations, abundant deformed quartz veins, and isoclinal folds with subhorizontal and steeply plunging fold axes. In the metabasalt, planar foliation development and the presence of metamorphic amphibole define the shear zone. The edges of the LRSZ in both lithologies are

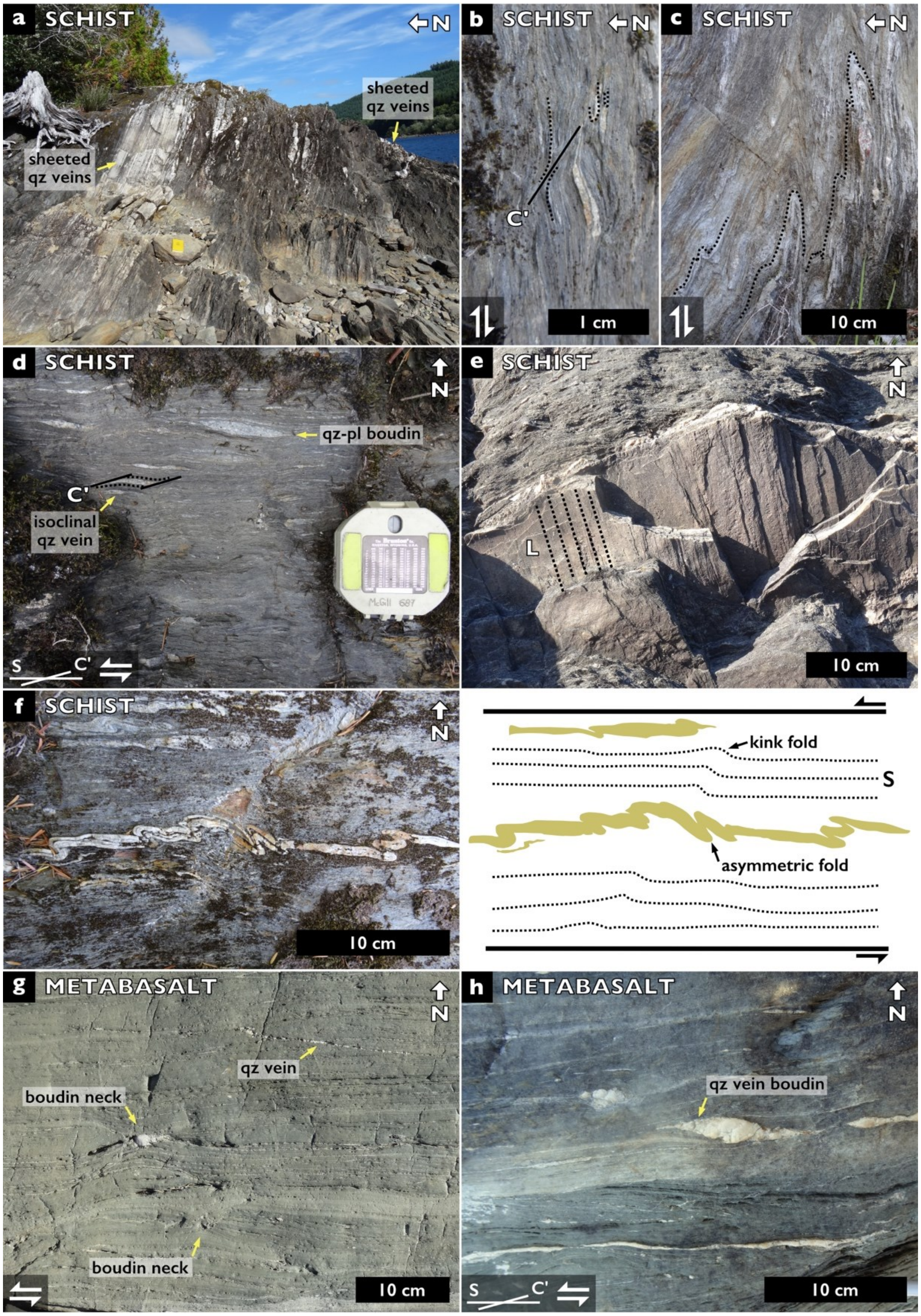

Figure 3-4: Field photos of structure and kinematics of the mylonite zone. Subvertical sections contain north-side-up shear sense indicators and subhorizontal sections contain left-

lateral shear sense indicators. **a-c)** Subvertical sections of the Leech River Schist mylonite showing foliation defined by compositional layering and alignment of phyllosilicate basal planes, C’ shear bands, isoclinal folding of quartz-dominated layers, and asymmetric folding of the foliation. **d)** Subhorizontal section of the LRS mylonite showing foliation, C’ shear bands, boudinage of quartz- and plagioclase-dominated layers, and isoclinal folding of quartz-dominated layers. **e)** Steeply plunging stretching lineation (L) visible on foliation planes within the LRS mylonite is defined by aligned mineral aggregates of phyllosilicates. **f)** Subhorizontal section of the LRS mylonite showing asymmetric shear folding of a quartz- and plagioclase-dominated layer and kink folding of foliation (S). The schematic cartoon illustrates the two types of folds. **g-h)** Subhorizontal sections of Metchosin Basalt mylonite showing foliation defined by compositional layering, C’ shear bands, and boudinage of compositional layering and quartz veins.

gradational. The broad-scale architecture of the shear zone, including potential lithologic mixing and deformation heterogeneity, is not well constrained due to limited exposure. A lithologic contact between the schist and metabasalt mylonites was only observed in one location, where the contact is sharp and planar over the extent of the outcrop, which is ~10 meters in length along strike.

The Leech River Schist mylonite is a strongly foliated and lineated, fine-grained rock (Fig. 3-4a-e). The mylonitic foliation is sub-parallel to the map-scale structure, striking approximately east-west and dipping steeply (~70°) to the north. This foliation is defined by subparallel compositional layers, development of a composite S-C-C’ foliation where the mylonite is phyllosilicate-rich, and a ubiquitous grain shape preferred orientation that is locally parallel to the compositional layers (Fig. 3-2b, 3-4a-d, and 3-5a,b). Elongate grains and aggregates of phyllosilicates aligned on foliation planes define a penetrative, steeply plunging stretching lineation (Fig. 3-2b and 3-4e). Compositional layers (millimeters to centimeters thick with rare layers of the order of tens of centimeters thick) are differentiated by changes in the relative proportion of phyllosilicates, quartz, and feldspar, equivalent to the layering between metapsammitic and metapelitic lithologies north of the shear zone. These layers are typically planar and continuous for tens of centimeters to meters, with lengths limited by exposure, such that the layering is extremely attenuated compared to outside the shear zone. Three types of folds affect the layering within the schist mylonite (Fig. 3-2b). The layers are isoclinally folded with axial planes parallel to the mylonitic foliation and both sub-horizontal and steeply plunging hinges (Fig. 3-4b-d). Tight folds of the layering are less common and have axial planes at a low angle to the foliation and steeply plunging axes subparallel to the stretching lineation (Fig 3-4f). Kink folds of the foliation are rare and have axial planes at a high angle to the foliation (Fig 3-4f). Most folds have the same sense of asymmetry with the exception of the kink folds, which are interpreted to have formed late relative to the other structures within the mylonites. Quartz-plagioclase-rich layers are also boudinaged with long axes of boudins parallel to the foliation. Shear bands that deflect the layering, boudin margins, and quartz veins define the C-C' composite foliation. We interpret the mylonitic foliation (S_3) to be axial planar to isoclinal folds of S_{0-2}, which are now all parallel due to transposition.

The Metchosin metabasalt mylonite contains a strong foliation defined by millimeter- to centimeter-scale compositional layering between plagioclase- and amphibole-rich layers (Fig. 3-2b and Fig. 3-4g,h). Some compositional layers are boudinaged with boudin long axes parallel to the layering. At the grain-scale, large (~200-500 μm) asymmetric amphibole porphyroblasts are surrounded by a fine-grained amphibole, plagioclase, and sometimes epidote matrix (Fig. 3-6a). Amphibole, plagioclase ribbons, and subparallel trains of titanite and ilmenite grains all show shape-preferred orientations parallel to the compositional layering (Fig. 3-6a). Subparallel long

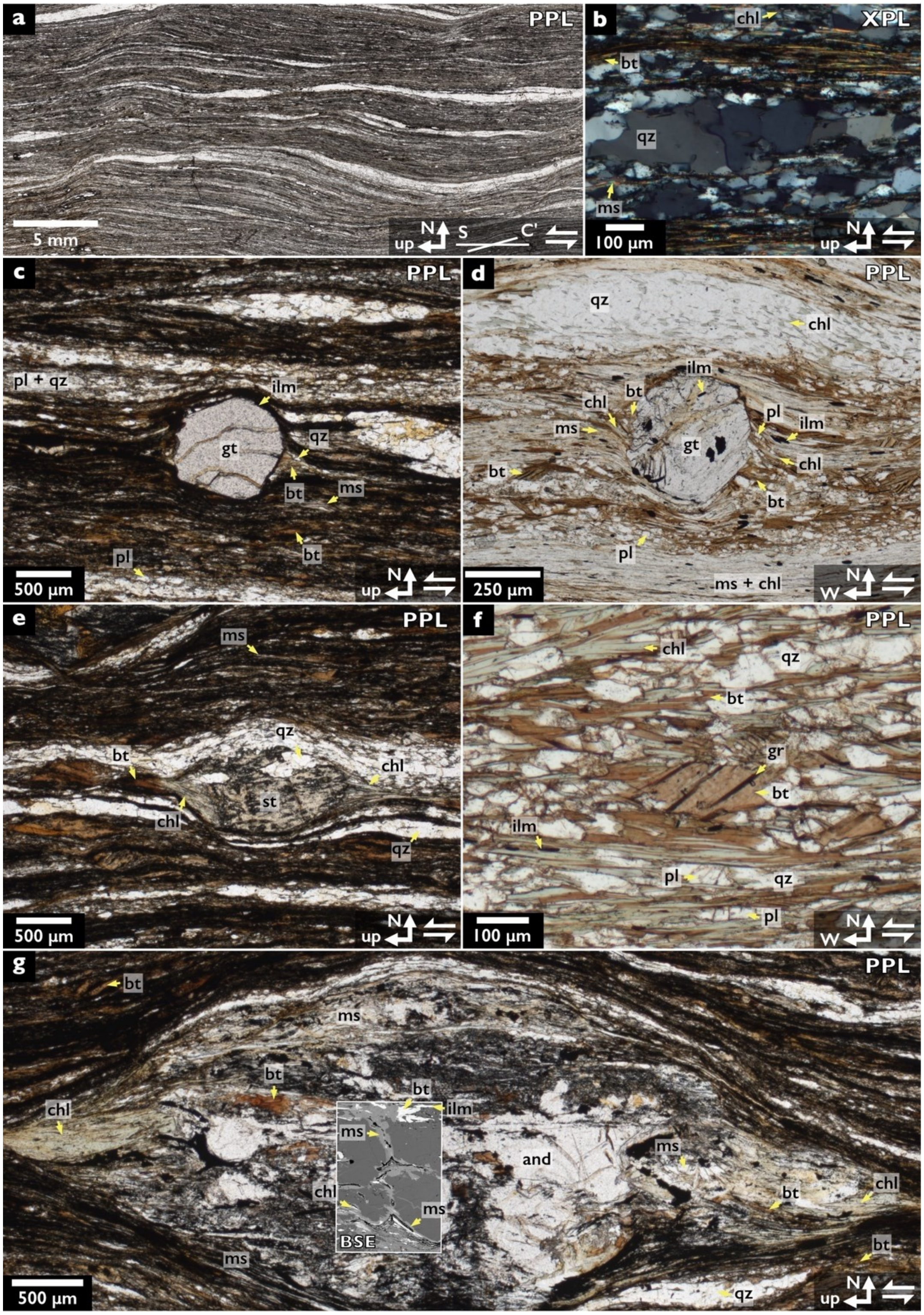

Figure 3-5: Leech River Schist mylonite microstructure. Photomicrographs in plane-polarized (PPL) and cross-polarized (XPL) light. **a)** Foliation planes (S) defined by

compositional layering deflected by C' shear bands creating an asymmetric composite foliation. **b)** Quartz-dominated layer with interpenetrative quartz grain boundaries. **c)** Garnet sigma-clast with asymmetric tails in lineation-parallel section. **d)** Garnet delta-clast with asymmetric tails in lineation-perpendicular section. **e)** Staurolite sigma-clast partially replaced by chlorite with asymmetric tails**. f)** Biotite porphyroblast with graphite inclusions and intergrown biotite and chlorite in a phyllosilicate-dominated layer. **g)** Andalusite sigma-clast partially replaced by muscovite with asymmetric tails. and—andalusite, bt—biotite, chl—chlorite, gr—graphite, gt—garnet, ilm—ilmenite, ms—muscovite, pl—plagioclase, qz—quartz, st—staurolite.

axes of amphibole minerals define a steeply plunging, penetrative mineral lineation in the metabasalt mylonite (Fig 3-2b).

Quartz veins are centimeters to tens of meters long and are present in both the schist and metabasalt mylonites, but they are far more abundant in the schist mylonite. The range of vein shapes and attitudes indicates they were progressively deformed during shear. Most quartz veins are boudinaged into asymmetrical shapes or isoclinally folded with their axial planes subparallel to the foliation (Fig. 3-2b and 3-4). A few veins exhibit folded axial surfaces, indicating they were re-folded. Later veins are relatively continuous and are oriented subparallel to the foliation. The latest veins are planar and crosscut the foliation at apparent angles of ~30° in subhorizontal exposures. Large sets of sheeted veins are tens of centimeters to around one meter thick and can be traced for hundreds of meters along strike (e.g., Fig. 3-4a). These sheeted veins are present in both the schist and metabasalt mylonites and contain multiple approximately centimeter-thick layers separated by sub-millimeter layers of phyllosilicates or amphibole, respectively, interpreted to be selvages of the local wall rock They are also isoclinally folded with steeply dipping axial surfaces subparallel to the mylonitic foliation and are occasionally boudinaged.

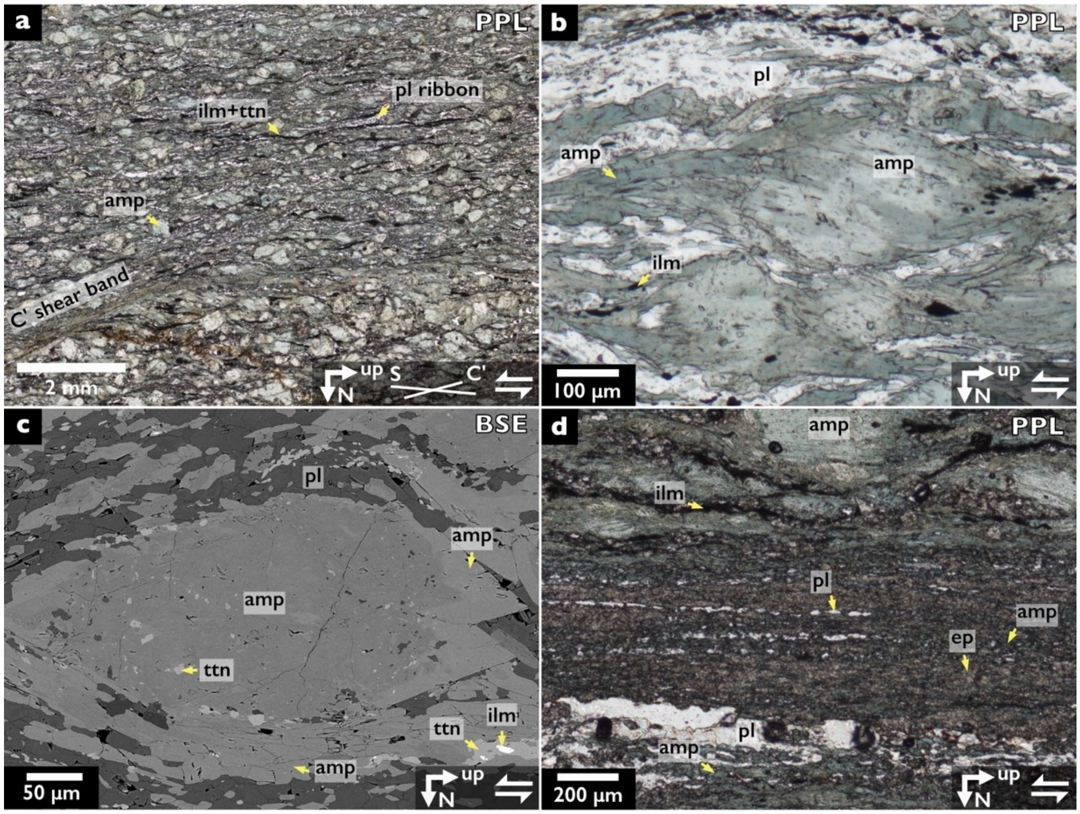

Figure 3-6: Metchosin Basalt mylonite microstructure. Photomicrographs in plane-polarized (PPL) and cross-polarized (XPL) light. **a)** Foliation planes (S) deflected by both C planes, oriented horizontally, and C' shear bands creating an asymmetric composite foliation. **b-c)** Chemical zoning between light green and dark green amphibole cores and tails. Fine-grained plagioclase surrounding amphibole porphyroblasts. Ilmenite seams along edges of amphibole domains. **d)** Fine-grained epidote-amphibole layer. amp—amphibole, ep—epidote, ilm—ilmenite, pl—plagioclase, ttn—titanite.

Kinematic indicators observed in outcrop (Fig. 3-4) and in thin section (Fig. 3-5 and 3-6) are consistent with sinistral-reverse motion in both the schist and metabasalt mylonites, with reverse-sense indicators most strongly expressed. Indicators include the development of a composite S-C foliation, deflection of the foliation by C' shear bands, asymmetric folding of the mylonitic foliation, asymmetric folding and boudinage of quartz veins, and asymmetric tails on rotated porphyroblasts. Overall, the dominant thrust motion and secondary sinistral strike-slip motion we observed is consistent with sinistral-oblique underthrusting of the Metchosin Basalt beneath the Leech River Schist.

3.4.3.2 Pressure and temperature of deformation

The pressure and temperature conditions of deformation inform the tectonic context and further dictate whether or not the LRSZ represents a subduction interface. Syn-kinematic P-T conditions were determined with a combination of microstructural observations and mineral chemistry analyses. For the schist mylonites, we applied syn-kinematic mineral assemblages, garnet compositional zoning, pseudosection modeling, and Ti-in-biotite geothermometry to constrain pressure and temperature. For the metabasalt mylonites, we used amphibole compositions to estimate metamorphic facies.

The schist mylonites in the LRSZ contain garnet + biotite + chlorite + muscovite + plagioclase + quartz + ilmenite ± staurolite ± andalusite ± graphite (Fig. 3-5). Compositional layering between millimeter- to centimeter-thick quartz-plagioclase-rich, and phyllosilicate-rich layers dominates the microstructure with porphyroblasts of garnet, staurolite, and andalusite. Garnet occurs within layers dominated by biotite, chlorite, and muscovite. Garnet porphyroblasts are euhedral, display minimal zoning, lack evidence of retrogression, and often have weakly asymmetric tails and pressure shadows of quartz and phyllosilicates in both lineation-parallel and lineation-perpendicular orientation (Fig. 3-5c,d). Some garnet grains are inclusion-free, while others have ilmenite and/or quartz inclusions. Ilmenite grains are also dispersed within mica-dominated layers in the matrix and are aligned with their long axis parallel to foliation. Staurolite porphyroblasts are partially replaced by chlorite and quartz and have weakly asymmetric tails (Fig. 3-5e). Fine-

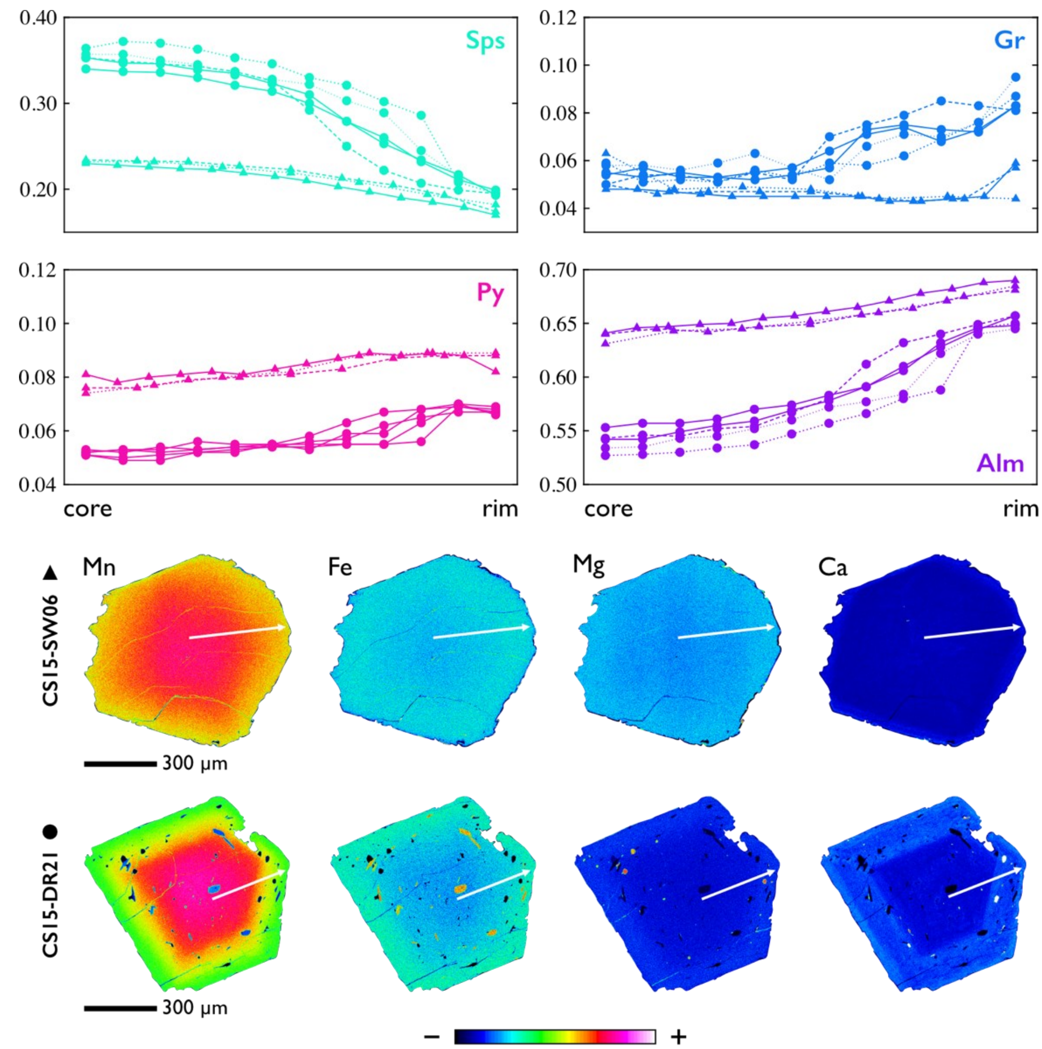

Figure 3-7: Garnet compositions from the schist mylonite. TOP: Garnet end-member fractions along core-to-rim transects showing decreasing Mn content and increasing Mg, Fe, and Ca content during growth. **BOTTOM:** Wavelength-dispersive X-ray spectroscopy (WDS) maps representative of garnet compositional zoning. Core and rim compositions from grains in sample CS15-SW06 are contoured on the pseudosection in Fig. 3-8. White arrows indicate location of microprobe transect. Sps—spessartine (X_{Mn}); Py—pyrope (X_{Mg}); Alm—almandine (X_{Fe}); Gr—grossular (X_{Ca}).

grained biotite, chlorite, and muscovite are intergrown in phyllosilicate-rich layers with basal planes locally parallel to the foliation. These phyllosilicate-rich layers have variable proportions of each phase, and muscovite-chlorite layers are most common. Biotite porphyroblasts with their

Table 3-1: Bulk composition of Leech River Schist obtained from XRF analyses

Oxide	Detection Limit	CS15-SW06 (wt%)
SiO_2	0.01	61.73
TiO_2	0.01	0.89
Al_2O_3	0.01	19.50
Fe_2O_3	0.01	7.49
MnO	0.001	0.116
MgO	0.01	2.52
CaO	0.01	1.22
Na_2O	0.01	1.45
K_2O	0.01	2.12
P_2O_5	0.01	0.17
Total	0.01	100.20
LOI	-	2.91
Co_3O_4	0.005	< 0.005
Cr_2O_3	0.01	0.02
CuO	0.005	0.012
NiO	0.003	0.005
V_2O_5	0.003	0.021
Graphite	0.05	0.70

basal plane at an angle to the foliation are coarse-grained (~100-1000s μm long), blocky, and often contain graphite interlayers (Fig. 3-5f). Large andalusite porphyroblasts (~1-10 mm long) are fragmented, surrounded by reaction rims composed of muscovite and biotite, and have weakly asymmetric tails composed of chlorite, biotite, and muscovite (Fig. 3-5g). The reaction rims indicate disequilibrium between the andalusite and staurolite porphyroblasts and matrix phases. The mineral textures described above therefore define a peak metamorphic mineral assemblage of garnet + biotite + chlorite + muscovite + quartz, with ilmenite (as it forms inclusions), staurolite, and andalusite growing prior to peak metamorphism. This peak assemblage is syn-kinematic with shear zone deformation based on the asymmetric tails formed on porphyroblasts and the layers of aligned micas defining the foliation.

Garnet compositions were analyzed to help constrain P-T estimates because compositional zoning within garnet records changing metamorphic conditions during growth. Transects across garnet grains show decreasing Mn content and increasing Mg, Fe, and Ca content, recording prograde growth at peak metamorphic conditions (Fig. 3-7; transect locations shown in Fig. B-2; Table B-1). Garnet compositions within each sample are internally consistent, with differences between samples attributable to compositional variation within the schist. This interpretation is supported by the differences in rim compositions between samples. Growth zones are visible in some grains (e.g., garnet from sample CS15-DR21 in Fig. 3-7), but most grains show continuous zonation, and the analyzed grains show minimal evidence of resorption rims or retrogression.

P-T conditions during peak metamorphism of schist mylonite were then estimated by calculating a pseudosection and overlapping the garnet compositions for a representative sample containing the peak metamorphic mineral assemblage defined above (CS15-SW06; Table 3-1). The pseudosection was calculated for the MnO-Na_2O-CaO-K_2O-FeO-MgO-Al_2O_3-SiO_2-TiO_2-H_2O system with H_2O as a saturated phase using the solution models listed in Fig. 3-8. Contours of garnet composition (i.e., isopleths) were calculated for endmember fractions (Mn, Ca, Fe) and representative core and rim isopleths were plotted. These garnet compositions plot within the gt-bt-chl-mica-ru-qz field, which is consistent with the peak metamorphic mineral assemblage (Fig. 3-8). Overlapping grossular (Ca), spessartine (Mn), and almandine (Fe) isopleths constrain the

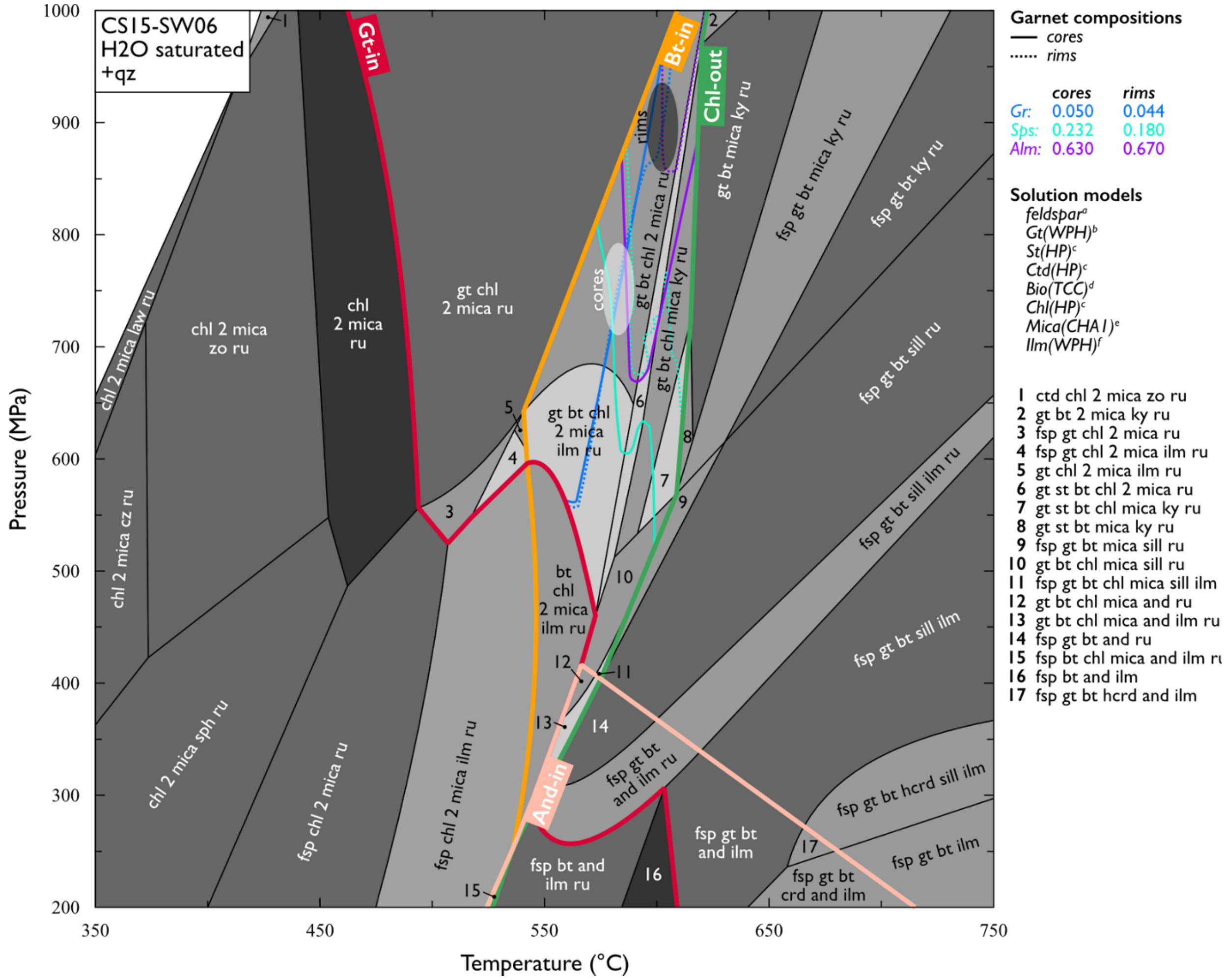

Figure 3-8: Pseudosection for schist mylonite. Pseudosection generated for schist mylonite sample CS15-SW06. Contours of grossular (Gr), spessartine (Sps), and almandine (Alm) content for garnet core and rim compositions crossover within the gt-bt-chl-2 mica-ru field at *T*~575 °C and *P*~750 MPa and *T*~600°C and *P*~850 MPa, respectively. Solution models are from [a]Fuhrman and Lindsley (1988), [b]White et al. (2007), [c]Holland and Powell (1998), [d]Tajčmanová et al. (2009), [e]Auzanneau et al. (2010), and [f]White et al. (2000). and—andalusite, bt—biotite, chl—chlorite, crd—cordierite, cz—clinozoisite, fsp—feldspar, gt—garnet, hcrd—hydrouscordierite, ilm—ilmenite, ky—kyanite, law—lawsonite, qz—quartz, ru—rutile, sill—sillimanite, st—staurolite, zo—zoisite.

metamorphic conditions of garnet growth from ~575 °C and ~750 MPa in the core to ~600 °C and ~850 MPa in the rim, although we note that the steep garnet contours make the pressure estimates sensitive to small changes in temperature.

Peak temperature estimates were also calculated from the Ti content of biotite following the method of Henry et al. (2005). Biotite grains selected for geothermometry were inclusion-free, showed no retrogression textures, and were not in contact with garnet. The Ti contents suggest peak metamorphic temperatures were primarily between 550-600 °C with an error of ±24 °C (Fig. 3-9; Table B-2). This temperature estimate is consistent across the four samples from the LRS mylonite and matches the temperature range predicted by the pseudosection.

The metabasalt mylonites contain a syn-kinematic mineral assemblage of amphibole + plagioclase + epidote + titanite ± chlorite ± quartz. Large amphibole porphyroblasts have chemically distinct cores and tails (Fig. 3-6b) and sometimes contain inclusions of titanite and plagioclase (Fig. 3-6c). Fine-grained amphibole, plagioclase, epidote, titanite, and ilmenite surround the amphibole porphyroblasts. Titanite and ilmenite occur as discontinuous seams often wrapping around amphibole grains with titanite sometimes enveloping large ilmenite grains. Quartz and chlorite occur as minor phases, with quartz present as fine grains within the matrix and rare chlorite present along amphibole tails. Fine-grained layers of epidote and amphibole with interspersed ribbons of plagioclase may represent relict epidote veins (Fig. 3-6d).

P-T conditions during metamorphism of the metabasalt mylonite were constrained with amphibole and plagioclase compositions (Fig. 3-10; Table B-3 and B-4). Spot analyses and maps document

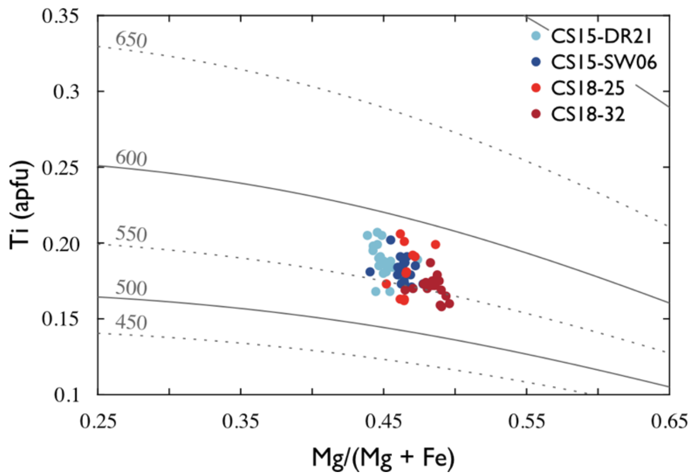

Figure 3-9: Ti-in-biotite thermometry. Ti content in biotite from the schist mylonite plotted on the Ti saturation surfaces of Henry et al. (2005). All analyses fall between the 500 and 600 °C contours, consistent with the peak metamorphic temperatures indicated by pseudosection modeling of ~550-575 °C.

increasing Fe, Al, Ti, and Na content and decreasing Mg and Si content from amphibole cores to rims/tails (Fig. 3-10a,c). The Si, Al, and Na distribution in amphibole structural sites depends on the pressure and temperature during growth (Ernst and Liu, 1998; Spear, 1981, 1995). Amphibole transitions from actinolite cores to hornblende/tschermakite rims via the pressure-sensitive Al-Tschermak substitution ($^{T}Si + {}^{M1\text{-}M3}Mg = {}^{T}Al + {}^{M1\text{-}M3}Al$). The positive correlation between A site occupancy and tetrahedrally-coordinated Al (Al^{iv}) records the temperature-sensitive edenite exchange ($^{T}Si + {}^{A}[\ ] = {}^{T}Al + {}^{A}(Na + K)$). Growth of magnesio-hornblende amphibole rims suggests peak metamorphic temperatures were >420 °C, providing a minimum constraint (Maruyama et al., 1983). Additionally, TiO_2 in amphibole increases from 0.05-0.15 in the cores to 0.20-0.50 in the rims. The increasing TiO_2 content is consistent with increasing temperature (Ernst and Liu, 1998). These trends record prograde amphibole growth during deformation. Metamorphic plagioclase compositions are oligoclase to andesine ($An_{26\text{-}45}$; Fig. 3-10b), which are typical of amphibolite facies metamorphism and the calcification of plagioclase, caused by increasing temperature, is

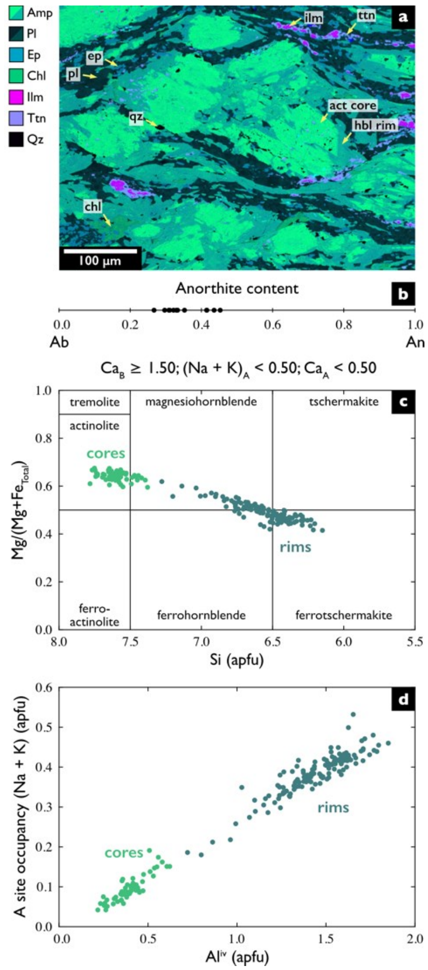

Figure 3-10: Amphibole and plagioclase compositions from the metabasalt mylonite. Chemical maps and point analyses from plagioclase grains and amphibole grains with chemically distinct cores and rims. **a)** False-colored phase map generated from multiple x-ray maps highlighting chemically distinct cores and rims. Rim compositions extend into syn-kinematic tails. **b)** Plagioclase compositions in the matrix range from An_{27} to An_{45}. **c)** Amphibole core and rim compositions plotted onto a discrimination diagram with field labels following Leake et al. (1997). Cores primarily plot as actinolite, while rims plot as hornblende to tschermakite. **d)** Temperature-sensitive A site occupancy and tetrahedral alumina content demonstrate prograde growth of amphibole.

consistent with the actinolite-to-hornblende transition (Maruyama et al., 1982; Maruyama et al., 1983; Spear, 1995).

3.5 Detrital zircon U-Pb geochronology

We investigated the origin of the protolith and intrusives of the Leech River Complex with detrital zircon geochronology to re-evaluate the deposition age of the complex and help determine if the Jordan River Unit is metasedimentary or intrusive. U-Pb ages were analyzed from zircon grains in four rock samples: one sample of Walker Creek intrusives, one sample of Leech River Schist, and two samples of the Jordan River Unit, which has been inconsistently described as a metasandstone (Fairchild and Cowan, 1982; Muller, 1980) and an igneous intrusion (Groome et al., 2003) (sample locations in Fig. 3-1).

The MDA of the Leech River Schist sample is 64.4±2.4 (2σ) Ma and the MDA of the Jordan River samples are 66.9±2.1 Ma and 61.0±2.1 Ma (2σ). U-Pb age distributions are presented as histograms and kernal density estimate (KDE) diagrams (Fig. 3-11; Table B-5). Zircons in the Leech River Schist and Jordan River metasandstone are detrital, with two significant peaks at 60-100 Ma and 140-200 Ma and a cluster of minor peaks between 1100-1800 Ma. Mesozoic zircons were likely sourced from the nearby Coast Mountains Batholith, the volcanic arc formed from Jurassic-Cretaceous subduction beneath the western margin of Wrangellia (Cecil et al., 2018; Friedman and Armstrong, 1995; Gehrels et al., 2009). Precambrian zircons have several possible sources, which are discussed below in section 3.5.1. The similar U-Pb age distribution and MDAs for the Leech River Schist and Jordan River Unit, together with petrographic observations (Fig. B-3), support the interpretation that the Jordan River Unit is metasedimentary (as defined by Fairchild and Cowan (1982) and Muller (1980)). The Walker Creek intrusion contains very few zircons and the age distribution matches distributions from the Leech River Schist and Jordan River metasandstone, suggesting these zircons were all inherited during *in situ* partial melting of the

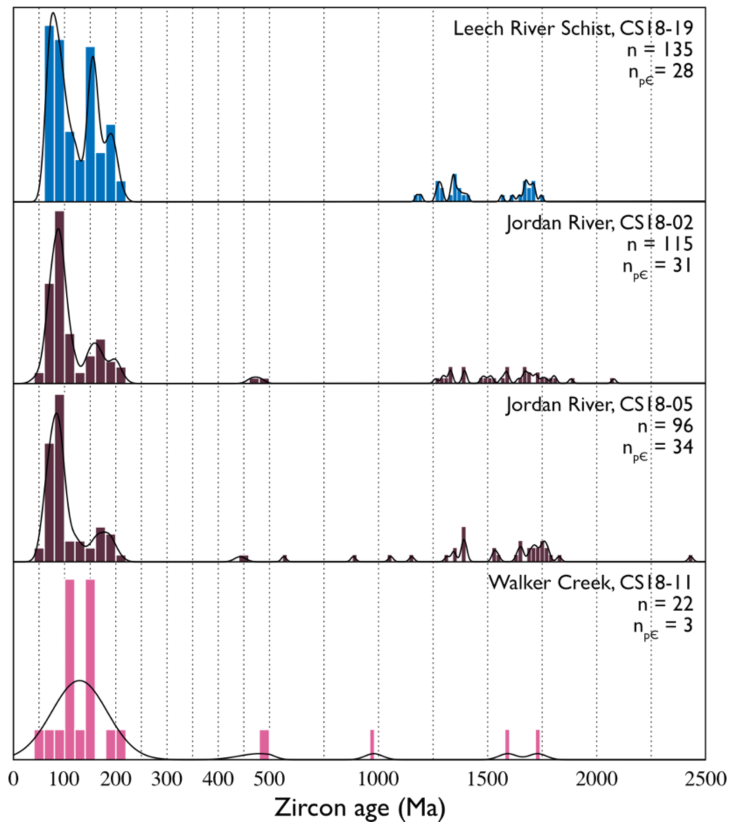

Figure 3-11: U-Pb detrital zircon geochronology of the Leech River Complex. Histograms and kernel density estimates for detrital zircons from the Leech River Schist (CS1819, blue), Jordan River metasandstone (CS1802 and CS1805, purple), and the Walker Creek intrusions (CS1811, pink). Note that there's a break in scaling on the x-axis at 500 Ma, but the bin size is consistently 20 My.

schist, consistent with the peraluminous compositions of the intrusions. The youngest age in the Walker Creek is 47.5±1.6 Ma (2σ), possibly representing a crystallization age, but not conclusively.

3.6 Discussion

3.6.1 Origin of the Leech River Complex and coast-wise transport

Our field observations of lithological variation between metapelitic and metapsammitic layers are consistent with previous work, which suggested the Leech River Schist formed as a series of turbidites and minor volcanics deposited near a continental margin (Fairchild and Cowan, 1982; Rusmore and Cowan, 1985). Late Cretaceous to Paleocene depositional ages of the Leech River Schist and Jordan River Unit are younger than previous Late Jurassic to Cretaceous deposition estimates based on whole-rock Rb-Sr isotopic data (Fairchild and Cowan, 1982).

The general lithology, approximate age, and depositional setting are common to many geologic units spread over thousands of kilometers of coastal North America, whose paleogeography and depositional relationships have been the focus of decades of tectonic reconstructions (e.g., Cowan, 2003; Cowan et al., 1997; Garver and Davidson, 2015; Zumsteg et al., 2003). The detrital zircon age distributions of the Leech River Schist and Jordan River metasandstone are similar to two separate groups of potentially related sedimentary rocks: the Maastrichtian-age formations in the Upper Nanaimo Group on Vancouver Island (Coutts et al., 2020; Englert et al., 2018; Matthews et al., 2017) and the Yakutat Group in Alaska (Fig. 3-12; Garver and Davidson, 2015). The Upper Nanaimo Group were deposited in a marine subduction forearc basin. The Yakutat Group, part of the Chugach-Prince William Terrane, was deposited as trench-fill turbidites. Previous authors concluded that Mesozoic and early Paleocene age grains (200-60 Ma) are likely derived from the Coast Mountains Batholith, while Proterozoic (1850-1560 and 1450-1300 Ma) zircons have been proposed to either derive from the Belt-Purcell Basin in Idaho or the Yavapai and Mazatzal terranes of southwestern Laurentia (Coutts et al., 2020; Dumitru et al., 2016; Garver and Davidson, 2015; Housen and Beck, 1999; Matthews et al., 2017). Matthews et al. (2017) prefer the interpretation that the Nanaimo Group Proterozoic zircon population was derived from southwestern Laurentia and argue in favor of the Nanaimo Group undergoing large amounts of displacement in the Late Cretaceous or Cenozoic. Garver and Davidson (2015) also interpret the Proterozoic ages as derived from a Yavapai and Mazatzal source, which is further supported by juvenile Hf isotopic compositions.

Large coast-wise translation is required to reconcile the deposition of southwest Laurentian zircons with the current positions of all three units. The similarity between the Leech River Schist, Upper Nanaimo Group, and Yakutat Group zircon populations and their potential sources suggests that these units were likely deposited near each other in the Late Cretaceous to Paleocene. This proximity is reinforced by the narrow geographic window allowing for sediment from southwestern Laurentia to reach the near-margin basins where the units were accumulating (Jacobson et al., 2011). Additionally, the Nanaimo Group uncomfortably overlies the Wrangellia Terrane (Mustard, 1994), requiring Wrangellia to be located further south during deposition as well. We infer that the Leech River Schist must have been deposited near its current geographic position relative to the Wrangellia Terrane, which constitutes the majority of Vancouver Island. It follows that the Leech River, Nanaimo Group, and Wrangellia have been proximal since the Late Cretaceous and any subsequent coast-wise motion translated them together as one block. Together with the Yakutat Group, these units were all part of the coherent "Baja-BC" block that experienced northward translation during the Late Cretaceous to early Cenozoic (Cowan, 1982, 2003; Garver and Davidson, 2015). Forearc anatexis of the Leech River Schist due to heating by the slab window produced the Walker Creek intrusions that pin the location of the schist to its current position from

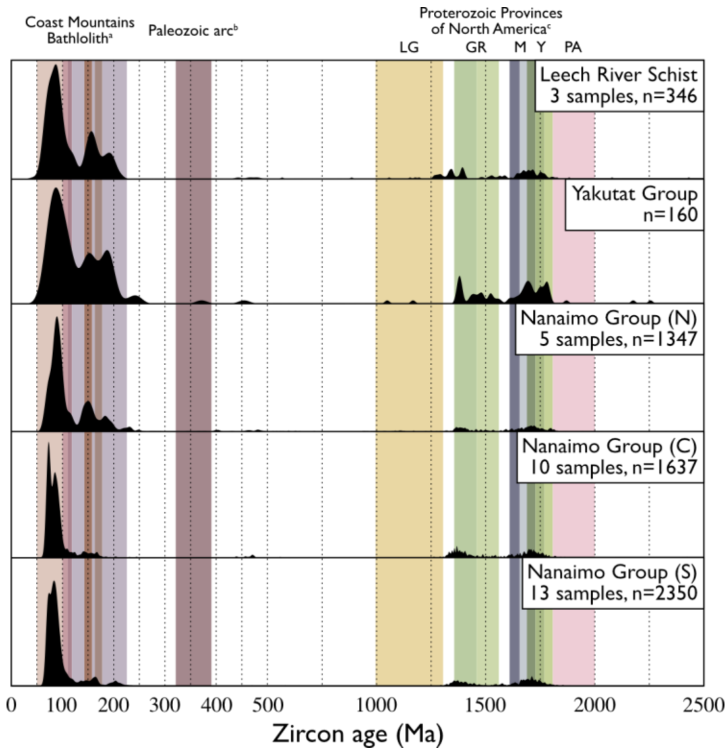

Figure 3-12: Comparing detrital zircon ages across terranes. Detrital zircon age distributions (KDEs) from the Leech River Schist compared with the Yakutat Group (Garver and Davidson, 2015) and "Facies 2" zircons from the Upper Nanaimo Group (northern, central, and southern transects of Coutts et al., 2020; Englert et al., 2018; Matthews et al., 2017). Colored bars represent detrital zircon provenances from [a]Gehrels et al. (2009), [b]Nelson and Colpron (2007), and [c]Whitmeyer and Karlstrom (2007). LG—Llano-Grenville province. GR—Granite-Rhyolite province. M—Mazatzal province. Y—Yavapai province. PA—Paleoproterozoic arcs.

~51 Ma to the present (Breitsprecher et al., 2003; Groome et al., 2003). These ages therefore constrain the coast-wise translation to have occurred between ~61 Ma and ~51 Ma. Subsequently, the Yakutat Group and the rest of the Chugach-Prince William Terrane were translated further north beyond Vancouver Island to their current position in the Cenozoic.

3.6.2 Deformation in the Leech River Shear Zone

Field and microstructural observations of distinct deformation characteristics within the schist and metabasalt mylonites define the LRSZ. Relative to the structures formed in the schist north of the LRSZ, the schist mylonite contains a more strongly developed foliation defined by thin compositional layers and pronounced grain shape-preferred orientations, a steeply plunging stretching lineation oriented downdip, and steeply plunging folds hinges for folds formed during shear zone deformation. We interpret the thinner, more repetitive banding in the schist mylonite to be the result of higher shear strains accumulated during further isoclinal folding, layer thinning, and transposition relative to the folding and disruption of bedding observed in the schist north of the LRSZ. The compositional layering in the schist mylonites is therefore likely the rotated, thinned, and transposed equivalents of the sedimentary bedding observed at Botany Bay. A distinct metamorphic mineral assemblage and a strongly developed foliation define the metabasalt mylonite, which exhibits similar kinematics to the schist mylonite. The consistent structures and kinematics between the schist and metabasalt mylonites clearly define the deformation that is characteristic of the shear zone relative to regional deformation in the Leech River Schist.

The S_2 foliation in the Leech River Schist north of the mylonite zone is parallel to the mylonitic (S_3) foliation, indicating that the shortening throughout the schist may have been coeval with displacement across the shear zone, rather than representing a distinct earlier phase of deformation. These interpretations are broadly consistent with the observations of Fairchild and Cowan (1982) and Groome et al. (2003), but our results are the first to show reverse-sense motion across the LRSZ. We observed isoclinal folding of previously transposed layering (e.g., Fig. 3-3e), suggesting that the foliations shown in Fig. 3-2, with the exception of S_1 at Botany Bay, match those of Fairchild and Cowan (1982) and correspond to their D_2. At Botany Bay, the S_2 foliation is less pronounced than in other exposures of the schist. Though qualitative, this observation suggests strain may decrease through the unit to the north (as previously suggested by Fairchild and Cowan (1982) and Rusmore and Cowan (1985)). Due to limited exposures, we do not have data to determine if the strain gradient is continuous or discontinuous (e.g., broken up by intra-complex faulting). The S_1 foliation at Botany Bay is more shallowly dipping, is oriented at a ~30° angle to the shear zone orientation, and may represent an earlier phase of deformation.

3.6.3 Paleo-subduction zone

Shear zone metamorphism, kinematics, and tectonic context all suggest that the LRSZ is a sinistral-oblique thrust that accommodated subduction of the Metchosin Basalt beneath the North American margin and therefore represents a paleo-subduction plate interface. Prograde growth of syn-kinematic metamorphic minerals such as garnet in the schist mylonite and amphibole in the metabasalt mylonite confirm that shear zone deformation fabrics formed during subduction.

P-T conditions during deformation in the LRSZ estimated from the schist and metabasalt mylonites are compatible. Chemical zoning in garnet qualitatively indicates prograde temperature and pressure changes during growth, which are further supported by thermodynamic calculations of isopleths. Contours of spessartine and almandine content predict moderate increases in temperature from core to rim, and contours of almandine and grossular content require a minimum of 550-650 MPa while crossover points predict peak pressures up to 850 MPa (Fig. 3-8). In amphibole, the transition from actinolite cores to hornblende rims indicates the transition between greenschist and amphibolite facies (Maruyama et al., 1983). This transition corresponds with increasing pressure and temperature recorded by the increasing Ti, Na, and Al content and decreasing Si (Fig. 3-10; Ernst and Liu, 1998; Spear, 1981, 1995). The amphibolite facies metamorphism predicted by the garnet and amphibole compositions are confirmed by peak temperature estimates of 550-575 °C from Ti-in-biotite geothermometry in the schist mylonite (Fig. 3-9).

Our observations of the metamorphic mineralogy of the Leech River Schist and Metchosin Basalt are consistent with previous studies (Fairchild and Cowan, 1982; Groome et al., 2003; Timpa et al., 2005). However, syn- to post-kinematic low-pressure metamorphism of the Leech River Schist was previously inferred based on the presence of andalusite (Fairchild and Cowan, 1982; Groome et al., 2003). Andalusite in the schist mylonite is rare, small (<1 cm), and exhibits disequilibrium textures and syn-kinematic tails within the phyllosilicate-rich matrix (e.g., Fig. 3-5g). We therefore interpret andalusite growth to pre-date peak, syn-kinematic metamorphism in the LRSZ.

Peak temperature and pressure conditions of 600 °C and 850 MPa during deformation are within the temperature range of the andalusite stability field (525-700 °C), but our pressure estimates that are significantly greater (<400 MPa). The structural context, which indicates thrust faulting across the LRSZ, indicates increasing pressure is likely due to subduction-related burial of the Leech River Complex, which is supported by the garnet and amphibole compositions. Our P-T estimates correspond to a geothermal gradient of ~20 °C/km, which is compatible with the hottest subduction zones (Penniston-Dorland et al., 2015; Syracuse et al., 2010). These anomalous elevated temperatures are likely due to the subduction of the Kula-Farallon Ridge beneath the forearc (Breitsprecher et al., 2003; Groome and Thorkelson, 2009). Geothermal gradients during ridge subduction as high as 50 °C/km have been reported in other subduction complexes (e.g., Sakaguchi, 1996). Additionally, we interpret the spatial variation in metamorphic mineral assemblages to be controlled by compositional heterogeneity within the Leech River Schist rather than contact metamorphism.

We propose a new model for the tectonic evolution of the LRSZ as a paleo-subduction zone during the Eocene that accommodated docking of the Metchosin Basalt against the North American margin and subduction beneath the Leech River Schist (Fig. 3-13). At ~65 Ma, the Leech River Schist and Nanaimo Group were deposited in near-margin subduction forearc basins (MDA 66-61 Ma; this study). Coast-wise transport of all three units during the Late Cretaceous to early Paleogene prior to docking of the Metchosin Basalt is allowable according to our study and is postulated by previous studies (Coutts et al., 2020; Matthews et al., 2017). At ~52 Ma, the Metchosin Basalt formed as part of an oceanic plateau (U-Pb zircon age of 52±2 Ma; Massey (1986); Phillips et al. (2017)) while ongoing subduction of the Kula/Resurrection and Farallon plates deformed the underthrust Leech River Schist, while the Nanaimo Group was shallowly buried. By ~50-45 Ma, during the collision and accretion of the Siletz-Crescent Terrane to the North American margin, the Metchosin Basalt was subducted beneath the Leech River Schist along the LRSZ, the Cowichan fold-and-thrust belt developed in the Nanaimo Group (England and Calon, 1991), and shortening and rotation initiated in the forearc (Johnston and Acton, 2003). Shortly thereafter, the Metchosin Basalt, and therefore the LRSZ itself, were underplated and accreted to the overriding continent as the décollement stepped further west. Following underplating, the Leech River Schist was exhumed through the mica cooling temperatures ($^{40}Ar/^{39}Ar$ ages of 45.2±0.2 Ma and 42.5±0.2 Ma in muscovite and biotite, respectively; Groome

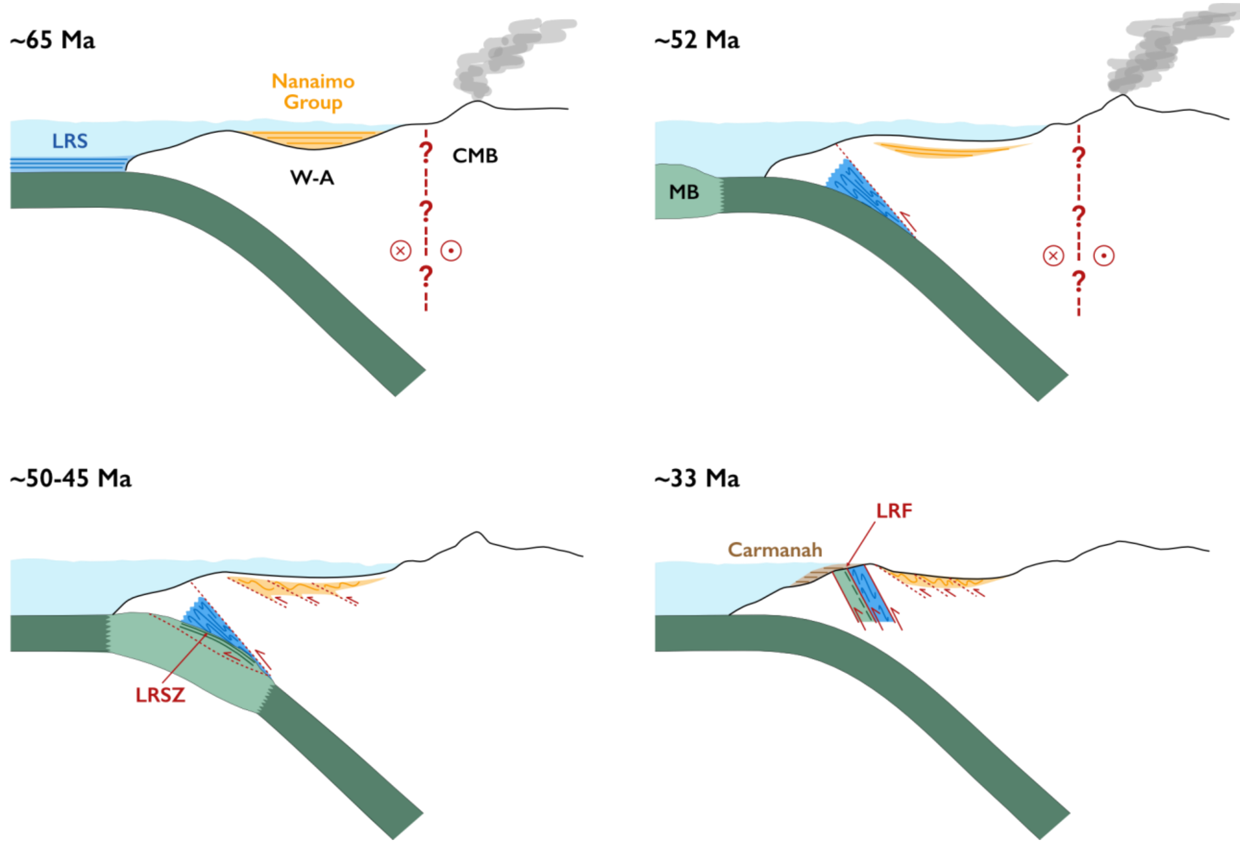

Figure 3-13: Tectonic history of the LRF. Schematic cartoon of the development of the Leech River Shear Zone and surrounding terranes from ~65 Ma to ~33 Ma. CMB—Coast Mountains Batholith. LRSZ—Leech River Shear Zone. LRS—Leech River Schist. MB—Metchosin Basalt. W-A—Wrangellia-Alexander Terrane.

et al. (2003)). Deposition of the unconformable coastal marine Carmanah Formation across the LRSZ in the Oligocene constrains the exhumation and exposure of the units at the surface (Muller, 1977a). This interpretation is consistent with previous work on the tectonic history and timing of accretion of the Siletz-Crescent Terrane (Eddy et al., 2016; Groome et al., 2003; McCrory and Wilson, 2013; Wells et al., 2014).

3.7 Conclusions

Structures, kinematics, and metamorphism of mylonites from the LRSZ indicate sinistral-reverse sense deformation under amphibolite facies conditions in both the schist and metabasalt. The elevated geotherm implied by the peak P-T conditions likely resulted from subduction of the Kula/Resurrection-Farallon Ridge and the nearby Yellowstone Hotpot. These observations are consistent with tectonic models of the hotspot location and plate motions during the Eocene (~50 Ma). Detrital zircon distributions suggest the Leech River Schist was deposited in proximity to the Upper Nanaimo Group on eastern Vancouver Island and the Yakutat Group in Alaska during the Cretaceous. Proterozoic zircon ages of all three units are characteristic of a southwest Laurentian source that requires coast-wise transport. The Leech River Schist, Nanaimo Group, and Wrangellia were likely translated north as a coherent block. We therefore establish that the Leech River Schist is not allochthonous to most of Vancouver Island, and the LRSZ represents a paleo-plate interface from an anomalously hot Eocene subduction zone.

3.8 References

Auzanneau, E., Schmidt, M.W., Vielzeuf, D., Connolly, J.A.D., 2010. Titanium in phengite: a geobarometer for high temperature eclogites. Contrib. Mineral. Petrol. 159, 1. https://doi.org/10.1007/s00410-009-0412-7.

Babcock, R.S., Burmester, R.F., Engebretson, D.C., Warnock, A., Clark, K.P., 1992. A rifted margin origin for the crescent basalts and related rocks in the northern Coast Range Volcanic Province, Washington and British Columbia. J. Geophys. Res. Solid Earth 97, 6799-6821. https://doi.org/10.1029/91JB02926.

Breitsprecher, K., Thorkelson, D.J., Groome, W.G., Dostal, J., 2003. Geochemical confirmation of the Kula-Farallon slab window beneath the Pacific Northwest in Eocene time. Geology 31, 351-354. https://doi.org/10.1130/0091-7613(2003)031<0351:GCOTKF>2.0.CO;2.

Cecil, M.R., Rusmore, M.E., Gehrels, G., Woodsworth, G., Stowell, H.H., Yokelson, I.N., Chisom, C., Trautman, m., Homan, E., 2018. Along-strike variation in the magmatic tempo of the Coast Mountains Batholith, British Columbia, and implications for processes controlling episodicity in arcs. Geochem. Geophys. Geosyst. 19, 4274-4289. https://doi.org/10.1029/2018GC007874.

Clowes, R.M., Brandon, M.T., Green, A.G., Yorath, C.J., Brown, A.S., Kanasewich, E.R., Spencer, C., 1987. LITHOPROBE--southern Vancouver Island: Cenozoic subduction complex imaged by deep seismic reflections. Can. J. Earth Sci. 24, 31-51. https://doi.org/10.1139/e87-004.

Connolly, J.A.D., 2005. Computation of phase equilibria by linear programming: a tool for geodynamic modeling and its application to subduction zone decarbonation. Earth Planet. Sci. Lett. 236, 524-541. https://doi.org/10.1016/j.epsl.2005.04.033.

Coutts, D., Matthews, W.A., Englert, R.G., Brooks, M.D., Boivin, M.-P., Hubbard, S., 2020. Along-strike variations in sediment provenance within the Nanaimo basin reveal mechanisms of forearc basin sediment influx events. Lithosphere 12, 180-197. https://doi.org/10.1130/L1138.1.

Cowan, D.S., 1982. Geological evidence for post-40 m.y. B.P. large-scale northwestward displacement of part of southeastern Alaska. Geology 10, 309-313. https://doi.org/10.1130/0091-7613(1982)10<309:GEFPMB>2.0.CO;2.

Cowan, D.S., 2003. Revisiting the Baranof-Leech River hypothesis for early Tertiary coastwise transport of the Chugach-Prince William terrane. Earth Planet. Sci. Lett. 213, 463-475. https://doi.org/10.1016/S0012-821X(03)00300-5.

Cowan, D.S., Brandon, M.T., Garver, J.I., 1997. Geologic tests of hypotheses for large coastwise displacements—A critique illustrated by the Baja British Columbia controversy. Am. J. Sci. 297, 117-173.

Cui, Y., Miller, D., Schiarizza, P., Diakow, L.J., 2017. British Columbia digital geology. British Columbia Ministry of Energy, Mines and Petroleum Resources, British Columbia Geological Survey Open File 2017-8, Data version 2019-12-19.

Dumitru, T.A., Elder, W.P., Hourigan, J.K., Chapman, A.D., Graham, S.A., Wakabayashi, J., 2016. Four Cordilleran paleorivers that connected Sevier thrust zones in Idaho to depocenters in California, Washington, Wyoming, and, indirectly, Alaska. Geology 44, 75-78. https://doi.org/10.1130/G37286.1.

Duncan, R.A., 1982. A captured island chain in the Coast Range of Oregon and Washington. J. Geophys. Res. Solid Earth 87, 10827-10837. https://doi.org/10.1029/JB087iB13p10827.

Eddy, M.P., Bowring, S.A., Umhoefer, P.J., Miller, R.B., McLean, N.M., Donaghy, E.E., 2016. High-resolution temporal and stratigraphic record of Siletzia's accretion and triple junction migration from nonmarine sedimentary basins in central and western Washington. Geol. Soc. Am. Bull. 128, 425-441. https://doi.org/10.1130/B31335.1.

Eddy, M.P., Clark, K.P., Polenz, M., 2017. Age and volcanic stratigraphy of the Eocene Siletzia oceanic plateau in Washington and on Vancouver Island. Lithosphere 9, 652-664. https://doi.org/10.1130/L650.1.

England, T.D.J., Calon, T.J., 1991. The Cowichan fold and thrust system, Vancouver Island, southwestern British Columbia. Geol. Soc. Am. Bull. 103, 336-362. https://doi.org/10.1130/0016-7606(1991)103<0336:TCFATS>2.3.CO;2.

Englert, R.G., Hubbard, S., Coutts, D., Matthews, W.A., 2018. Tectonically controlled initiation of contemporaneous deep ‐ water channel systems along a Late Cretaceous continental margin, western British Columbia, Canada. Sedimentology 65, 2404-2438. https://doi.org/10.1111/sed.12472.

Ernst, W.G., Liu, J., 1998. Experimental phase-equilibrium study of Al- and Ti-contents of calcic amphibole in MORB—A semiquantitative thermobarometer. Am. Min 83, 952-969. https://doi.org/10.2138/am-1998-9-1004.

Fairchild, L.H., Cowan, D.S., 1982. Structure, petrology, and tectonic history of the Leech River complex northwest of Victoria, Vancouver Island. Can. J. Earth Sci. 19, 1817-1835. https://doi.org/10.1139/e82-161.

Fleming, S.W., Tréhu, A.M., 1999. Crustal structure beneath the central Oregon convergent margin from potential ‐ field modeling: Evidence for a buried basement ridge in local contact with a seaward dipping backstop. J. Geophys. Res. Solid Earth 104, 20431-20447. https://doi.org/10.1029/1999JB900159.

Friedman, R.M., Armstrong, R.L., 1995. Jurassic and Cretaceous geochronology of the southern Coast Belt, British Columbia, 49° to 51°N. Special Papers-Geological Society of America 299, 95-139. https://doi.org/10.1130/SPE299-p95.

Fuhrman, M.L., Lindsley, D.H., 1988. Ternary-feldspar modeling and thermometry. Am. Min 73, 201-215.

Garver, J.I., Davidson, C.M., 2015. Southwestern Laurentian zircons in Upper Cretaceous flysch of the Chugach-Prince William terrane in Alaska. Am. J. Sci. 315, 537-556.

Gehrels, G., Rusmore, M.E., Woodsworth, G., Crawford, M., Andronicos, C., Hollister, L., Patchett, J., Ducea, M., Butler, R., Klepeis, K., Davidson, C.M., Friedman, R., Haggart, J., Mahoney, B., Crawford, W., Pearson, D., Girardi, J., 2009. U-Th-Pb geochronology of the Coast Mountains batholith in north-coastal British Columbia: Constraints on age and tectonic evolution. Geol. Soc. Am. Bull. 121, 1341-1361. https://doi.org/10.1130/B26404.1.

Groome, W.G., 2000. Magmatism and Metamorphism in the Leech River Complex, Southern Vancouver Island, British Columbia, Canada: Implications for Eocene Tectonics of the Pacific Northwest. Simon Fraser University.

Groome, W.G., Thorkelson, D.J., 2009. The three-dimensional thermo-mechanical signature of ridge subduction and slab window migration. Tectonophysics 464, 70-83. https://doi.org/10.1016/j.tecto.2008.07.003.

Groome, W.G., Thorkelson, D.J., Friedman, R.M., Mortensen, J.K., Massey, N.W.D., Marshall, D.D., Layer, P.W., 2003. Magmatic and tectonic history of the Leech River Complex, Vancouver Island, British Columbia: Evidence for ridge-trench intersection and accretion of the Crescent Terrane. Special Papers-Geological Society of America 371, 327-353. https://doi.org/10.1130/0-8137-2371-X.327.

Harrichhausen, N., Morell, K.D., Regalla, C., Bennett, S.E., Leonard, L.J., Lynch, E.M., Nissen, E., 2021. Paleoseismic trenching reveals Late Quaternary kinematics of the Leech River Fault: Implications for forearc strain accumulation in northern Cascadia Bull. Seismol. Soc. Am. https://doi.org/10.1785/0120200204.

Hawthorne, F.C., Oberti, R., Harlow, G.E., Maresch, W.V., Martin, R.F., Schumacher, J.C., Welch, M.D., 2012. Nomenclature of the amphibole supergroup. Am. Min 97, 2031-2048. http://doi.org/10.2138/am.2012.4276.

Henry, D.J., Guidotti, C.V., Thomson, J.A., 2005. The Ti-saturation surface for low-to-medium pressure metapelitic biotites: Implications for geothermometry and Ti-substitution mechanisms. Am. Min 90, 316-328. https://doi.org/10.2138/am.2005.1498.

Holland, T.J.B., Powell, R., 1998. An internally consistent thermodynamic data set for phases of petrological interest. J. metamorphic Geol. 16, 309-343. https://doi.org/10.1111/j.1525-1314.1998.00140.x.

Horstwood, M.S.A., Košler, J., Gehrels, G., Jackson, S.E., McLean, N.M., Paton, C., Pearson, N.J., Sircombe, K., Sylvester, P., Vermeesch, P., Bowring, J.F., Condon, D.J., Schoene, B., 2016. Community‐Derived Standards for LA‐ICP‐MS U‐(Th‐)Pb Geochronology ‐ Uncertainty Propagation, Age Interpretation and Data Reporting. Geostandards and Geoanalytical Research 40, 311-332. https://doi.org/10.1111/j.1751-908X.2016.00379.x.

Housen, B., Beck, M.E., 1999. Testing terrane transport: An inclusive approach to the Baja B.C. controversy. Geology 27, 1143-1146. https://doi.org/10.1130/0091-7613(1999)027<1143:TTTAIA>2.3.CO;2.

Hyndman, R.D., Yorath, C.J., Clowes, R.M., Davis, E.E., 1990. The northern Cascadia subduction zone at Vancouver Island: seismic structure and tectonic history. Can. J. Earth Sci. 27, 313-329. https://doi.org/10.1139/e90-030.

Irving, E., 1979. Paleopoles and paleolatitudes of North America and speculations about displaced terrains. Can. J. Earth Sci. 16, 669-694. https://doi.org/10.1139/e79-065.

Jacobson, C.E., Grove, M., Pedrick, J.N., Barth, A.P., Marsaglia, K.M., Gehrels, G., Nourse, J.A., 2011. Late Cretaceous–early Cenozoic tectonic evolution of the southern California margin inferred from provenance of trench and forearc sediments. Geol. Soc. Am. Bull. 123, 485-506. https://doi.org/10.1130/B30238.1.

Johnston, S.T., Acton, S., 2003. The Eocene Southern Vancouver Island Orocline — a response to seamount accretion and the cause of fold-and-thrust belt and extensional basin formation. Tectonophysics 365, 165-183. https://doi.org/10.1016/S0040-1951(03)00021-0.

Leake, B.E., Woolley, A.R., Arps, C.E.S., Birch, W.D., Gilbert, M.C., Grice, J.D., Hawthorne, F.C., Kato, A., Kisch, H., J., Krivovichev, V.G., Linthout, K., Laird, J., Mandarino, J.A., Maresch, W.V., Nickel, E.H., Rock, N.M.S., Schumacher, J.C., Smith, D.C., Stephenson, N.C.N., Ungaretti, L., Whittaker, E.J.W., Youzhi, G., 1997. Nomenclature of amphiboles: Report of the subcommittee on amphiboles of the International Mineralogical Association, Commission on new minerals and mineral names. Mineralogical Magazine 61, 295-310. https://doi.org/10.1180/minmag.1997.061.405.13.

Li, G., Liu, Y., Regalla, C., Morell, K.D., 2018. Seismicity relocation and fault structure near the Leech River Fault Zone, southern Vancouver Island. J. Geophys. Res. Solid Earth 123, 2841-2855. https://doi.org/10.1002/2017JB015021.

Locock, A.J., 2014. An Excel spreadsheet to classify chemical analyses of amphiboles following the IMA 2012 recommendations. Computers & Geosciences 62, 1-11. https://doi.org/10.1016/j.cageo.2013.09.011.

Ludwig, K.R., 2003. User's manual for Isoplot 3.00, a geochronological toolkit for Microsoft Excel. 4, 25-32.

Maruyama, S., Liou, J.G., Suzuki, O., 1982. The peristerite gap in low-grade metamorphic rocks. Contrib. Mineral. Petrol. 81, 268-276. https://doi.org/10.1007/BF00371681.

Maruyama, S., Suzuki, K., Liou, J.G., 1983. Greenschist-amphibolite transition equilibria at low pressures. J. Petrology 24, 583-604. https://doi.org/10.1093/petrology/24.4.583.

Massey, N.W.D., 1986. Metchosin Igneous Complex, southern Vancouver Island: Ophiolite stratigraphy developed in an emergent island setting. Geology 14, 602-605. https://doi.org/10.1130/0091-7613(1986)14%3C602:MICSVI%3E2.0.CO;2.

Matharu, G., Bostock, M.G., Christensen, N.I., Tromp, J., 2014. Crustal anisotropy in a subduction zone forearc:Northern Cascadia. J. Geophys. Res. Solid Earth 119, 7058-7078. https://doi.org/10.1002/2014JB011321.

Matthews, W.A., Guest, B., 2017. A Practical Approach for Collecting Large ‐ n Detrital Zircon U ‐ Pb Data sets by Quadrupole LA ‐ ICP ‐ MS. Geostandards and Geoanalytical Research 41, 161-180. https://doi.org/10.1111/ggr.12146.

Matthews, W.A., Guest, B., Coutts, D., Bain, H., Hubbard, S., 2017. Detrital zircons from the Nanaimo basin, Vancouver Island, British Columbia: An independent test of Late Cretaceous to Cenozoic northward translation. Tectonics 36, 854-876. https://doi.org/10.1002/2017TC004531.

McCrory, P.A., Wilson, D.S., 2013. A kinematic model for the formation of the Siletz-Crescent forearc terrane by capture of coherent fragments of the Farallon and Resurrection plates. Tectonics 32, 718-736. https://doi.org/10.1002/tect.20045.

Morell, K.D., Regalla, C., Leonard, L.J., Amos, C., Levson, V., 2017. Quaternary rupture of a Crustal Fault beneath Victoria, British Columbia, Canada. GSA Today 27, 4-10. https://doi.org/10.1130/GSATG291A.1.

Muller, J.E., 1977a. Evolution of the Pacific Margin, Vancouver Island, and adjacent regions. Can. J. Earth Sci. 14, 2062-2085. http://doi.org/10.1139/e77-176.

Muller, J.E., 1977b. Geology of Vancouver Island, British Columbia. Geological Survey of Canada, Open File 463. https://doi.org/10.4095/129265.

Muller, J.E., 1980. Geology, Victoria, British Columbia. Geological Survey of Canada, Open File 701. https://doi.org/10.4095/129114.

Mustard, P.S., 1994. The Upper Cretaceous Nanaimo Group, Georgia Basin, in: Monger, J. (Ed.), Geology and geological hazards of the Vancouver region, southwestern British Columbia, Geological Survey of Canada Bulletin 481, p. 320.

Nelson, J., Colpron, M., 2007. Tectonics and metallogeny of the British Columbia, Yukon, and Alaskan Cordillera, 1.8 Ga to the present, in: Goodfellow, W.D. (Ed.), Mineral Deposits of Canada: A Synthesis of Major Deposit-Types, District Metallogeny, the Evolution of Geological Provinces, and Exploration Methods. Geological Association of Canada, Mineral Deposits Division, Special Publication No. 5, pp. 755-791.

Paton, C., Woodhead, J.D., Hellstrom, J.C., Hergt, J.M., Greig, A., Maas, R., 2010. Improved laser ablation U‐Pb zircon geochronology through robust downhole fractionation correction. Geochem. Geophys. Geosyst. 11. https://doi.org/10.1029/2009GC002618.

Penniston-Dorland, S.C., Kohn, M.J., Manning, C.E., 2015. The global range of subduction zone thermal structures from exhumed blueschists and eclogites: Rocks are hotter than models. Earth Planet. Sci. Lett. 428, 243-254. http://doi.org/10.1016/j.epsl.2015.07.031.

Phillips, B.A., Kerr, A.C., Mullen, E.K., Weis, D., 2017. Oceanic mafic magmatism in the Siletz terrane, NW North America: Fragments of an Eocene oceanic plateau? Lithos 274-275, 291-303. https://doi.org/10.1016/j.lithos.2017.01.005.

104

Rusmore, M.E., 1982. Structure and petrology of pre-tertiary rocks near Port Renfrew, Vancouver Island, British Columbia. University of Washington.

Rusmore, M.E., Cowan, D.S., 1985. Jurassic-Cretaceous rock units along the southern edge of the Wrangellia terrane. Can. J. Earth Sci. 22, 1223-1232. https://doi.org/10.1139/e85-124.

Sakaguchi, A., 1996. High paleogeothermal gradient with ridge subduction beneath the Cretaceous Shimanto accretionary prism, southwest Japan. Geology 24, 795-798. https://doi.org/10.1130/0091-7613(1996)024%3C0795:HPGWRS%3E2.3.CO;2.

Shekut, S., Licht, A., 2020. Late Middle Miocene Emergence of the Olympic Peninsula Shown by Sedimentary Provenance. Lithosphere, 1-20. https://doi.org/10.2113/2020/7040598.

Simpson, R.W., Cox, A., 1977. Paleomagnetic evidence for tectonic rotation of the Oregon Coast Range. Geology 5, 585-589. https://doi.org/10.1130/0091-7613(1977)5<585:PEFTRO>2.0.CO;2.

Sláma, J., Košler, J., Condon, D.J., Crowley, J.L., Gerdes, A., Hanchar, J.M., Horstwood, M.S.A., Morris, G.A., Nasdala, L., Norberg, N., Schaltegger, U., Schoene, B., Tubrett, M.N., Whitehouse, M.J., 2008. Plešovice zircon — A new natural reference material for U-Pb and Hf isotopic microanalysis. Chemical Geology 249, 1-35. https://doi.org/10.1016/j.chemgeo.2007.11.005.

Spear, F.S., 1981. An experimental study of hornblende stability and compositional variability in amphibolite. Am. J. Sci. 281, 697-734.

Spear, F.S., 1995. Metamorphic Phase Equilibria and Pressure-Temperature-Time-Paths, 2nd ed.

Syracuse, E.M., van Keken, P.E., Abers, G.A., 2010. The global range of subduction zone thermal models. Phys. Earth Planet. Inter. 183, 73-90. https://doi.org/10.1016/j.pepi.2010.02.004.

Tajčmanová, L., Connolly, J.A.D., Cesare, B., 2009. A thermodynamic model for titanium and ferric iron solution in biotite. J. metamorphic Geol. 27, 153-165. https://doi.org/10.1111/j.1525-1314.2009.00812.x.

Timpa, S., Gillis, K.M., Canil, D., 2005. Accretion-related metamorphism of the Metchosin Igneous Complex, southern Vancouver Island, British Columbia. Can. J. Earth Sci. 42, 1467-1479. https://doi.org/10.1139/e05-043.

Tréhu, A.M., Asudeh, I., Brocher, T.M., Luetgert, J.H., Mooney, W.D., Nabelek, J.L., Nakamura, Y., 1994. Crustal architecture of the Cascadia forearc. Science 266, 237-243. https://doi.org/10.1126/science.266.5183.237.

Wells, R., Bukry, D., Friedman, R., Pyle, D., Duncan, R., Haeussler, P., Wooden, J., 2014. Geologic history of Siletzia, a large igneous province in the Oregon and Washington Coast Range: Correlation to the geomagnetic polarity time scale and implications for a long-lived Yellowstone hotspot. Geosphere 10, 692-719. https://doi.org/10.1130/GES01018.1.

Wells, R., Engebretson, D.C., Snavely Jr., P.D., Coe, R.S., 1984. Cenozoic plate motions and the volcano ‐ tectonic evolution of western Oregon and Washington. Tectonics 3, 275-294. https://doi.org/10.1029/TC003i002p00275.

White, R.W., Powell, R., Holland, T., Worley, B., 2000. The effect of TiO2 and Fe2O3 on metapelitic assemblages at greenschist and amphibolite facies conditions: mineral equilibria calculations in the system K2O-FeO-MgO-Al2O3-SiO2-H2O-TiO2-Fe2O3. J. metamorphic Geol. 18, 497-511. https://doi.org/10.1046/j.1525-1314.2000.00269.x.

White, R.W., Powell, R., Holland, T.J.B., 2007. Progress relating to calculation of partial melting equilibria for metapelites. J. metamorphic Geol. 25, 511-527. https://doi.org/10.1111/j.1525-1314.2007.00711.x.

Whitmeyer, S.J., Karlstrom, K.E., 2007. Tectonic model for the Proterozoic growth of North America. Geosphere 3, 220-259. https://doi.org/10.1130/GES00055.1.

Yorath, C.J., Sutherland Brown, A., Massey, N.W.D., 1999. LITHOPROBE, southern Vancouver Island, British Columbia. Geological Survey of Canada, Open File 498. https://doi.org/10.4095/210350.

Zumsteg, C.L., Himmelberg, G.R., Karl, S.M., Haeussler, P.J., 2003. Metamorphism within the Chugach accretionary complex on southern Baranof Island, southeastern Alaska, in: Sisson, V.B., Roeske, S.M., Pavlis, T.L. (Eds.), Geology of a transpressional orogen developed during ridge-trench interaction along the North Pacific margin. Geological Society of America Special Paper 371, Boulder, Colorado, pp. 253-267.

CHAPTER 4

Strength of the subduction interface below the seismogenic zone

Seyler, C.E., Kirkpatrick, J.D., Strength of the subduction interface below the seismogenic zone, in preparation for submission to Earth and Planetary Science Letters.

Abstract

Subduction interfaces below the seismogenic zone are expected to be relatively weak based on geophysical observations and geodynamic models, but very few estimates have been determined from the rock record. We estimate the strength of the subduction interface by evaluating the deformation mechanisms operating within an exhumed subduction interface—the Leech River Shear Zone (LRSZ) on Vancouver Island, British Columbia. The LRSZ is defined by a 600-m wide zone of mylonites across a lithologic contact with syn-kinematic temperatures of ~550-575 °C. Mylonites from metasedimentary rocks are composed of polymineralic layers of quartz, plagioclase, and phyllosilicates, and mylonites from metabasaltic rocks are mostly amphibole, plagioclase, and epidote. Quartz veins within the mylonites that deformed by dislocation creep are boudinaged, providing an upper bound on strength. Within the metasedimentary mylonites, polymineralic layers likely deformed by grain-size sensitive creep at low shear stresses, while phyllosilicate-rich layers deformed by dislocation glide. Amphibole within the metabasalt mylonites deformed by a combination of dissolution-precipitation creep and dislocation creep, while plagioclase deformed by diffusion creep. Overall, deformation on the subduction interface was accommodated by multiple deformation mechanisms operating in different phases, and available flow laws provide strength estimates of 1-10 MPa based on geologic strain rates, with the bulk strength significantly reduced by hydrous phases like phyllosilicates and amphibole.

4.1 Introduction

The strength of the subduction interface is fundamental in understanding how plate boundaries accommodate relative motion, informing models of seismic hazard and subduction zone dynamics. Subduction models rely on a weak interface to allow decoupling between the down-going slab and the upper plate (Duarte et al., 2015; Gerya et al., 2008), and the viscosity of the plate interface strongly influences the subduction velocity (Behr and Becker, 2018). Shear strength magnitudes required by numerical models are low (<35 MPa; Duarte et al., 2015; Richardson and Coblentz, 1994) and are well-matched with estimates derived from heat flow measurements (Gao and Wang, 2014; von Herzen et al., 2001; Wang et al., 1995) and seismic data (Bletery et al., 2017; Hardebeck, 2015). Most explanations of subduction interface weakness invoke frictional-viscous flow (e.g., Fagereng and den Hartog, 2016; Niemeijer and Spiers, 2005), pressure solution or dislocation creep in quartz (e.g., Behr and Platt, 2013; Platt et al., 2018), or the inherent weakness of hydrous minerals, like clay within subducting sediments (e.g., Okamoto et al., 2019) or serpentine in the mantle wedge (e.g., Auzende et al., 2015). However, there are few studies of subduction interfaces exhumed from below the seismogenic zone.

Strength and rheology of the subduction interface are dictated by the grain-scale mechanisms that accommodate deformation. Rheology is dependent on a myriad of factors, including temperature, pressure, strain rate, the presence or absence of fluids, and grain size, among others (Passchier and Trouw, 2005). But estimates of rock strength depend on the extrapolation of a handful of experimentally derived, single-mineral flow laws, each for a single deformation mechanism (e.g., Kohlstedt et al., 1995) or the application of paleopiezometry (e.g., Behr and Platt, 2013; Trepmann et al., 2017). These methods are traditionally based on monomineralic samples and strongly biased towards quartz. Shear zones, however, are often hosted by multiple lithologies, which contain more than a single mineral. Polymineralic rock strength is complicated by phase interactions (e.g., Zhao et al., 2019), their microstructural arrangement (e.g., Gerbi et al., 2015), and their viscosity contrasts (e.g., Holyoke and Tullis, 2006). Flow laws for single mineral phases can then be combined based on a particular set of assumptions about how stress and strain rate are partitioned in the rock, with end-member assumptions of isostrain or isostress bounding the possible range of bulk strength (Handy, 1994; Tullis et al., 1991). Previous experimental studies have demonstrated that even small proportions of a weaker phase can significantly reduce the bulk strength and partition strain into weak phase networks (e.g., Holyoke and Tullis, 2006; Tullis and Wenk, 1994). Other studies have highlighted the importance of diffusion-accommodated deformation mechanisms in polymineralic rocks, which can be weaker than the strength of single minerals (e.g., Fliervoet et al., 1997; Platt, 2015; Wheeler, 1992; Zhao et al., 2019). Despite these insights, our understanding of subduction interface rheology from the rock record is limited, especially for common yet understudied subduction minerals like phyllosilicates, amphibole, and epidote.

Application of experimental flow laws to natural shear zones requires the mineral assemblages at relevant temperatures to be determined, which can only be achieved through field observations of ancient, exhumed structures. The downdip transition beneath the seismogenic zone of subduction zones is thermally controlled as it is generally thought to coincide with the onset of plastic deformation mechanisms inside plate boundary shear zones (Hyndman and Wang, 1993; Oleskevich et al., 1999). Understanding this transition is important because the lower limit of the seismogenic zone sets the maximum size of megathrust earthquakes (e.g., Hyndman, 2013). The downdip regions of some subduction zones also exhibit a range of slow slip phenomena (e.g., Peng and Gomberg, 2010), which are poorly understood. However, exposures of deeply exhumed subduction interfaces are rare, so the specific deformation mechanisms that are important to subduction zone rheology are under-constrained and there are few examples that can be used to represent subduction zones with specific thermal structures. In this study, we investigate the Leech River Shear Zone (LRSZ) on Vancouver Island, British Columbia, which was a subduction plate interface in the Eocene before it was underplated (Chapter 3). The LRSZ formed as a relatively hot subduction interface that contained hydrated mineral assemblages in pelitic schist and metabasalt. The metamorphic conditions in the exposed section of the shear zone are comparable to those down dip of the seismogenic zone of the modern Cascadia subduction zone (Peacock, 2009). We use microstructural analyses to determine the dominant grain-scale deformation mechanisms accommodating relative plate motion, establish the bulk rheology of the shear zone, and estimate the strength of the plate interface at depth. The results indicate that deformation mechanisms active in the stable mineral assemblage had low strength, consistent with geophysical expectations.

4.2 Geologic setting

The LRSZ is an exhumed subduction plate interface that developed as the terrane boundary between the Late Cretaceous-Early Paleocene Leech River Schist and Eocene Metchosin Igneous Complex on southern Vancouver Island (Fig. 4-1; Chapter 3). The Metchosin Igneous Complex contains a ~3 km-thick ophiolite pseudostratigraphy consisting of gabbro stocks, sheeted dikes, and a sequence of basalt flows that transitions from submarine to subaerial up-section (Massey, 1986). The Metchosin Igneous Complex is part of the Siletz-Crescent Terrane, which is interpreted to be an underplated portion of a large igneous province that developed on the Farallon plate above

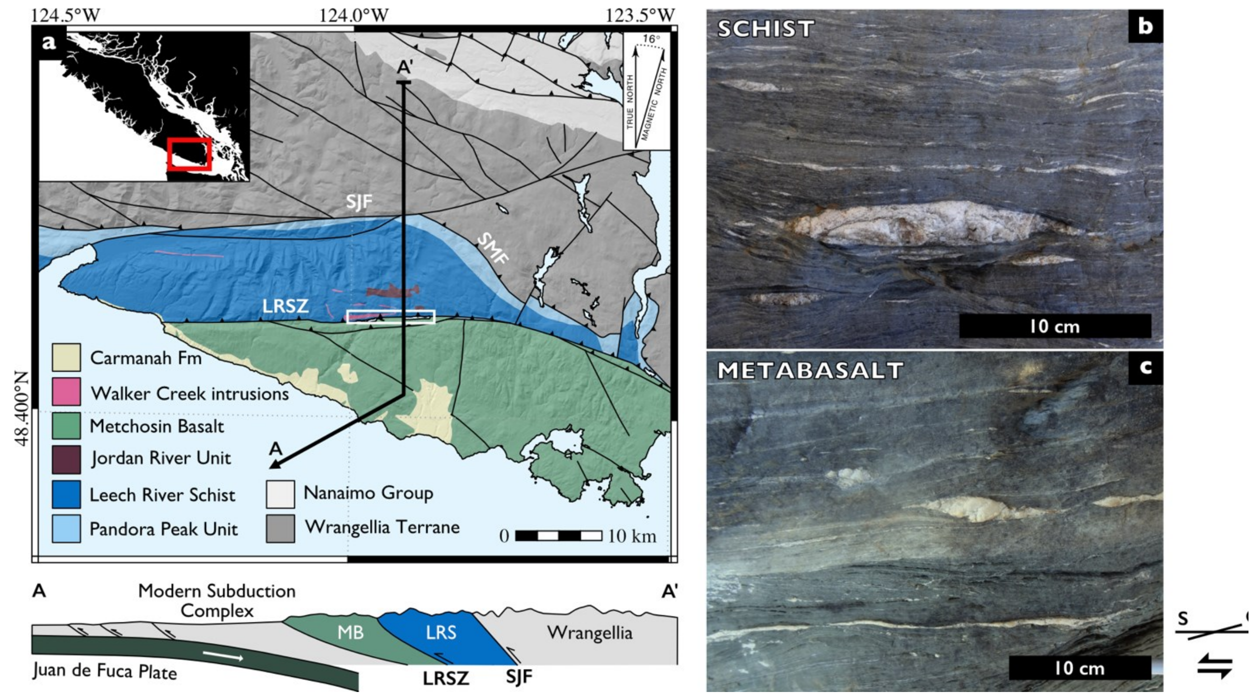

Figure 4-1: Geologic setting. a) Geologic map (adapted from Cui et al., 2017; Groome et al., 2003; Muller, 1980; Rusmore, 1982) and schematic cross section (adapted from Clowes et al., 1987; Hyndman et al., 1990). Field photos of **b)** schist mylonite and **c)** metabasalt mylonite showing strong foliation, C' shear bands, and boudinage of quartz veins and quartz-rich compositional layers. White box on geologic map outlines study area. LRSZ—Leech River Shear Zone; SJF—San Juan Fault; SMF—Survey Mountain Fault; MB—Metchosin Basalt; LRS—Leech River Schist.

the Yellowstone Hotspot offshore Vancouver Island (Phillips et al., 2017; Wells et al., 2014). Due to the proximity of the Kula-Farallon spreading ridge to the subduction margin at the time, the Metchosin basalts are inferred to have erupted onto relatively young oceanic crust. The Leech River Schist is an accretionary complex that consists of discontinuous layers of metamorphosed shales and sandstones with minor chert and basaltic volcanics, interpreted to have formed as a submarine, near-continental margin turbidite sequence (Fairchild and Cowan, 1982; Muller, 1980).

The sinistral-reverse-sense LRSZ is defined by a ~600-m wide zone of mylonites that trends east-west across southern Vancouver Island along the contact between the schist and basalt. Noncoaxial deformation is distributed across both lithologies, though in a broader zone in the schist (~400 m) than in the basalt (~200 m). The lithologic contact is rarely exposed but is sharp and planar in one observed location (Chapter 3.4.3). The mylonites in both lithologies have a pronounced, steeply dipping foliation defined by millimeter- to centimeter-thick compositional layering and a penetrative downdip stretching lineation, which are consistent with subduction of the metabasalt beneath the schist. The foliation forms S—C fabrics that are locally deflected along C' shear bands. In the schist, the layering is defined by transposed, isoclinally folded, sheared, and thinned primary bedding. In exposure, layers in the schist are dark to light grey, reflecting increases in quartz and plagioclase content. Lighter grey layers are discontinuous, typically terminating along strike within tens of centimeters, indicating boudinage of quartz- and plagioclase-rich layers was common. In the metabasalt, compositional layering reflects variations between plagioclase- and amphibole-rich layers. Quartz veins in both units exhibit planar, folded, and refolded geometries, indicating they were emplaced at different stages in the deformation history. The majority of veins are isoclinally folded and/or boudinaged, recording a significant amount of strain within the shear zone. Temperature and pressure conditions during deformation were ~575 °C and ~800 MPa as determined by Ti-in-biotite thermometry and the composition of syn-kinematic garnet and amphibole (Chapter 3.6.2). Both garnet and amphibole form asymmetric porphyroclasts, which show zonation consistent with growth during prograde metamorphism. The LRSZ therefore represents the downdip portion of an Eocene subduction interface formed between metasedimentary schists of an accretionary complex and a subducted oceanic plateau.

4.3 Methods

Oriented samples of mylonite were collected from the Leech River Shear Zone on Vancouver Island. Standard polished thin sections were prepared perpendicular to the foliation and parallel to the lineation (XZ plane) as well as perpendicular to the lineation (YZ plane) for optical and electron microscopy. Electron back scattered diffraction (EBSD) was used to quantify rock microstructures. For EBSD, thin sections of metabasalt mylonite were polished with colloidal silica on a Multipol-style system for 2 h. Thin sections of schist mylonite were polished with colloidal silica by hand for 5 min. To improve indexing of phyllosilicates, samples targeted for phyllosilicate mapping were also ion milled (Inoue and Kogure, 2012) with a Hitachi IM3000 flat milling system for two sessions of 20 minutes. EBSD maps were collected at McGill University under a low vacuum on a Hitachi SU5000 field emission SEM equipped with an Oxford Nordlys EBSD detector using 20 kV accelerating voltage, 60 spot intensity, and 18 µm working distance. Large area maps were acquired with the Oxford Instruments AZTEC software using 4x4 binning mode, 3 gain, 45-50 ms exposure time, and 1-20 µm step sizes. Step size was adjusted according to the grain size of the target map area to collect multiple points within each grain (Prior et al., 2009). Simultaneous element maps were collected with EDS under the same beam conditions. EBSD data was processed with the MTEX toolbox version 5.1.1 (Bachmann et al., 2010) to plot phase maps, orientation maps, misorientation maps, and point-per-grain pole figures as well as calculate fabric strength using M- and J-indices (Bunge, 1982; Skemer et al., 2005). Some grain boundary artefacts were produced at the edges where map panels were stitched together, creating anomalously straight boundaries. False-colored phase maps were produced by combining element maps in ImageJ (Rasband, 1997-2018).

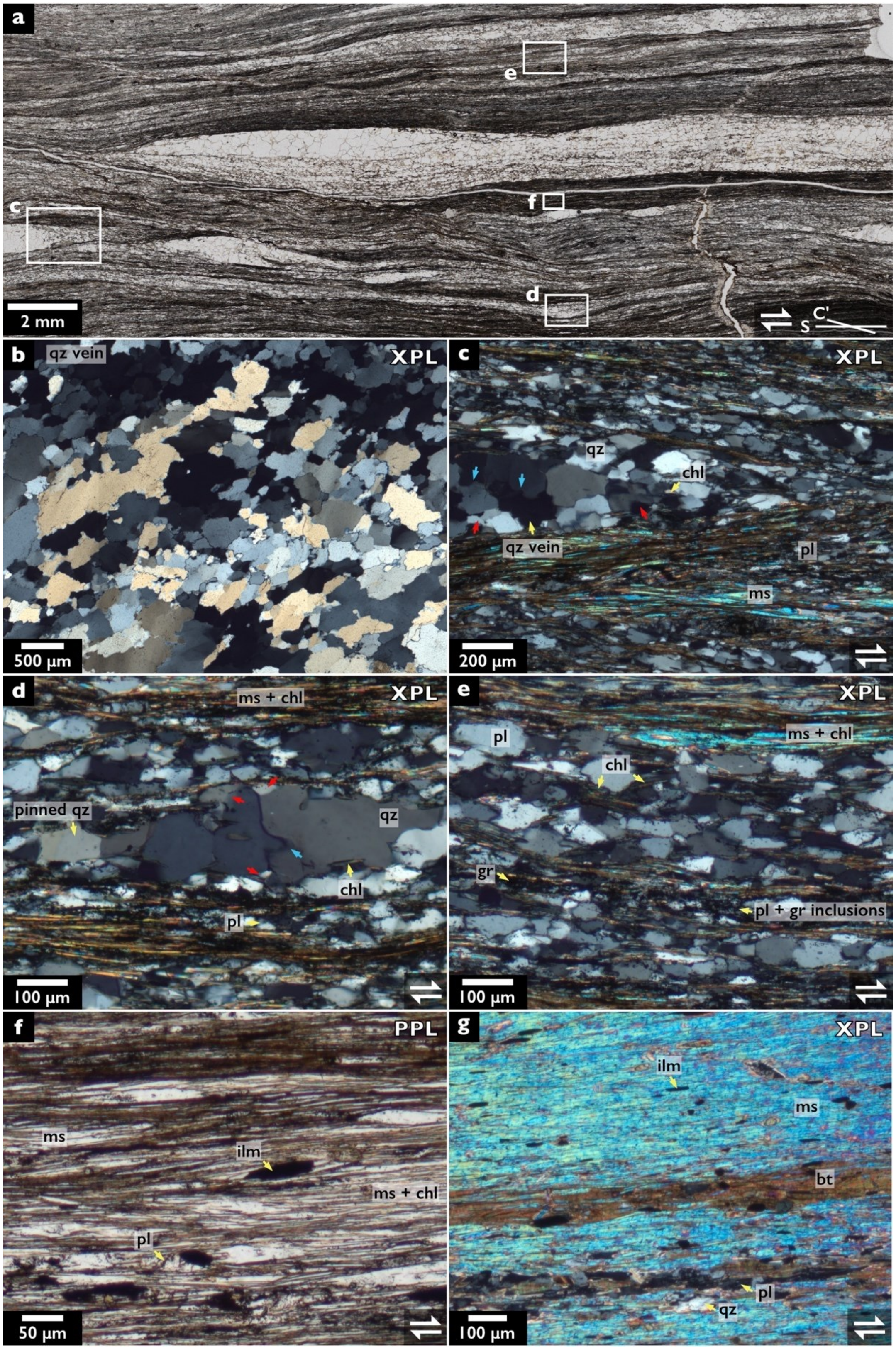
a
e
f
c
d
2 mm
S
C'
b
qz vein
XPL
500 µm
c
XPL
qz
chl
qz vein
pl
ms
200 µm
d
ms + chl
XPL
pinned qz
qz
chl
pl
100 µm
e
XPL
pl
ms + chl
chl
gr
pl + gr inclusions
100 µm
f
PPL
ms
ilm
ms + chl
pl
50 µm
g
XPL
ilm
ms
bt
pl
qz
100 µm

Figure 4-2: Schist mylonite microstructure. a) Quartz veins are boudinaged and isoclinally folded within a foliated matrix defined by compositional layering between quartz-dominated layers with minor chlorite, quartz-plagioclase layers, and phyllosilicate-dominated layers. Photomicrograph shows subfigure locations. **b-d)** In quartz veins and quartz ribbons, quartz shows a shape preferred orientation, lobate grain boundaries (blue arrows), subgrain development (red arrows) including chessboard subgrains, and pinning by mica grains. **e)** In plagioclase-rich layer, fine-grained plagioclase shows a shape preferred orientation. **f-g)** In phyllosilicate-rich layers, fine-grained muscovite, chlorite, and/or biotite are strongly aligned and elongated with high aspect ratios. Some biotite grains are oriented with basal planes at an angle to the foliation are not elongated, suggesting they are less deformed.

4.4 Microstructure and deformation mechanisms

4.4.1 Schist mylonite

The schist mylonite is fine-grained, strongly foliated and lineated and contains a syn-kinematic mineral assemblage of garnet + quartz + plagioclase + biotite + chlorite + muscovite + ilmenite. Relict andalusite and staurolite from an earlier high temperature-low pressure assemblage exhibit disequilibrium textures within the matrix (Chapter 3.4.3) The deformation fabric of the schist mylonite is dominated by compositional layering a few millimeters to 2-3 centimeters thick defined by quartz-rich layers, phyllosilicate-rich layers, and layers composed of a mixture of quartz, plagioclase, and phyllosilicates (Fig. 4-2a and 4-3a). Polymineralic layers are most common and contain a range of modal proportions of the constituent minerals. Some quartz-rich layers with minor plagioclase and phyllosilicates are present (i.e., quartz ribbons), but the vast majority of polymineralic layers (~75%) always contain ~10-50% phyllosilicates. Polymineralic layers have a secondary spaced foliation defined by alternating quartz-plagioclase-rich domains and phyllosilicate-rich domains. These layers are boudinaged when surrounded by phyllosilicate-rich layers. The compositional layers, along with the alignment of platy minerals, and a grain shape preferred orientation in quartz and plagioclase define the foliation. Layers exhibit the same S—C and C' shear bands observed in outcrop (Fig. 4-1b), which are consistent with asymmetry of tails around garnet porphyroblasts.

Quartz occurs within veins (Fig. 4-2b,c), quartz ribbons (Fig. 4-2d), and polymineralic layers (Fig. 4-2e). Quartz veins and quartz ribbons are asymmetrically isoclinally folded and boudinaged, consistent with the reverse-sense shear direction (Fig. 4-2a). Vein quartz is relatively coarse-grained, with grains up to hundreds of microns in diameter (Fig. 4-2b,c), while grain size within quartz ribbons (~50-250 µm) is constrained by the width of the layer (Fig. 4-2d). Irregular grain shapes, lobate grain boundaries, and development of chessboard subgrains within quartz veins and quartz ribbons are all characteristic of grain boundary migration (GBM) recrystallization (Hirth and Tullis, 1992; Stipp et al., 2002). Pinning by dispersed phyllosilicates reduced the recrystallized grain size, especially at boudin edges where the fraction of phyllosilicates is greater. Quartz vein c-axes (Map 1; Fig. 4-4) form a cross girdle, and internal grain misorientations, defined as the magnitude of the lattice rotation away from the average grain orientation, illustrate the presence of ~50-100 µm diameter subgrains (Fig. 4-4f). Quartz c-axes within quartz ribbons (Map 2; Fig. 4-4) have a weak maximum normal to the shear direction within the shear plane, but internal grain misorientations demonstrate subgrain development, particularly within large grains (Fig. 4-4g).

Within the polymineralic layers, fine-grained (~10-50 µm) quartz and plagioclase have a shape preferred orientation with grains weakly elongated in the shear direction (Fig. 4-2e and 4-3a,b). Quartz and plagioclase are interspersed within these layers, making it difficult to discern grain boundaries from phase boundaries. Where observable, most quartz-quartz grain boundaries are

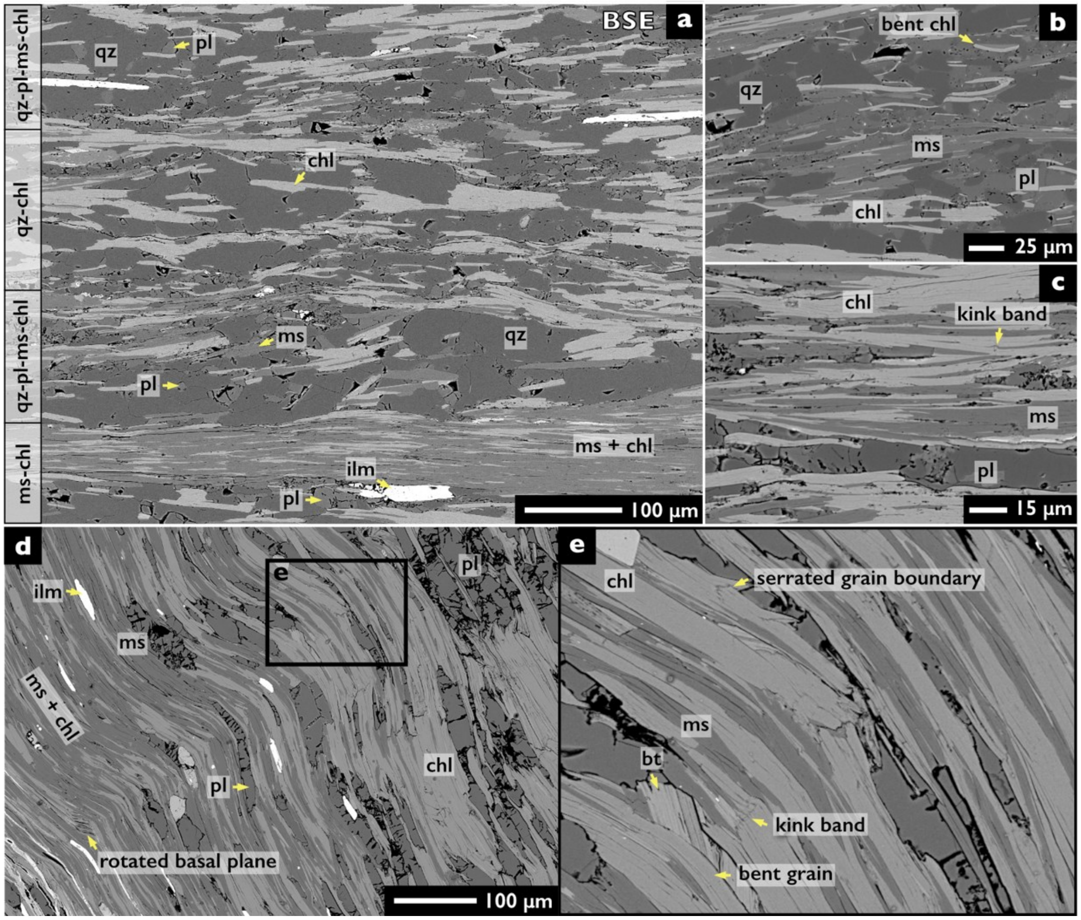

Figure 4-3: Phyllosilicate grain size and shape. a) Phyllosilicate grain size and aspect ratios are distinct between phyllosilicate-rich layers and layers where phyllosilicates are mixed with quartz and/or plagioclase. **b)** In polymineralic layers, chlorite grains are bent around other phases, indicative of crystal plastic deformation. **c)** Kink band developed in phyllosilicate-rich layer. **d-e)** Kink band developed within folding of the foliation, serrated grain boundaries in chlorite, and a biotite grain with its basal plane at an angle to the foliation.

straight, with only a few examples of irregular grain boundaries, and there is minimal subgrain development. Quartz and plagioclase grain size in these layers is likely limited by both mutual pinning between quartz and plagioclase as well as dispersed grains of chlorite and muscovite (cf. Hunter et al., 2016; Song and Ree, 2007). Quartz c-axes in polymineralic layers (Maps 3 and 4; Fig. 4-4) have a weak pattern and internal grain misorientations show moderate development of subgrains and deformation bands (Fig. 4-4e). Plagioclase has a near uniform distribution of crystal lattice orientations (Maps 2-3; Fig. 4-4), minimal internal misorientations, and no subgrain development (Fig. 4-4e,g).

Phyllosilicates occur within the polymineralic layers as well as in phyllosilicate-rich layers (Fig. 4-2f,g and 4-3c). In all layers, phyllosilicate basal planes are strongly aligned with the local foliation. Phyllosilicates within the quartz-plagioclase domains of polymineralic layers have a similar grain size to the quartz and plagioclase (~10-50 μm) and have relatively low aspect ratios. Chlorite grains are locally bent or kinked around quartz or plagioclase grains (Fig. 4-3a,b). In phyllosilicate-rich layers, chlorite, muscovite, and/or biotite grain sizes range from 1-100 μm, but the overall grain size is reduced relative to the adjacent quartz-plagioclase domains, and grains are extremely elongated in the lineation direction with high aspect ratios. A few relatively large, lower aspect ratio grains persist in these layers (e.g., large, clear muscovite grains in Fig. 4-2f), and occasional, relatively equant grains have basal planes at an angle to the foliation. The formation of kink bands is rare, and they most often occur locally within micro-scale folds or near phase boundaries with plagioclase (Fig. 4-3c,d). Grain boundaries parallel to basal planes are straight and smooth, but grain boundaries normal to basal planes are irregular, often exhibiting interlocking patterns between phyllosilicate phases and there are some examples of serrated grain boundaries in chlorite (Fig. 4-3e). Muscovite has a strong lattice-preferred orientation (LPO) (Fig. 4-5), with (001) planes strongly aligned with the foliation, and [100] and (010) forming girdles within the shear plane, which contain weak clusters. Internal grain misorientation maps for individual grains show the development of tilt walls subperpendicular to foliation via rotation around the (001) and (100) directions (Fig. 4-5e,f; cf. Bestmann et al., 2011; Padrón-Navarta et al., 2012).

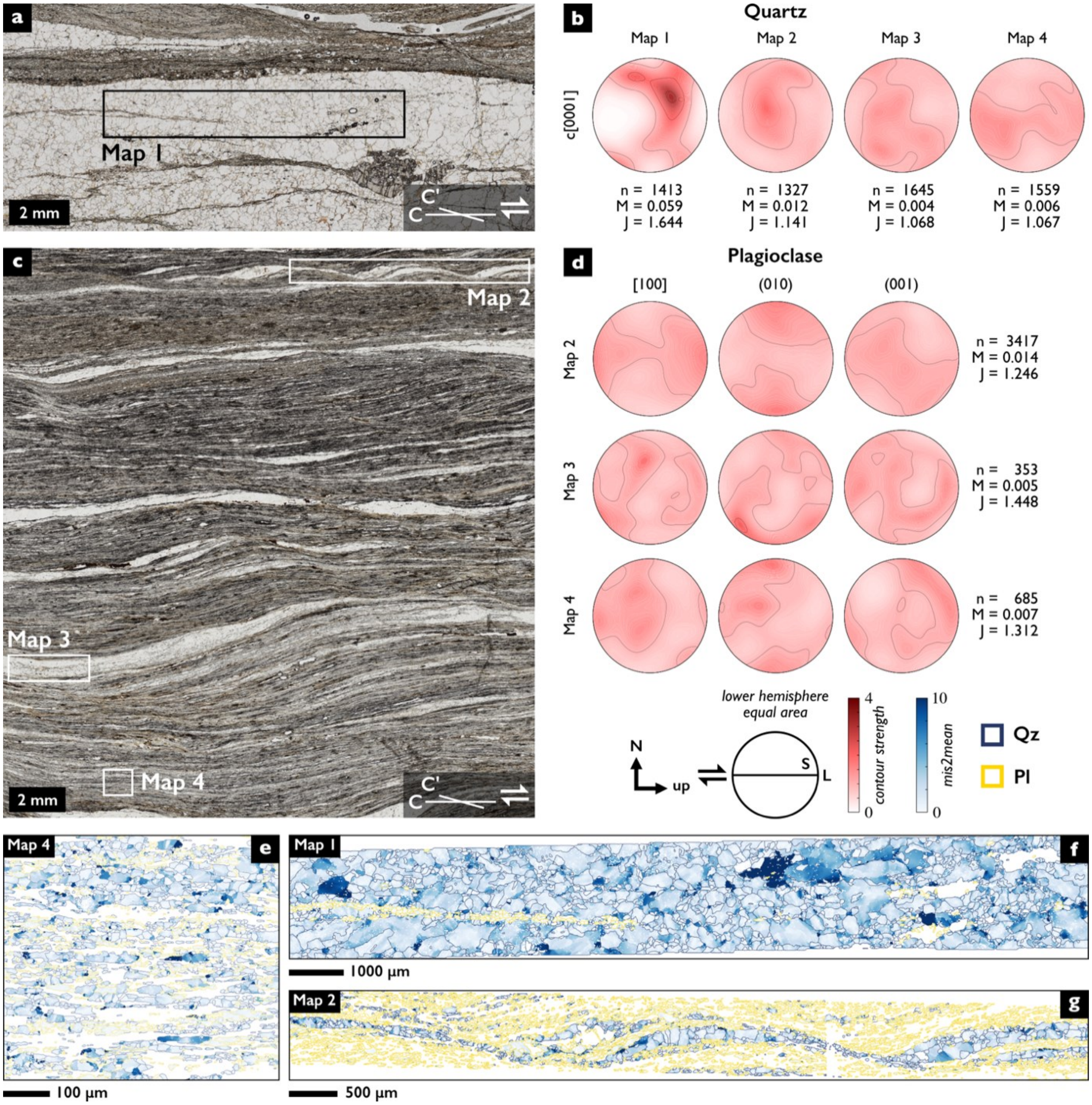

Figure 4-4: LPO and misorientations of quartz and plagioclase in schist mylonite. a, c) Photomicrographs of quartz vein and schist mylonite, respectively, showing map locations. **b)** Quartz c-axes show the development of a cross girdle within the quartz vein in map 1, weak clustering in the quartz layer in map 2, but no pattern in quartz from polymineralic layers in maps 3 and 4. **d)** Plagioclase LPOs are weak to random in all maps. **e-g)** Quartz and plagioclase intragranular misorientations. Pole figures are equal area lower hemisphere projections contoured with a halfwidth of 15° and a contour interval of 1.

4.4.2 Metabasalt mylonite

The metabasalt mylonite is moderately fine-grained, strongly foliated and lineated, and composed of amphibole + plagioclase + epidote + ilmenite + titanite (Fig. 4-6a), which is interpreted to represent the syn-kinematic assemblage at the peak P-T conditions. The fabric is dominated by large (~100-1000 μm) amphibole porphyroclasts with chemically distinct cores and asymmetric tails, which are surrounded by ribbons of plagioclase and seams of titanite and ilmenite parallel to S and deflected into local C' shear bands (Fig. 4-6b and 4-7a,c), forming the same S—C fabrics and C' shear bands observed in outcrop (Fig. 4-1c). Two microstructural domains are present in the finer-grained matrix surrounding the amphibole porphyroclasts: amphibole mixed with plagioclase (Fig. 4-7a,c) and amphibole mixed with both plagioclase and epidote (Fig. 4-7b,d). In the former, amphibole matrix grains are ~50-200 μm and relatively equant. Plagioclase is segregated into ribbons in which grains are ~10-50 μm. In the latter, amphibole is ~10-100 μm long, but grains have large aspect ratios, which together potentially indicate grain size reduction by dynamic recrystallization. Plagioclase and epidote tend to be mixed together and have grain sizes of around tens of microns. Narrow, fine-grained bands are deflected into C' shear bands.

Asymmetric tails on large amphibole porphyroclasts (~50-500 μm) are locally aligned with the S or C' orientation and show some crystal lattice misorientation relative to the grain core (Fig. 4-6b,d). Phase maps constructed from chemical data show chemical zoning between the light green actinolite cores and dark green hornblende tails of amphibole porphyroclasts (Fig. 4-8a; Fig 3-10; Chapter 3.4.3.2). The chemical zoning is often truncated along the foliation and tails extend in the shear direction, indicative of dissolution and re-precipitation. All amphibole domains have a strong LPO with (100) planes aligned with the shear plane and [001] axes (i.e., shortest Burgers vector;

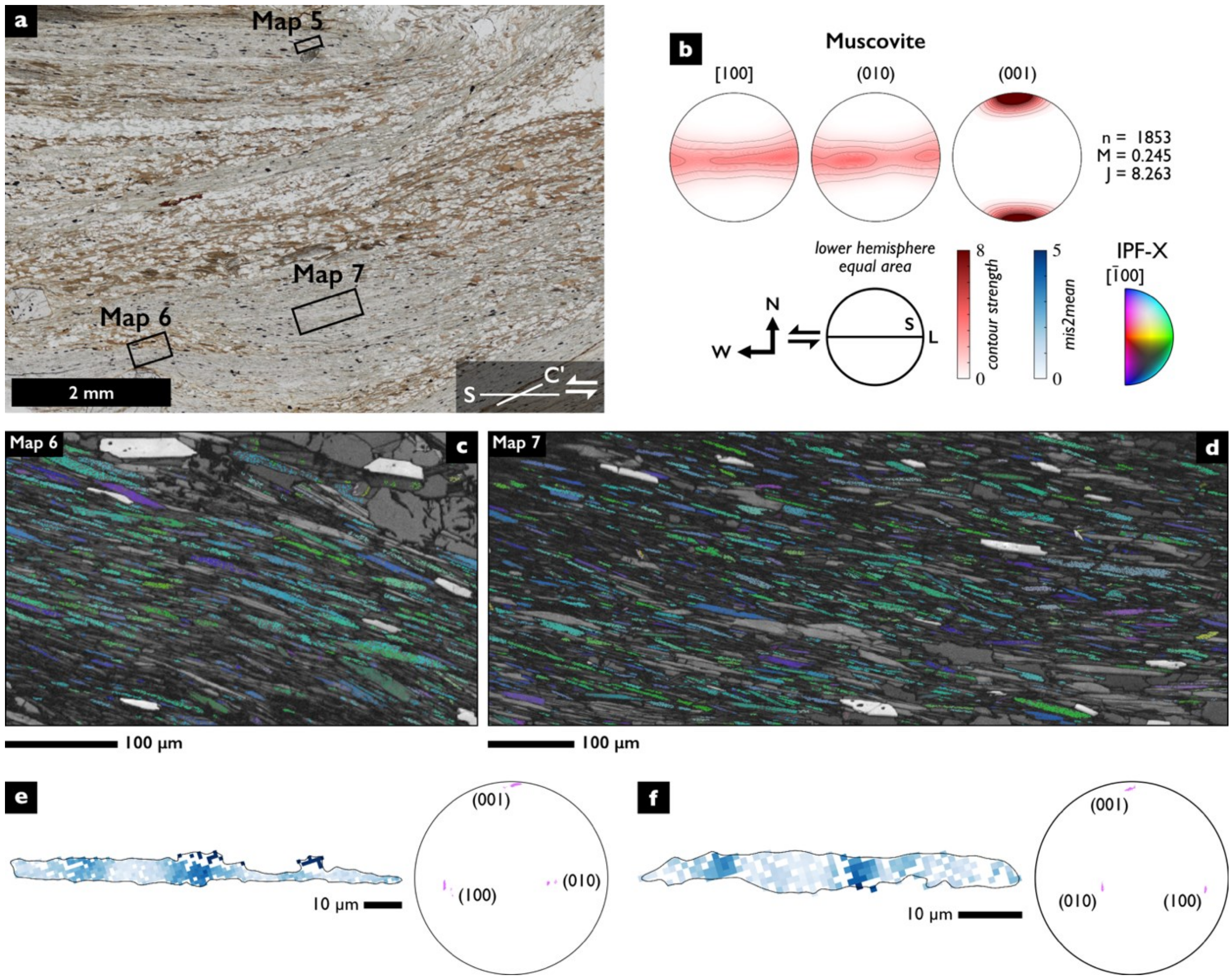

Figure 4-5: LPO and misorientations of muscovite in schist mylonite. a) Photomicrograph showing map locations within muscovite-chlorite layers. **b)** Muscovite LPO shows girdles in the [100] direction and (010) planes and strong clustering of (001) basal planes. **c-d)** IPF-X orientations of muscovite. **e-f)** Single grain misorientations of muscovite showing the developed of tilt walls subperpendicular to basal planes accommodated by rotation around [001] and [100] axes, show on pole figures. Pole figures are equal area lower hemisphere projections contoured with a halfwidth of 15° and a contour interval of 1.

Hacker and Christie, 1990) aligned with the shear direction (Fig. 4-9a). Amphibole porphyroclasts have significant internal misorientations indicative of subgrain development (Fig. 4-10a). Misorientation maps for individual porphyroclasts show subgrain boundaries subparallel and subperpendicular to the shear plane that formed via rotation around the [100] and [010] axes (Fig.

4-10c,d). Misorientation maps for finer, possibly recrystallized grains show rotation around the [010] axis dominates.

In fine-grained bands from the plagioclase-epidote matrix domain, amphibole exhibits a shape preferred orientation with long axes parallel to C planes or C' shear bands (Fig. 4-6e). Some coarse-grain amphibole porphyroclasts remain and have similar microstructural characteristics to porphyroclastic grains within the main fabric, including asymmetric tails, truncated chemical zoning (Fig. 4-8b), a strong LPO with the same pattern as the main fabric (Fig. 4-9b), and internal misorientations and subgrain development (Fig. 4-10b). Even in the finer grain amphibole, few grains lack chemical zoning, and the majority of pure hornblende grains appear to be recrystallized from the hornblende tails of porphyroclasts. Additionally, there is no difference in LPO or misorientation patterns between fine-grained, presumably recrystallized grains and the large porphyroclasts.

Plagioclase in the mixed amphibole and plagioclase domains is fine-grained (~10-50 μm) and occurs as discontinuous ribbons between amphibole porphyroclasts (Fig. 4-6a,b and 4-7a). Grain boundaries are straight, and most grains have a shape preferred orientation, elongated in the shear direction. Where fine-grained plagioclase is interspersed with amphibole and epidote, plagioclase has a smaller grain size (~5-25 μm), possibly related to phase mixing and pinning with epidote (Fig. 4-6e and 4-7b). Epidote grains are slightly larger than plagioclase (~10-40 μm), and also have a weak shape preferred orientation. Plagioclase has a near uniform distribution of crystal lattice orientations in both microstructural domains, while epidote has a weak LPO, with a girdle of [100] axes normal to the shear direction, (010) oriented normal to the shear plane, and (001) aligned with

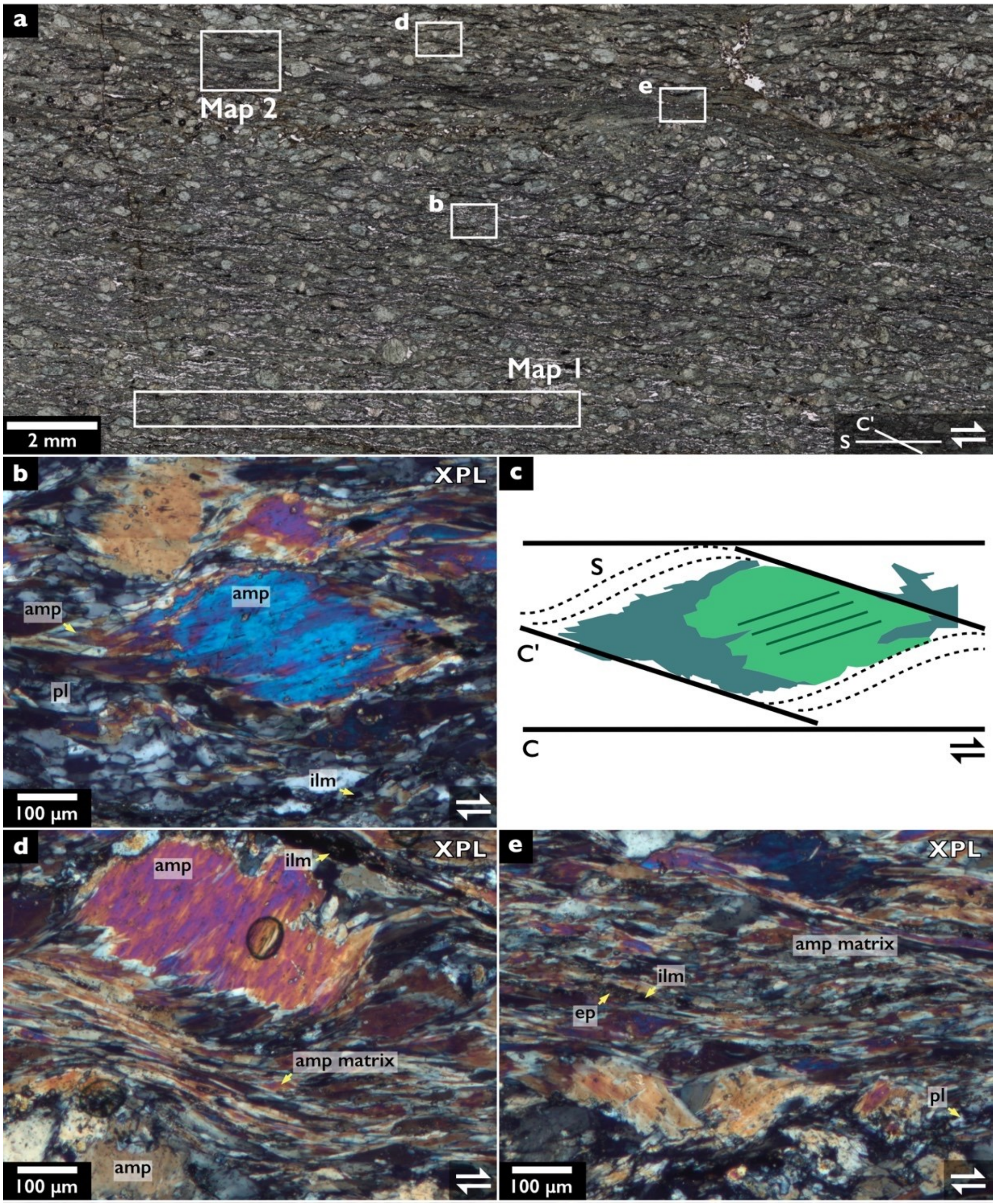

Figure 4-6: Metabasalt mylonite microstructure. a) Large amphibole porphyroclasts, fine-grained amphibole, and fine-grained plagioclase ribbons form an S—C composition foliation deflected by C' shear bands. Photomicrograph shows subfigure and map locations. **b,d)** Photomicrographs of large amphibole porphyroblasts with syn-kinematic tails aligned with C' shear bands. **c)** Schematic cartoon of amphibole porphyroclast tails aligned with C' shear bands. **e)** Fine-grained amphibole layer surrounded by a plagioclase and epidote matrix.

the shear plane. (Fig. 4-9). In agreement with the pole figures, plagioclase grains show no internal misorientations, while epidote shows only minor subgrain development (Fig. 4-10a,b).

4.5 Discussion

The observations presented in the previous section document a range of textures in the mineral phases that coexisted and accommodated strain at the peak metamorphic conditions. Asymmetric deformation structures and composite foliations developed at exposure to thin section scales are all consistent with a reverse-sinistral, slightly oblique sense of shear across the shear zone, which we interpret to represent deformation in the subduction megathrust. In this section, we define the deformation mechanisms active in each mineral phase and the interactions of mechanisms in mixtures of mineral phases. We then use these insights to discuss the implications for the rheology of the subduction interface.

4.5.1 Deformation mechanisms

4.5.1.1 Quartz

Deformation in quartz veins was accommodated by dislocation creep. The grain boundary migration (GBM) recrystallization microstructures, large recrystallized grain size, and cross girdle c-axis pattern are characteristic of dislocation creep under moderately high temperature and low stress conditions (Hirth and Tullis, 1992; Jessell, 1987; Stipp et al., 2002). The cross-girdle c-axis pattern is achieved through a combination of basal <a>, rhomb<a>, and prism <a> slip (Passchier and Trouw, 2005; Schmid and Casey, 1986). Quartz opening angle thermometry following the method of Law (2014) indicates deformation temperatures of ~550-600 °C (Fig. 4-11), consistent with GBM recrystallization as well as the temperature of deformation reported in Chapter 3. Quartz

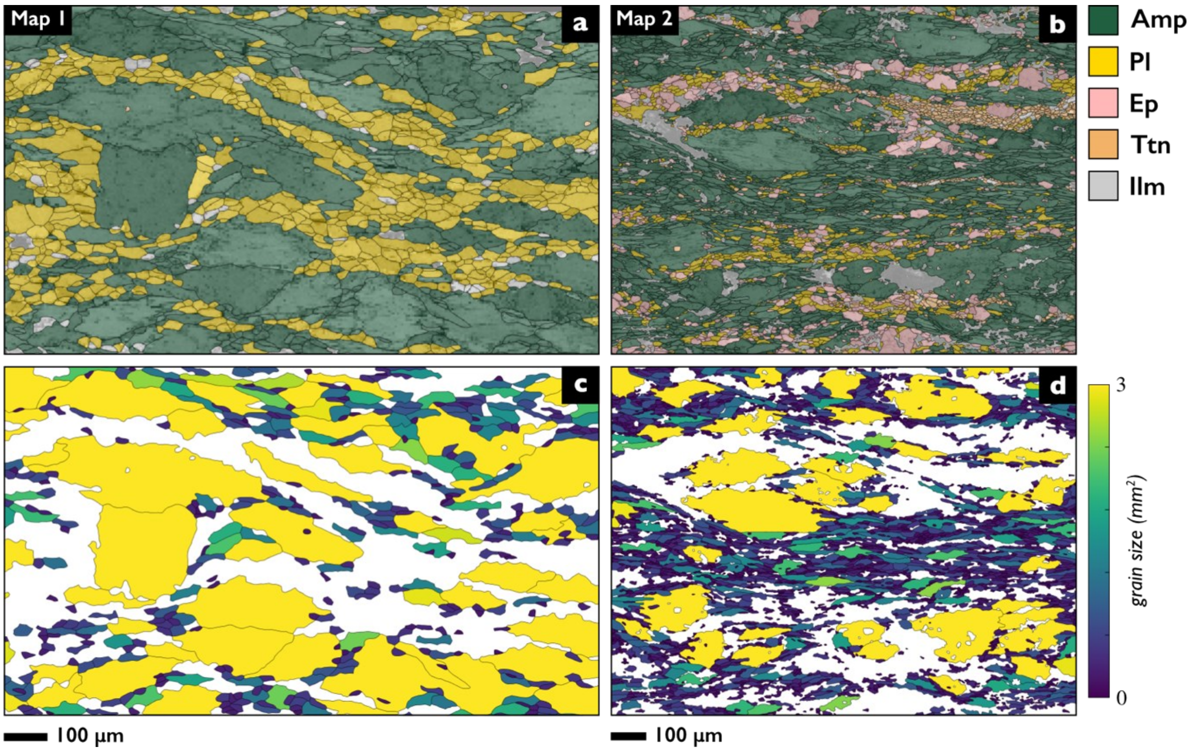

Figure 4-7: Grain size reduction in metabasalt mylonite. a-b) EBSD phase maps overlaying band contrast. **c-d)** Amphibole grain size maps demonstrating grain size reduction where epidote is present in the matrix. The grain area color bar saturates at 3 mm^2 to distinguish between amphibole porphyroclasts (yellow grains with areas ≥3 mm^2) and matrix grains (<3 mm^2).

within ribbon layers also exhibited characteristics typical of GBM recrystallization, including lobate grain boundaries, "island grains" created by the 2D sectioning of interlobate grains, and pinning by secondary phases. The weak c-axis maximum normal to the shear direction is produced by the greater contribution of prism<a> slip (Passchier and Trouw, 2005; Schmid and Casey, 1986). Therefore, deformation within these quartz ribbons was also likely accommodated by dislocation creep.

Quartz within the polymineralic quartz-plagioclase-phyllosilicate layers is finer-grained than the quartz within veins or ribbons and exhibits microstructural characteristics of dislocation creep and

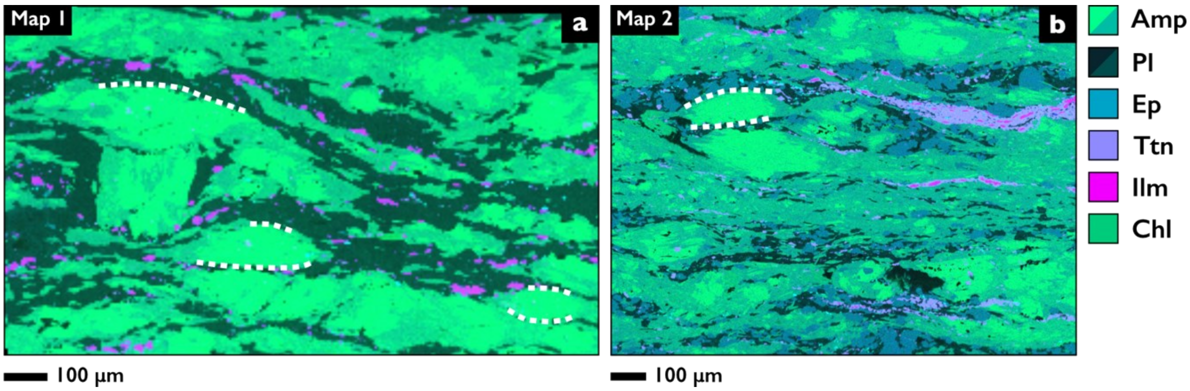

Figure 4-8: Phase maps of metabasalt mylonite. False-color phase maps constructed from WDS element maps show chemical zoning between actinolite cores and hornblende tails. Chemical zoning is truncated along foliation surfaces (white dotted lines). Fine-grained amphibole in the matrix matches the tail composition. Ilmenite and titanite occur as seams along the foliation.

grain-size sensitive creep. For example, internal misorientations and a few examples of irregular grain boundaries suggest dislocation-accommodated creep, but the lack of LPO and mixing of fine-grained quartz and plagioclase are consistent with grain-size sensitive creep. Straight quartz boundaries parallel to spaced phyllosilicates may also indicate dissolution of the quartz. Previous studies of fine-grained quartz have documented simultaneous activation of diffusion and dislocation creep (Fukuda et al., 2018), while other studies have suggested that diffusion-accommodated grain boundary sliding, which results in well-mixed phases, is a common mechanism in fine-grained polymineralic rocks (Ashby and Verrall, 1973; Etheridge and Wilkie, 1979; Fliervoet et al., 1997; Miranda et al., 2016; Stünitz and Tullis, 2001). Therefore, quartz within polymineralic layers deformed via a combination of diffusion- and dissolution-controlled grain-size sensitive deformation mechanisms.

4.5.1.2 Phyllosilicates

Phyllosilicates are generally presumed to deform by dislocation glide via "easy" and "hard" slip along basal planes (Bell et al., 1986; Kronenberg et al., 1990; Meike, 1989). Naturally and experimentally deformed phyllosilicates often exhibit kinking, which is characteristic of dislocation glide (Behrmann, 1984; Bell and Wilson, 1981; Bell et al., 1986; Bons, 1988; Borg and Handin, 1966; Christoffersen and Kronenberg, 1993; Kronenberg et al., 1990; Mares and Kronenberg, 1993; Mariani et al., 2006; Misra and Burg, 2012; Shea and Kronenberg, 1993; Vernon, 1977; Wilson and Bell, 1979). LPO studies on deformed phyllosilicates are few, but they typically have LPO patterns with (001) planes aligned with the foliation and [100] and [010] axes forming a girdle within the foliation plane (Dempsey et al., 2011; Ha et al., 2018; Naus-Thijssen et al., 2011; Tulley et al., 2020; Wallis et al., 2015), matching our observed LPO and compatible with easy slip along the (001) plane. This LPO is consistent with the shape preferred orientation of basal planes parallel with foliation, influenced by their strong crystallographic anisotropy and platy crystal habit. Although single-grain misorientation maps indicate intracrystalline plasticity of phyllosilicates, grains in the phyllosilicate-rich layers of the schist mylonite are rarely kinked. Instead, grains in the phyllosilicate-rich layers are extremely elongated and sometimes smoothly bent around other phases. The lack of kink bands despite dislocation mobility and grain size reduction in phyllosilicate-rich layers relative to polymineralic layers suggests that they were destroyed, either through fracturing (i.e., Goodwin and Wenk, 1990), grain boundary sliding, or recrystallization via an unknown mechanism. Grain-scale evidence for fracturing in the phyllosilicates is rare, and where present cracks are developed along (001) planes. Combined with irregular, interlocking grain boundaries normal to basal planes, this suggests dynamic

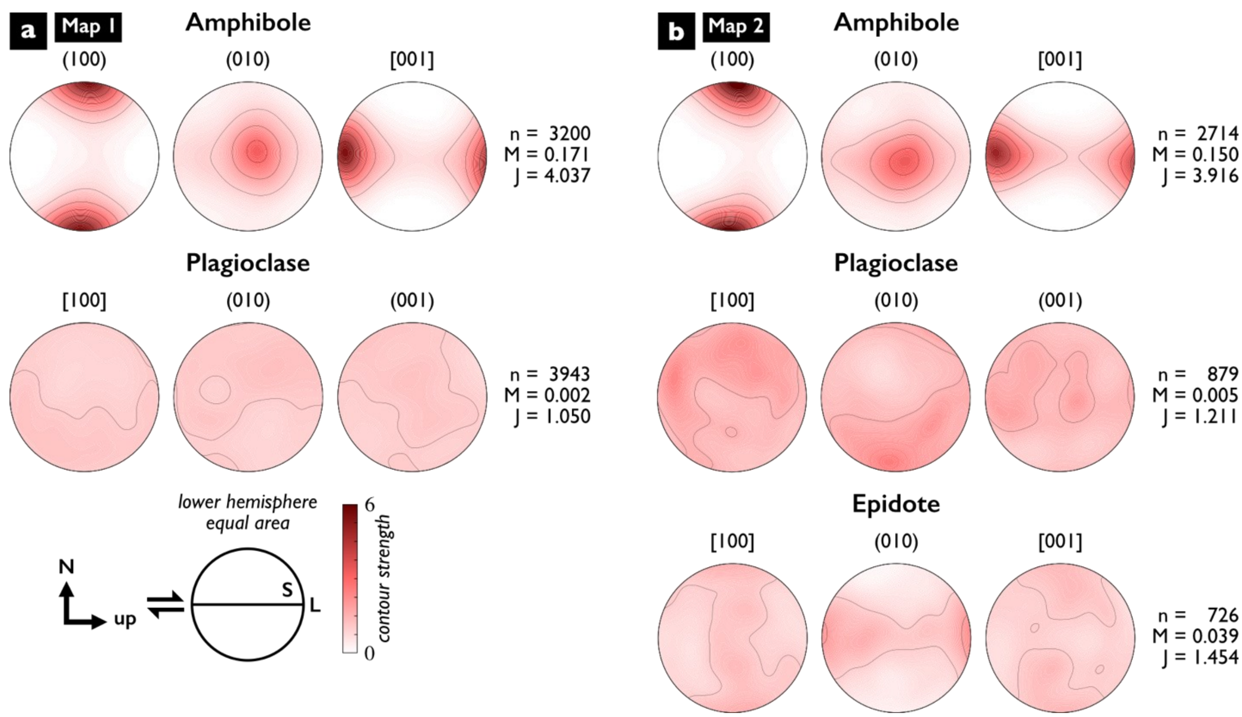

Figure 4-9: LPO in metabasalt mylonite. a) In the plagioclase matrix domain, amphibole LPO is strong, while plagioclase LPO is weak to random. **b)** In the plagioclase-epidote matrix domain, amphibole and plagioclase LPOs match those from the plagioclase matrix domain, and epidote LPO is weak. Pole figures are equal area lower hemisphere projections contoured with a halfwidth of 15° and a contour interval of 1.

recrystallization was the dominant recovery mechanism. Deformation of phyllosilicates was therefore likely accommodated by dislocation glide accompanied by dynamic recrystallization.

4.5.1.3 Plagioclase

Diffusion creep in plagioclase is the dominant deformation mechanism for temperatures > 400 °C and grain sizes <50 µm (Rybacki and Dresen, 2004), and is commonly documented in high grade quartzofeldspathic (e.g., Gower and Simpson, 1992) and metamafic rocks (e.g., Getsinger et al., 2013). Near uniform distributions of crystal lattice orientations and small grain sizes of ~10-50 µm in the schist mylonites and ~5-25 and ~10-50 µm in the metabasalt mylonite indicate deformation in plagioclase in both units was accommodated by diffusion creep. In the schist, phase boundaries are common in the polymineralic layers, so deformation of plagioclase within polymineralic layers in the schist may have been accommodated by an alternative grain-size sensitive mechanism such as grain boundary sliding (e.g., Condit and Mahan, 2018; Mehl and Hirth, 2008; Miranda et al., 2016).

4.5.1.4 Amphibole

Deformation mechanisms previously documented in amphibole include rigid grain rotation, cataclasis and semi-brittle flow (Allison and La Tour, 1977; Babaie and La Tour, 1994; Hacker and Christie, 1990; Nyman et al., 1992), fracturing and dissolution-precipitation creep (DPC) (Berger and Stünitz, 1996; Díaz Aspiroz et al., 2007; Imon et al., 2002; Imon et al., 2004; Marti et al., 2018; Soret et al., 2019; Stokes et al., 2012), diffusion creep (Getsinger and Hirth, 2014), and dislocation glide and creep (Cao et al., 2010; Dollinger and Blacic, 1975; Elyaszadeh et al., 2018; Hacker and Christie, 1990; Kruse and Stünitz, 1999). Dynamic recrystallization of amphibole has also been recognized (Cao et al., 2010; Cumbest et al., 1989; Díaz Aspiroz et al., 2007; Elyaszadeh et al., 2018; Kruse and Stünitz, 1999).

The truncated chemical zoning, shape-preferred orientation, elongation of porphyroclast tails into the shear bands, and solution seams of oxides indicate that DPC was active in the amphibole (Wassmann and Stöckhert, 2013). LPOs with (100) planes aligned with the foliation, poles to (010) planes in the foliation plane and subperpendicular to the lineation, and [001] axes parallel with the lineation are commonly observed in naturally deformed amphibole (Berger and Stünitz, 1996; Cao et al., 2010; Díaz Aspiroz et al., 2007; Elyaszadeh et al., 2018; Getsinger and Hirth, 2014; Hacker

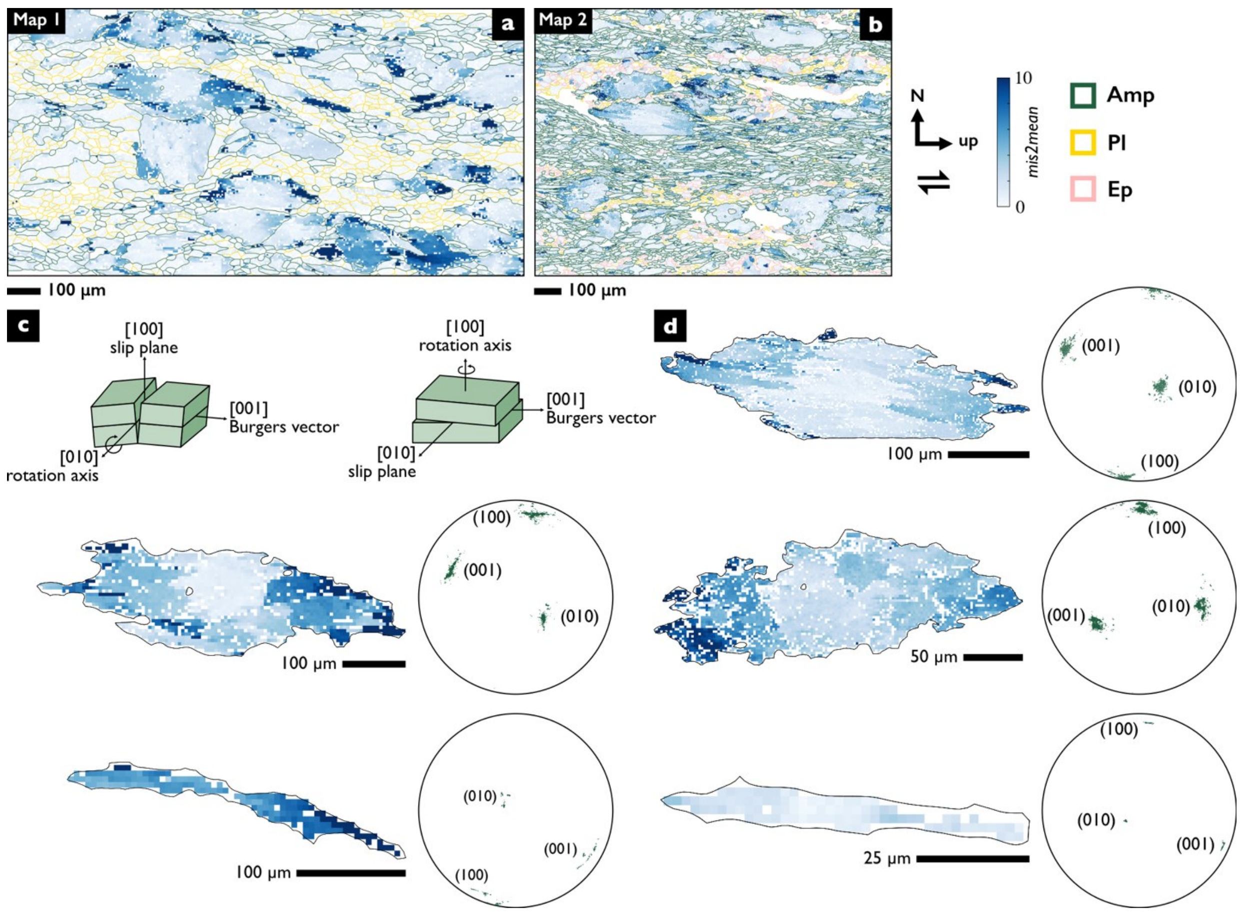

Figure 4-10: Amphibole misorientations in metabasalt mylonite. a-b) Internal grain misorientation maps of amphibole and plagioclase. **c)** Schematic cartoons of slip systems in amphibole. **d)** Single grain misorientations of amphibole exhibiting subgrain development accommodated by rotation around [010] and [100] axes.

and Christie, 1990; Imon et al., 2004; Tatham et al., 2008). Strong LPOs can originate from rigid grain rotation, oriented growth, or dislocation creep, so the LPO we observe is not immediately indicative of second required mechanism and may be formed from oriented growth during DPC (e.g., Imon et al., 2004; Marti et al., 2018), but could also be indicative of dislocation creep. Because there is no difference in the LPO between large porphyroclasts and finer grains within the matrix, only a small increase in LPO strength in fine-grained amphibole, it is likely the LPO in the large porphyroclasts originated from oriented growth during prograde metamorphism.

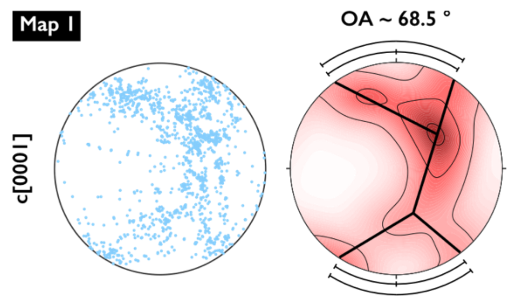

Figure 4-11: Quartz opening angle thermometry. Quartz c-axes from veins within the schist mylonite have a cross girdle pattern with an opening angle of 68.5°. Opening angle thermometry suggests the quartz LPO developed at temperatures of ~550-600 °C (Law, 2014).

However, the presence of chemical zoning in nearly all grains other than recrystallized grains found in porphyroclast tails suggests that grain size reduction was not achieved through precipitation of new grains alone. Newly precipitated grains at high grade P-T conditions would be pure hornblende, lacking any chemical zoning, while grain size reduction by dynamic recrystallization preserves the distinct core and rim compositions. Additionally, internal misorientation maps for individual amphibole porphyroclasts demonstrate the development of subgrains via the (010)[001] and (100)[001] easy slip systems (Fig. 4-10c,d). These slip systems appear active in both the plagioclase-matrix and plagioclase-epidote-matrix domains within the metabasalt mylonites, but subgrain development is more extensive in porphyroclasts in the plagioclase-epidote-matrix domain. This suggests that grain size reduction was primarily achieved through dynamic recrystallization during dislocation creep. Therefore, both DPC and dislocation creep were active within amphibole, with their relative contributions to bulk deformation varying between microstructural domains. The switch in mechanism may be the result of either a lower viscosity contrast between the epidote-plagioclase matrix and the amphibole resulting in higher flow stresses, or a reduction in the metamorphic reaction facilitating DPC due to the lower fraction of plagioclase.

4.5.1.5 Epidote

Deformation mechanisms of epidote are not well known, but previous studies have interpreted rigid grain rotation (e.g., Brunsmann et al., 2000; Kim et al., 2013), dislocation glide along cleavage planes (e.g., Franz and Liebscher, 2004), and diffusion-accommodated grain boundary sliding within a plagioclase matrix (e.g., Stünitz and Tullis, 2001) as dominant mechanisms. Epidote has a weak LPO (Fig. 4-9b), suggesting dislocations were mobile during deformation, which has been previously recognized in naturally deformed epidote blueschists (Cao et al., 2013; Ha et al., 2018; Kim et al., 2013). However, the misorientation maps (Fig. 4-10b) show minimal subgrain development and the lack of recrystallization microstructures indicates epidote likely behaved as rigid grains.

4.5.2 Shear zone rheology and estimating strength

The strength of a subduction interface downdip of the seismogenic zone is a key control on the overall behavior of the subduction zone. Shear zone strength can be approximated by calculating stress from flow laws based on the interpreted deformation mechanisms from field and microstructural observations. Applying this approach to the LRSZ is challenging because strain was distributed across two lithologies, which were both composites of different phase mixtures. Furthermore, flow laws are experimentally calibrated for a single mineral phase or a specific set of minerals deforming via a single deformation mechanism, and the majority of flow laws describe just a handful of minerals. Flow laws for quartz dislocation creep (Hirth et al., 2001) and diffusion creep (Rutter and Brodie, 2004), plagioclase diffusion creep (Rybacki et al., 2006), and biotite dislocation glide (Kronenberg et al., 1990) are well-calibrated with numerous experiments and commonly applied. Amphibolite flow laws are calibrated by for synthetic aggregates of hornblende and plagioclase (Getsinger, 2015; Hacker and Christie, 1990) whose mineralogy and phase abundances closely match our metabasalts. But flow laws for monophase amphibole or epidote, DPC, or polymineralic grain boundary sliding (GBS) are not developed. The presence of water and the water fugacity can significantly weaken dislocation and diffusion creep, but the effect of water fugacity is only included in the quartz dislocation creep and plagioclase diffusion creep flow laws. Additionally, laboratory-derived flow laws are constructed for strain rates of 10^{-4} to 10^{-7} s^{-1} and must be extrapolated to geological strain rates (10^{-12} to 10^{-15} s^{-1}), introducing another degree of uncertainty. We therefore take flow stress estimates from flow laws to be representative within an order of magnitude.

To constrain the overall strength of the shear zone, we assessed the strengths of the major constituent mineral phases with available flow laws for the deformation conditions of the LRSZ (Fig. 4-12). The bulk strain rate accommodated by the shear zone was approximated as 10^{-12} s^{-1} based on the ~600 m width and the convergence rate of ~40 mm/year at the Cascadia subduction zone, which is a typical strain rate for plate boundary shear zones (Fagereng and Biggs, 2019). Strain rate may have varied within the shear zone among the different lithologies and compositional layers due to changes in rheology or development of stress heterogeneities, but the distribution of strain across both the schist mylonite and metabasalt mylonite at the same peak temperature suggests the schist and metabasalt had similar strengths. This inference is supported by Figure 4-12, which shows that, with the exception of quartz diffusion creep and amphibole diffusion creep, the deformation mechanisms that we identified in the mylonites could all have accommodated strain at 10^{-12} s^{-1} at stresses of ~5-30 MPa predicted by geodynamic models and seismic data. Quartz veins provide an additional constraint. Boudinage of quartz veins in both

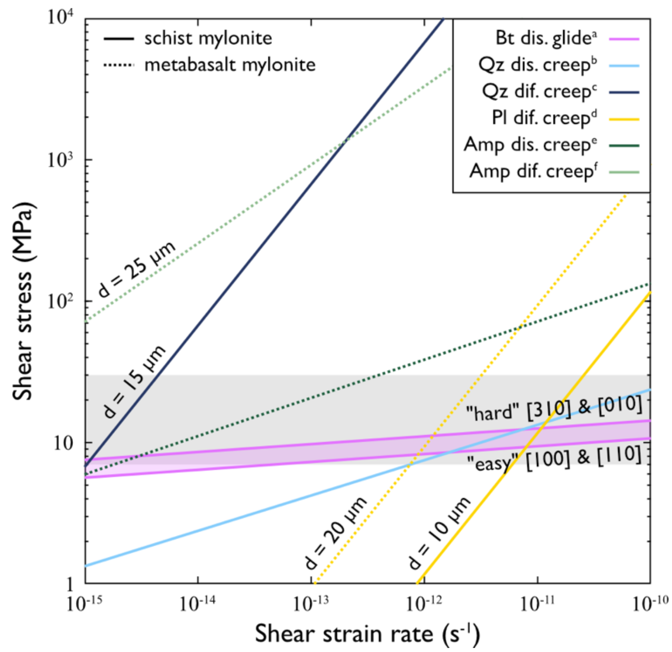

Figure 4-12: Strength estimates from flow laws. Flow laws for dominant phases in the schist and metabasalt mylonites calculated for the deformation P-T of 575 °C and 800 MPa (Chapter 3), a water fugacity of 663 MPa estimated from Tony Withers' water fugacity calculator (https://www.esci.umn.edu/people/researchers/withe012/fugacity.htm), quartz grain size of 15 µm, plagioclase grain sizes of 10 and 20 µm for the schist and metabasalt, respectively, and amphibolite grain size of 25 µm. Note that the water fugacity estimate is a thermodynamic calculation for pure water at the pressure and temperature of deformation. Grey box represents the stress predicted by geodynamic models and seismic data. [a]Dry, single-crystal biotite dislocation glide—Kronenberg et al. (1990). [b]Wet quartz dislocation creep—Hirth et al. (2001). [c]Wet quartz diffusion creep—Rutter and Brodie (2004). [d]Wet plagioclase diffusion creep—Rybacki et al. (2006). [e]Dry amphibolite (~53% hornblende and ~43% plagioclase) dislocation creep—Hacker and Christie (1990). [f]Wet amphibolite (~40-65% hornblende and ~20-40% plagioclase) composite dislocation-diffusion creep—Getsinger (2015).

lithologies, which deformed via dislocation creep, indicates they were strong relative to the polymineralic matrix. Quartz dislocation creep therefore provides an upper bound on the shear strength of the mylonites. The flow stress for quartz dislocation creep at the deformation conditions of the LRSZ is ~7 MPa (Fig. 4-12; Hirth et al., 2001), suggesting an overall weak shear zone.

The rheology of the LRSZ was more complex than this first order estimate, however, as microstructures in the schist and metabasalt mylonites indicate that strain was accommodated by multiple deformation mechanisms operating in different combinations within the varying compositional layers. The bulk strength of the schist mylonite matrix was a function of the deformation in quartz ribbons, polymineralic layers, and phyllosilicate-rich layers. Similar to the quartz veins, dislocation creep active in the boudinaged quartz ribbons accommodated deformation at flow stresses of ~7 MPa. The dominance of diffusive and grain boundary sliding textures and absence of LPO in matrix phases suggest the polymineralic layers likely deformed by grain-size sensitive creep, which is predicted to be significantly weaker (~1 MPa) than dislocation creep in sufficiently fine-grained material (e.g., Ashby and Verrall, 1973). We suggest deformation of the fine-grained, polymineralic layers of quartz, plagioclase, and phyllosilicates was likely accommodated by grain-size sensitive granular flow, a group of diffusion-accommodated mechanisms that includes diffusion- and dislocation-accommodated grain boundary sliding, dissolution-precipitation creep, and pressure solution (Paterson, 1995). Without a constitutive equation for granular flow in quartz-plagioclase-phyllosilicate mixtures, diffusion creep in plagioclase is the nearest approximation, predicting flow stresses as low as 1 MPa (Fig. 12; Rybacki et al., 2006). Boudinage of the polymineralic layers when surrounded by phyllosilicate-rich layers suggests that the phyllosilicate-rich layers were weaker than the polymineralic layers. This is in conflict with predicted flow stresses of ~8 MPa accommodated by dislocation glide in phyllosilicates (Fig. 12; Kronenberg et al., 1990) because microstructures indicate that phyllosilicate-rich layers are weaker than quartz veins. This discrepancy could be due to the construction of the biotite flow law from dry, single crystal experiments, which may not apply to the wet, polycrystalline phyllosilicate layers from the LRSZ. Additionally, the rheological effects

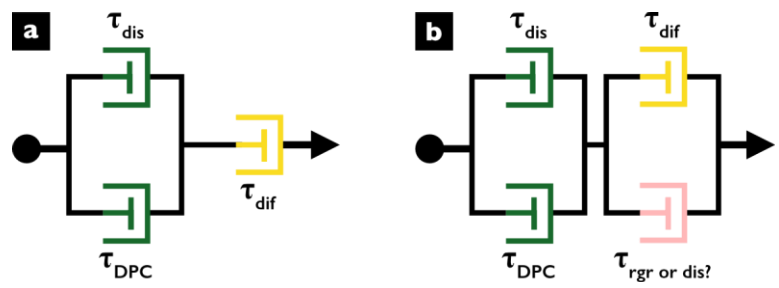

Figure 4-13: Rheological model for metabasalt mylonite. Rheological models constructed for the **(a)** plagioclase matrix domain and **(b)** plagioclase-epidote matrix domain in the metabasalt mylonite based on interpreted deformation mechanisms and microstructural relationships. Deformation proceeds via dislocation creep and DPC in amphibole (green), diffusion creep in plagioclase (yellow), and either rigid grain rotation or a dislocation-based mechanism in epidote (pink).

of possible recovery mechanisms responsible for the reduction in grain size are unknown. These observations indicate that grain-size sensitive creep of polymineralic layers coupled with glide along phyllosilicate basal planes likely deformed at stresses between ~1-7 MPa and were weaker than the quartz veins.

The strength of the metabasalt mylonite matrix was controlled by a combination of DPC and dislocation creep in amphibole and diffusion creep in the fine-grained plagioclase matrix, while the contribution of epidote deformation was minor. Significant deformation of amphibole porphyroclasts suggests a relatively low strength contrast between the porphyroclasts and the matrix as well as a low degree of strain localization (e.g., Handy, 1994; Holyoke and Tullis, 2006). The relative contribution of DPC and dislocation creep in amphibole deformation correlates with the matrix mineralogy. Where amphibole is surrounded by plagioclase (Fig. 4-7a,c), DPC textures dominate and the microstructure is characterized by chemically zoned amphibole porphyroclasts with asymmetric tails and truncated zoning patterns. Where the matrix is composed of epidote as well as plagioclase (Fig. 4-7b,d), amphibole demonstrates a higher degree of recrystallization, indicating that the relative contribution of dislocation creep is higher. Greater dynamic recrystallization in amphibole likely resulted from higher stresses produced by monomineralic layers of amphibole or the even lower strength contrast between amphibole and the epidote-plagioclase matrix due to the rigidity of epidote. Alternatively, the chemical gradients enhancing dissolution of amphibole may have been reduced within the epidote-plagioclase domain relative to the plagioclase domain.

These observations lead to two conceptual models for deformation in the plagioclase and plagioclase-epidote matrix domains (Fig. 4-13). Rheological components in series deform at the same stress, while components in parallel deform at the same strain rate. Amphibole DPC and dislocation creep are shown in parallel, indicating that amphibole deformation will be rate-limited by whichever mechanism is slower. For the plagioclase matrix, plagioclase diffusion creep is in series with amphibole deformation (Fig. 4-13a), indicating that both phases deform at the same stress, producing different strain rates and allowing strain to localize into plagioclase ribbons. For the plagioclase-epidote matrix, epidote is added in parallel with plagioclase (Fig. 4-13b), indicating that epidote limits the strain rate in the matrix and may translate stress to amphibole, contributing to its greater degree of dynamic recrystallization.

At 10^{-12} s^{-1}, dislocation creep of amphibolite, the closest approximation to amphibole dislocation creep, has a flow stress of ~50 MPa (Fig. 12; Hacker and Christie, 1990) and plagioclase diffusion creep has a flow stress of ~10 MPa (Fig. 12; Rybacki et al., 2006). The amphibolite flow law was produced from dry experiments without calibrating for the weakening effect of water fugacity and may therefore overestimate strength. For the matrix to flow at stresses lower than quartz dislocation creep, either DPC and dislocation creep in amphibole must deform at a lower stress, or the metabasalt may have accommodated deformation at slower strain rates. Wassmann and Stöckhert (2013) argue that DPC proceeds at lower stresses than dislocation creep, even at high strain rates, based on the lack of intracrystalline deformation indicators. Additionally, plagioclase diffusion creep supports much lower stresses than quartz dislocation creep at strain rates below 10^{-12} s^{-1}. Ultimately, the presence of water in both units and amphibole-forming hydration reactions in the basalt likely weakened the shear zone through the dominance of diffusion-accommodated deformation mechanisms to produce a very low overall strength (~1-10 MPa) at depths below the seismogenic zone. Low shear stresses in amphibolite-grade metabasalts from the Nishisonogi metamorphic rocks in Japan were also reported by Tulley et al. (2020). Those authors report boudinage of quartz veins within the metabasalts, and stress estimates of ~10-30 MPa from quartz paleopiezometry place an upper limit on the strength of the analyzed metabasalts. However, this weakness of the metabasalt matrix was attributed to slip on networks of muscovite and chlorite, rather than viscous deformation of amphibole. Our results emphasize that hydration of basalt and formation of an assemblage dominated by amphibole and plagioclase during prograde deformation weakens the rocks, to the extent that they have comparable strength to phyllosilicate-rich schists at high temperatures.

Overall, our results imply that the LRSZ, which was active at conditions comparable to the Cascadia subduction zone downdip of the seismogenic zone, was weak. For example, flow stresses of 1-10 MPa are ~0.1-1% of the lithostatic stress at the depth of deformation (~30 km). The LRSZ, was a hot subduction interface due to the regional tectonic context (Chapter 3) and represents an

139

endmember in the range of subduction thermal structures. Deeply exhumed subduction interfaces are scarce and variably overprinted during exhumation and retrogression, but most studies note the importance of diffusion-accommodated deformation processes like pressure solution and DPC supporting low shear stresses (e.g., Angiboust et al., 2011; Behr and Platt, 2013; Stöckhert, 2002; Tulley et al., 2020; Wassmann and Stöckhert, 2012, 2013). Geological evidence therefore supports geodynamic expectations for weak subduction interfaces downdip of the seismogenic zone.

4.6 Conclusions

The schist and metabasalt mylonites of the LRSZ were deformed along the subduction interface below the seismogenic zone. Field relationships and microstructural observations indicate that deformation was accommodated by multiple grain-scale mechanisms operating in different combinations dictated by the mineralogy of compositional layers. The schist mylonite deformed through dislocation creep in quartz ribbons, grain-size sensitive creep in polymineralic quartz-plagioclase-phyllosilicate layers, and dislocation glide with an unknown recovery mechanism in phyllosilicate-rich layers. In the metabasalt mylonite, amphibole deformed by a combination of DPC and dislocation creep, plagioclase deformed via diffusion creep, and epidote likely behaved as rigid grains. Amphibole microstructures within plagioclase matrix and plagioclase-epidote matrix domains are dominated by DPC and dynamic recrystallization via dislocation creep, respectively, indicating that the matrix mineralogy influenced the dominant deformation mechanism. Boudinage of quartz veins in both lithologies deformed via dislocation creep provides an upper bound to the shear zone strength. Deformation mechanisms in the schist and metabasalt mylonites indicate deformation proceeded at low shear stresses of ~1-10 MPa, consistent with geophysical constraints from heat flow and seismic data.

4.7 References

Allison, I., La Tour, T.E., 1977. Brittle deformation of hornblende in a mylonite: a direct geometrical analogue of ductile deformation by translation gliding. Can. J. Earth Sci. 14, 1953-1958. https://doi.org/10.1139/e77-166.

Angiboust, S., Agard, P., Raimbourg, H., Yamato, P., Huet, B., 2011. Subduction interface processes recorded by eclogite-facies shear zones (Monviso, W. Alps). Lithos 127, 222-238. https://doi.org/10.1016/j.lithos.2011.09.004.

Ashby, M.F., Verrall, R.A., 1973. Diffusion-accommodated flow and superplasticity. Acta Materialia 21, 149-163. https://doi.org/10.1016/0001-6160(73)90057-6.

Auzende, A.-L., Escartín, J., Walte, N.P., Guillot, S., Hirth, G., Frost, D.J., 2015. Deformation mechanisms of antigorite serpentinite at subduction zone conditions determined from experimentally and naturally deformed rocks. Earth Planet. Sci. Lett. 411, 229-240. https://doi.org/10.1016/j.epsl.2014.11.053.

Babaie, H.A., La Tour, T.E., 1994. Semibrittle and cataclastic deformation of hornblende-quartz rocks in a ductile shear zone. Tectonophysics 229, 19-30. https://doi.org/10.1016/0040-1951(94)90003-5.

Bachmann, F., Hielscher, R., Schaeben, H., 2010. Texture analysis with MTEX—free and open source software toolbox, Solid State Phenomena. Trans Tech Publications, pp. 63-68.

Behr, W.M., Becker, T.W., 2018. Sediment control on subduction plate speeds. Earth Planet. Sci. Lett. 502, 166-173. https://doi.org/10.1016/j.epsl.2018.08.057.

Behr, W.M., Platt, J.P., 2013. Rheological evolution of a Mediterranean subduction complex. J. Struct. Geol. 54, 136-155. https://doi.org/10.1016/j.jsg.2013.07.012.

Behrmann, J.H., 1984. A study of white mica microstructure and microchemistry in a low grade mylonite. J. Struct. Geol. 6, 283-292. https://doi.org/10.1016/0191-8141(84)90052-X.

Bell, I.A., Wilson, C.J.L., 1981. Deformation of biotite and muscovite: TEM microstructure and deformation model. Tectonophysics 78, 201-228. https://doi.org/10.1016/0040-1951(81)90014-7.

Bell, I.A., Wilson, C.J.L., McLaren, A.C., Etheridge, M.A., 1986. Kinks in mica: Role of dislocations and (001) cleavage. Tectonophysics 127, 49-65. https://doi.org/10.1016/0040-1951(86)90078-8.

Berger, A., Stünitz, H., 1996. Deformation mechanisms and reaction of hornblende: examples from the Bergell tonalite (Central Alps). Tectonophysics 257, 149-174. https://doi.org/10.1016/0040-1951(95)00125-5.

Bestmann, M., Pennacchioni, G., Frank, G., Göken, M., de Wall, H., 2011. Pseudotachylyte in muscovite-bearing quartzite: Coseismic friction-induced melting and plastic deformation of quartz. J. Struct. Geol. 33, 169-186. https://doi.org/10.1016/j.jsg.2010.10.009.

Bletery, Q., Thomas, A.M., Rempel, A.W., Hardebeck, J., 2017. Imaging shear strength along subduction faults. Geophys. Res. Lett. 44, 11329-11339. https://doi.org/10.1002/2017GL075501.

Bons, A.-J., 1988. Deformation of chlorite in naturally deformed low-grade rocks. Tectonophysics 154, 149-165. https://doi.org/10.1016/0040-1951(88)90232-6.

Borg, I., Handin, J.W., 1966. Experimental deformation of crystalline rocks. Tectonophysics 3, 249-367. https://doi.org/10.1016/0040-1951(66)90019-9.

Brunsmann, A., Franz, G., Erzinger, J., Landwehr, D., 2000. Zoisite- and clinozoisite-segregations in metabasites (Tauern Window, Austria) as evidence for high-pressure fluid–rock interaction. J. metamorphic Geol. 18, 1-21. https://doi.org/10.1046/j.1525-1314.2000.00233.x.

Bunge, H., 1982. Texture Analysis in Materials Science: Mathematical Models. Butterworth, London.

Cao, S., Liu, J., Leiss, B., 2010. Orientation-related deformation mechanisms of naturally deformed amphibole in amphibolite mylonites from the Diancang Shan, SW Yunnan, China. J. Struct. Geol. 32, 606-622. https://doi.org/10.1016/j.jsg.2010.03.012.

Cao, Y., Jung, H., Song, S., 2013. Petro-fabrics and seismic properties of blueschist and eclogite in the North Qilian suture zone, NW China: Implications for the low-velocity upper layer in subducting slab, trench-parallel seismic anisotropy, and eclogite detectability in the subduction zone. J. Geophys. Res. Solid Earth 118, 3037-3058. https://doi.org/10.1002/jgrb.50212.

Christoffersen, R., Kronenberg, A.K., 1993. Dislocation interactions in experimenatlly deformed biotite. J. Struct. Geol. 15, 1077-1095. https://doi.org/10.1016/0191-8141(93)90157-6.

Clowes, R.M., Brandon, M.T., Green, A.G., Yorath, C.J., Brown, A.S., Kanasewich, E.R., Spencer, C., 1987. LITHOPROBE--southern Vancouver Island: Cenozoic subduction complex imaged by deep seismic reflections. Can. J. Earth Sci. 24, 31-51. https://doi.org/10.1139/e87-004.

Condit, C.B., Mahan, K.H., 2018. Fracturing, fluid flow and shear zone development: Relationships between chemical and mechanical processes in Proterozoic mafic dykes from southwestern Montana, USA. J. metamorphic Geol. 36, 195-223. https://doi.org/10.1111/jmg.12289.

Cui, Y., Miller, D., Schiarizza, P., Diakow, L.J., 2017. British Columbia digital geology. British Columbia Ministry of Energy, Mines and Petroleum Resources, British Columbia Geological Survey Open File 2017-8, Data version 2019-12-19.

Cumbest, R.J., Drury, M.R., van Roermund, H.L.M., Simpson, C., 1989. Dynamic recrystallization and chemical evolution of clinoamphibole from Senja, Norway. Contrib. Mineral. Petrol. 101, 339-349. https://doi.org/10.1007/BF00375318.

Dempsey, E.D., Prior, D.J., Mariani, E., Toy, V.G., Tatham, D.J., 2011. Mica-controlled anisotropy within mid-to-upper crustal mylonites: an EBSD study of mica fabrics in the Alpine Fault Zone, New Zealand. Geol. Soc. Spec. Publ. 360, 33-47. https://doi.org/10.1144/SP360.3.

Díaz Aspiroz, M., Lloyd, G.E., Fernández, C., 2007. Development of lattice preferred orientation in clinoamphiboles deformed under low-pressure metamorphic conditions. A SEM/EBSD study of metabasites from the Aracena metamorphic belt (SW Spain). J. Struct. Geol. 29, 629-645. https://doi.org/10.1016/j.jsg.2006.10.010.

Dollinger, G., Blacic, J.D., 1975. Deformation mechanisms in experimentally and naturally deformed amphiboles. Earth Planet. Sci. Lett. 26, 409-416. https://doi.org/10.1016/0012-821X(75)90016-3.

Duarte, J.C., Schellart, W.P., Cruden, A.R., 2015. How weak is the subduction zone interface? Geophys. Res. Lett. 42, 2664-2673. https://doi.org/10.1002/2014GL062876.

Elyaszadeh, R., Prior, D.J., Sarkarinejad, K., Mansouri, H., 2018. Different slip systems controlling crystallographic preferred orientation and intracrystalline deformation of amphibole in mylonites from the Neyriz mantle diapir, Iran. J. Struct. Geol. 107, 38-52. https://doi.org/10.1016/j.jsg.2017.11.020.

Etheridge, M.A., Wilkie, J.C., 1979. Grainsize reduction, grain boundary sliding and the flow strength of mylonites. Tectonophysics 58, 159-178. https://doi.org/10.1016/0040-1951(79)90327-5.

Fagereng, Å., Biggs, J., 2019. New perspectives on 'geological strain rates' calculated from both naturally deformed and actively deforming rocks. J. Struct. Geol. 125, 100-110. https://doi.org/10.1016/j.jsg.2018.10.004.

Fagereng, Å., den Hartog, S.A.M., 2016. Subduction megathrust creep governed by pressure solution and frictional–viscous flow. Nat. Geosci. 10, 51-57. https://doi.org/10.1038/ngeo2857.

Fairchild, L.H., Cowan, D.S., 1982. Structure, petrology, and tectonic history of the Leech River complex northwest of Victoria, Vancouver Island. Can. J. Earth Sci. 19, 1817-1835. https://doi.org/10.1139/e82-161.

Fliervoet, T.F., White, S.H., Drury, M.R., 1997. Evidence for dominant grain-boundary sliding deformation in greenschist- and amphibolite-grade polymineralic ultramylonites from the Redbank Deformed Zone, Central Australia. J. Struct. Geol. 19, 1495-1520. https://doi.org/10.1016/S0191-8141(97)00076-X.

Franz, G., Liebscher, A., 2004. Physical and chemical properties of the epidote minerals—An introduction. Reviews in Mineralogy and Geochemistry 56, 1-81. https://doi.org/10.2138/gsrmg.56.1.1.

Fukuda, J., Holyoke, C.W., III, Kronenberg, A.K., 2018. Deformation of fine-grained quartz aggregates by mixed diffusion and dislocation creep. J. Geophys. Res. Solid Earth 123, 4676-4696. https://doi.org/10.1029/2017JB015133.

Gao, X., Wang, K., 2014. Strength of stick-slip and creeping subduction megathrusts from heat flow observations. Science 345, 1038-1041. https://doi.org/10.1126/science.1255487.

Gerbi, C., Johnson, S.E., Cook, A., Vel, S.S., 2015. Effect of phase morphology on bulk strength for power-law materials. Geophys. J. Int. 200, 374-389.

Gerya, T.V., Connolly, J.A.D., Yuen, D.A., 2008. Why is terrestrial subduction one-sided? Geology 36, 43-46. https://doi.org/10.1130/G24060A.1.

Getsinger, A.J., 2015. The Rheology of Amphibolite, Geological Sciences. Brown University, Providence, RI, p. 170.

Getsinger, A.J., Hirth, G., 2014. Amphibole fabric formation during diffusion creep and the rheology of shear zones. Geology 42, 535-538. https://doi.org/10.1130/G35327.1.

Getsinger, A.J., Hirth, G., Stünitz, H., Goergen, E.T., 2013. Influence of water on rheology and strain localization in the lower continental crust. Geochem. Geophys. Geosyst. 14, 2247-2264. https://doi.org/10.1002/ggge.20148.

Goodwin, L.B., Wenk, H.-R., 1990. Intracrystalline folding and cataclasis in biotite of the Santa Rosa mylonite zone: HVEM and TEM observations. Tectonophysics 172, 201-214. https://doi.org/10.1016/0040-1951(90)90030-C.

Gower, R.J.W., Simpson, C., 1992. Phase boundary mobility in naturally deformed, high-grade quartzofeldspathic rocks: evidence for diffusional creep. J. Struct. Geol. 14, 301-313. https://doi.org/10.1016/0191-8141(92)90088-E.

Groome, W.G., Thorkelson, D.J., Friedman, R.M., Mortensen, J.K., Massey, N.W.D., Marshall, D.D., Layer, P.W., 2003. Magmatic and tectonic history of the Leech River Complex, Vancouver Island, British Columbia: Evidence for ridge-trench intersection and accretion of the Crescent Terrane. Special Papers-Geological Society of America 371, 327-353. https://doi.org/10.1130/0-8137-2371-X.327.

Ha, Y., Jung, H., Raymond, L.A., 2018. Deformation fabrics of glaucophane schists and implications for seismic anisotropy: the importance of lattice preferred orientation of phengite. International Geology Review 61, 720-737. https://doi.org/10.1080/00206814.2018.1449142.

Hacker, B.R., Christie, J.M., 1990. Brittle/ductile and plastic/cataclastic transitions in experimentally deformed and metamorphosed amphibolite, in: Duba, A.G., Durham, W.B., Handin, J.W., Wang, H.F. (Eds.), The Brittle-Ductile Transition in Rocks. Geophysical Monograph Series, pp. 127-147.

Handy, M.R., 1994. Flow laws for rocks containing two non-linear viscous phases: a phenomenological approach. J. Struct. Geol. 16, 287-301. https://doi.org/10.1016/0191-8141(94)90035-3.

Hardebeck, J., 2015. Stress orientations in subduction zones and the strength of subduction megathrust faults. Science 349, 1213-1216. https://doi.org/10.1126/science.aac5625.

Hirth, G., Teyssier, C., Dunlap, W.J., 2001. An evaluation of quartzite flow laws based on comparisons between experimentally and naturally deformed rocks. Int. J. Earth Sci. 90, 77-87. https://doi.org/10.1007/s005310000152.

Hirth, G., Tullis, J., 1992. Dislocation creep regimes in quartz aggregates. J. Struct. Geol. 14, 145-159. https://doi.org/10.1016/0191-8141(92)90053-Y.

Holyoke, C.W., Tullis, J., 2006. Mechanisms of weak phase interconnection and the effects of phase strength contrast on fabric development. J. Struct. Geol. 28, 621-640. https://doi.org/10.1016/j.jsg.2006.01.008.

Hunter, N.J.R., Hasalová, P., Weinberg, R.F., Wilson, C.J.L., 2016. Fabric controls on strain accommodation in naturally deformed mylonites: The influence of interconnected micaceous layers. J. Struct. Geol. 83, 180-193. https://doi.org/10.1016/j.jsg.2015.12.005.

Hyndman, R.D., 2013. Downdip landward limit of Cascadia great earthquake rupture. J. Geophys. Res. Solid Earth 118, 5530-5549. https://doi.org/10.1002/jgrb.50390.

Hyndman, R.D., Wang, K., 1993. Thermal constraints on the zone of major thrust earthquake failure: The Cascadia Subduction Zone. J. Geophys. Res. Solid Earth 98, 2039-2060. https://doi.org/10.1029/92JB02279.

Hyndman, R.D., Yorath, C.J., Clowes, R.M., Davis, E.E., 1990. The northern Cascadia subduction zone at Vancouver Island: seismic structure and tectonic history. Can. J. Earth Sci. 27, 313-329. https://doi.org/10.1139/e90-030.

Imon, R., Okudaira, T., Fujimoto, A., 2002. Dissolution and precipitation processes in deformed amphibolites: An example from the ductile shear zone of the Ryoke metamorphic belt, SW Japan. J. metamorphic Geol. 20, 297-308. https://doi.org/10.1046/j.1525-1314.2002.00367.x.

Imon, R., Okudaira, T., Kanagawa, K., 2004. Development of shape- and lattice-preferred orientations of amphibole grains during initial cataclastic deformation and subsequent deformation by dissolution-precipitation creep in amphibolites from the Ryoke metamorphic belt, SW Japan. J. Struct. Geol. 26, 793-805. https://doi.org/10.1016/j.jsg.2003.09.004.

Inoue, S., Kogure, T., 2012. Electron backscatter diffraction (EBSD) analyses of phyllosilicates in petrographic thin sections. Am. Min 97, 755-758. https://doi.org/10.2138/am.2012.4061.

Jessell, M.W., 1987. Grain-boundary migration microstructures in a naturally deformed quartzite. J. Struct. Geol. 9, 1007-1014. https://doi.org/10.1016/0191-8141(87)90008-3.

Kim, D., Katayama, I., Michibayashi, K., Tsujimori, T., 2013. Deformation fabrics of natural blueschists and implications for seismic anisotropy in subducting oceanic crust. Phys. Earth Planet. Inter. 222, 8-21. https://doi.org/10.1016/j.pepi.2013.06.011.

Kohlstedt, D.L., Evans, B., Mackwell, S.J., 1995. Strength of the lithosphere: Constraints imposed by laboratory experiments. J. Geophys. Res. Solid Earth 100, 17587-17602. https://doi.org/10.1029/95JB01460.

Kronenberg, A.K., Kirby, S.H., Pinkston, 1990. Basal slip and mechanical anisotropy of biotite. J. Geophys. Res. Solid Earth 95, 19257-19278. https://doi.org/10.1029/JB095iB12p19257.

Kruse, R., Stünitz, H., 1999. Deformation mechanisms and phase distribution in mafic high-temperature mylonites from the Jotun Nappe, southern Norway. Tectonophysics 303, 223-249. https://doi.org/10.1016/S0040-1951(98)00255-8.

Law, R.D., 2014. Deformation thermometry based on quartz c-axis fabrics and recrystallization microstructures: A review. J. Struct. Geol. 66, 129-161. https://doi.org/10.1016/j.jsg.2014.05.023.

Mares, V.M., Kronenberg, A.K., 1993. Experimental deformation of muscovite. J. Struct. Geol. 15, 1061-1075. https://doi.org/10.1016/0191-8141(93)90156-5.

Mariani, E., Brodie, K.H., Rutter, E.H., 2006. Experimental deformation of muscovite shear zones at high temperatures under hydrothermal conditions and the strength of phyllosilicate-bearing faults in nature. J. Struct. Geol. 28, 1569-1587. http://doi.org/10.1016/j.jsg.2006.06.009.

Marti, S., Stünitz, H., Heilbronner, R., Plümper, O., Kilian, R., 2018. Syn-kinematic hydration reactions, grain size reduction, and dissolution-precipitation creep in experimentally deformed plagioclase-pyroxene mixtures. Solid Earth 9, 985-1009. https://doi.org/10.5194/se-9-985-2018.

Massey, N.W.D., 1986. Metchosin Igneous Complex, southern Vancouver Island: Ophiolite stratigraphy developed in an emergent island setting. Geology 14, 602-605. https://doi.org/10.1130/0091-7613(1986)14%3C602:MICSVI%3E2.0.CO;2.

Mehl, L., Hirth, G., 2008. Plagioclase preferred orientation in layered mylonites: Evaluation of flow laws for the lower crust. J. Geophys. Res. Solid Earth 113, B05202. https://doi.org/10.1029/2007JB005075.

Meike, A., 1989. In situ deformation of micas: A high-voltage electron-microscope study. Am. Min 74, 780-796.

Miranda, Elena A., Hirth, G., John, B.E., 2016. Microstructural evidence for the transition from dislocation creep to dislocation-accommodated grain boundary sliding in naturally deformed plagioclase. J. Struct. Geol. 92, 30-45. https://doi.org/10.1016/j.jsg.2016.09.002.

Misra, S., Burg, J.-P., 2012. Mechanics of kink-bands during torsion deformation of muscovite aggregate. Tectonophysics 548-549, 22-33. https://doi.org/10.1016/j.tecto.2012.04.014.

Muller, J.E., 1980. Geology, Victoria, British Columbia. Geological Survey of Canada, Open File 701. https://doi.org/10.4095/129114.

Naus-Thijssen, F.M.J., Goupee, A.J., Johnson, S.E., Vel, S.S., Gerbi, C., 2011. The influence of crenulation cleavage development on the bulk elastic and seismic properties of phyllosilicate-rich rocks. Earth Planet. Sci. Lett. 311, 212-224. https://doi.org/10.1016/j.epsl.2011.08.048.

Niemeijer, A.R., Spiers, C.J., 2005. Influence of phyllosilicates on fault strength in the brittle-ductile transition: Insights from rock analogue experiments. Geol. Soc. Spec. Publ. 245, 303-327. https://doi.org/10.1144/GSL.SP.2005.245.01.15.

Nyman, M.W., Law, R.D., Smelik, E.A., 1992. Cataclastic deformation mechanism for the development of core-mantle structures in amphibole. Geology 20, 455-458. https://doi.org/10.1130/0091-7613(1992)020<0455:CDMFTD>2.3.CO;2.

Okamoto, A.S., Verberne, B.A., Niemeijer, A., Takahashi, M., Shimizu, I., Ueda, T., Spiers, C.J., 2019. Frictional properties of simulated chlorite gouge at hydrothermal conditions: Implications for subduction megathrusts. J. Geophys. Res. Solid Earth 124, 4545-4565. https://doi.org/10.1029/2018JB017205.

Oleskevich, D.A., Hyndman, R.D., Wang, K., 1999. The updip and downdip limits to great subduction earthquakes: Thermal and structural models of Cascadia, south Alaska, SW Japan, and Chile. J. Geophys. Res. Solid Earth 104, 14965-14991. https://doi.org/10.1029/1999JB900060.

Padrón-Navarta, J.A., Tommasi, A., Garrido, C.J., Sánchez-Vizcaíno, V.L., 2012. Plastic deformation and development of antigorite crystal preferred orientation in high-pressure serpentinites. Earth Planet. Sci. Lett. 349-350, 75-86. https://doi.org/10.1016/j.epsl.2012.06.049.

Passchier, C.W., Trouw, R.A.J., 2005. Microtectonics, 2 ed. Springer, Berlin.

Paterson, M.S., 1995. A theory for granular flow accommodated by material transfer via an intergranular fluid. Tectonophysics 245, 135-151. https://doi.org/10.1016/0040-1951(94)00231-W.

Peacock, S.M., 2009. Thermal and metamorphic environment of subduction zone episodic tremor and slip. J. Geophys. Res. Solid Earth 114, B00A07. https://doi.org/10.1029/2008JB005978.

Peng, Z., Gomberg, J., 2010. An integrated perspective of the continuum between earthquakes and slow-slip phenomena. Nat. Geosci. 3, 599-607. https://doi.org/10.1038/ngeo940.

Phillips, B.A., Kerr, A.C., Mullen, E.K., Weis, D., 2017. Oceanic mafic magmatism in the Siletz terrane, NW North America: Fragments of an Eocene oceanic plateau? Lithos 274-275, 291-303. https://doi.org/10.1016/j.lithos.2017.01.005.

Platt, J.P., 2015. Rheology of two-phase systems: A microphysical and observational approach. J. Struct. Geol. 77, 213-227. https://doi.org/10.1016/j.jsg.2015.05.003.

Platt, J.P., Xia, H., Schmidt, W.L., 2018. Rheology and stress in subduction zones around the aseismic/seismic transition. Progress in Earth and Planetary Science 5, 24. https://doi.org/10.1186/s40645-018-0183-8.

Prior, D.J., Mariani, E., Wheeler, J., 2009. EBSD in the Earth Sciences: Applications, Common Practice, and Challenges, in: Schwartz, A.J., Kumar, M., Adams, B.L., Field, D.P. (Eds.), Electron Backscatter Diffraction in Materials Science, 2 ed. Springer Sc, pp. 345-360.

Rasband, W.S., 1997-2018. ImageJ. U.S. National Institutes of Health, Bethesda, MD, p. http://imagej.nih.gov/ij/.

Richardson, R.M., Coblentz, D.D., 1994. Stress modelling in the Andes: Constraints on the South American intraplate stress magnitudes. J. Geophys. Res. Solid Earth 99, 22015-22025. https://doi.org/10.1029/94JB01751.

Rusmore, M.E., 1982. Structure and petrology of pre-tertiary rocks near Port Renfrew, Vancouver Island, British Columbia. University of Washington.

Rutter, E.H., Brodie, K.H., 2004. Experimental grain size-sensitive flow of hot-pressed Brazilian quartz aggregates. J. Struct. Geol. 26, 2011-2023. https://doi.org/10.1016/j.jsg.2004.04.006.

Rybacki, E., Dresen, G., 2004. Deformation mechanism maps for feldspar rocks. Tectonophysics 382, 173-187. https://doi.org/10.1016/j.tecto.2004.01.006.

Rybacki, E., Gottschalk, M., Wirth, R., Dresen, G., 2006. Influence of water fugacity and activation volume on the flow properties of fine-grained anorthite aggregates. J. Geophys. Res. Solid Earth 111, B03203. http://doi.org/10.1029/2005JB003663.

Schmid, S.M., Casey, M., 1986. Complete fabric analysis of some commonly observed quartz c-axis patterns, in: Hobbs, B.E., Heard, H. (Eds.), Mineral and Rock Deformation: Laboratory Studies. Geophysical Monograph Series, pp. 263-286.

Shea, W.T., Kronenberg, A.K., 1993. Strength and anisotropy of foliated rocks with varied mica contents. J. Struct. Geol. 15, 1097-1121. http://doi.org/10.1016/0191-8141(93)90158-7.

Skemer, P., Katayama, I., Jiang, Z., Karato, S.-i., 2005. The misorientation index: Development of a new method for calculating the strength of lattice-preferred orientation. Tectonophysics 411, 157-167. https://doi.org/10.1016/j.tecto.2005.08.023.

Song, W.J., Ree, J.-H., 2007. Effect of mica on the grain size of dynamically recrystallized quartz in a quartz–muscovite mylonite. J. Struct. Geol. 29, 1872-1881. https://doi.org/10.1016/j.jsg.2007.09.011.

Soret, M., Agard, P., Ildefonse, B., Dubacq, B., Prigent, C., 2019. Deformation mechanisms in mafic amphibolites and granulites: record from the Semail metamorphic sole during subduction infancy. Solid Earth 10, 1733-1755. https://doi.org/10.5194/se-10-1733-2019.

Stipp, M., Stünitz, H., Heilbronner, R., Schmid, S.M., 2002. The eastern Tonale fault zone: A 'natural laboratory' for crystal plastic deformation of quartz over a temperature range from 250 to 700 ˚C. J. Struct. Geol. 24, 1861-1884. https://doi.org/10.1016/S0191-8141(02)00035-4.

Stöckhert, B., 2002. Stress and deformation in subduction zones: insight from the record of exhumed metamorphic rocks. Geol. Soc. Spec. Publ. 200, 255-274. https://doi.org/10.1144/GSL.SP.2001.200.01.15.

Stokes, M.R., Wintsch, R.P., Southworth, C.S., 2012. Deformation of amphibolites via dissolution–precipitation creep in the middle and lower crust. J. metamorphic Geol. 30, 723-737. https://doi.org/10.1111/j.1525-1314.2012.00989.x.

Stünitz, H., Tullis, J., 2001. Weakening and strain localization produced by syn-deformational reaction of plagioclase. Int. J. Earth Sci. 90, 136-148. https://doi.org/10.1007/s005310000148.

Tatham, D.J., Lloyd, G.E., Butler, R.W.H., Casey, M., 2008. Amphibole and lower crustal seismic properties. Earth Planet. Sci. Lett. 267, 118-128. https://doi.org/10.1016/j.epsl.2007.11.042.

Trepmann, C.A., Hsu, C., Hentschel, F., Döhler, K., Schneider, C., Wichmann, V., 2017. Recrystallization of quartz after low-temperature plasticity — The record of stress relaxation below the seismogenic zone. J. Struct. Geol. 95, 77-92. https://doi.org/10.1016/j.jsg.2016.12.004.

Tulley, C.J., Fagereng, Å., Ujiie, K., 2020. Hydrous oceanic crust hosts megathrust creep at low shear stresses. Sci. Adv. 6, eaba1529. https://doi.org/10.1126/sciadv.aba1529.

Tullis, J., Wenk, H.-R., 1994. Effect of muscovite on the strength and lattice preferred orientations of experimentally deformed quartz aggregates. Materials Science and Engineering: A 175, 209-220. https://doi.org/10.1016/0921-5093(94)91060-X.

Tullis, T., Horowitz, F.G., Tullis, J., 1991. Flow laws of polyphase aggregates from end-member flow laws. J. Geophys. Res. Solid Earth 96, 8081-8096. https://doi.org/10.1029/90JB02491.

Vernon, R.H., 1977. Microfabric of mica aggregates in partly recrystallized biotite. Contrib. Mineral. Petrol. 61, 175-185. https://doi.org/10.1007/BF00374366.

von Herzen, R., Ruppel, C., Molnar, P., Nettles, M., Nagihara, S., Ekström, G., 2001. A constraint on the shear stress at the Pacific-Australian plate boundary from heat flow and seismicity at the Kermadec forearc. J. Geophys. Res. Solid Earth 106, 6817-6833. https://doi.org/10.1029/2000JB900469.

Wallis, D., Lloyd, G.E., Phillips, R.J., Parsons, A.J., Walshaw, R.D., 2015. Low effective fault strength due to frictional-viscous flow in phyllonites, Karakoram Fault Zone, NW India. J. Struct. Geol. 77, 45-61. https://doi.org/10.1016/j.jsg.2015.05.010.

Wang, K., Mulder, T., Rogers, G., Hyndman, R., 1995. Case for very low coupling stress on the Cascadia subduction fault. J. Geophys. Res. 100, 12907-12918. https://doi.org/10.1029/95JB00516.

Wassmann, S., Stöckhert, B., 2012. Matrix deformation mechanisms in HP-LT tectonic mélanges: Microstructural record of jadeite blueschist from the Franciscan Complex, California. Tectonophysics 568-569, 135-153. https://doi.org/10.1016/j.tecto.2012.01.009.

Wassmann, S., Stöckhert, B., 2013. Rheology of the plate interface — Dissolution precipitation creep in high pressure metamorphic rocks. Tectonophysics 608, 1-29. https://doi.org/10.1016/j.tecto.2013.09.030.

Wells, R., Bukry, D., Friedman, R., Pyle, D., Duncan, R., Haeussler, P., Wooden, J., 2014. Geologic history of Siletzia, a large igneous province in the Oregon and Washington Coast Range: Correlation to the geomagnetic polarity time scale and implications for a long-lived Yellowstone hotspot. Geosphere 10, 692-719. https://doi.org/10.1130/GES01018.1.

Wheeler, J., 1992. Importance of pressure solution and Coble creep in the deformation of polymineralic rocks. J. Geophys. Res. 97, 4579-4586. https://doi.org/10.1029/91JB02476.

Wilson, C.J.L., Bell, I.A., 1979. Deformation of biotite and muscovite: Optical microstructure. Tectonophysics 58, 179-200. https://doi.org/10.1016/0040-1951(79)90328-7.

Zhao, N., Hirth, G., Cooper, R.F., Kruckenberg, S.C., Cukjati, J., 2019. Low viscosity of mantle rocks linked to phase boundary sliding. Earth Planet. Sci. Lett. 517, 83-94. https://doi.org/10.1016/j.epsl.2019.04.019.

CHAPTER 5

Future work

Future work for Chapter 2

The likelihood of rupture to the trench at the Cascadia subduction zone may depend on the frictional stability of the sediments along the décollement as well as their fracture energy. These frictional properties may help explain why geodetic models lack an updip zone of aseismic creep, which is common at other subduction margins, and instead interpret the shallow megathrust to be locked to the trench. Additionally, variability in the fracture energy of wet, clay-rich gouges is not well explained by any of the experimental parameters available in our data compilation. New experiments designed to measure the frictional properties of Cascadia sediments at *in situ* conditions will provide better constraints on the mechanical behavior of natural systems. These experiments could include:

- Low velocity experiments at *in situ* temperatures and confining pressures to determine rate-and-state frictional parameters of the ODP core samples to address the stability of the shallow plate interface in northern Cascadia and the degree of locking to the trench
- High velocity experiments with the ability to measure pore pressure to address the spread in mechanical behavior of wet, clay-rich gouges

Future work for Chapter 3

This chapter establishes the LRSZ as a subduction interface, but regional-scale variability and the precise timing of deformation and metamorphism remain largely unknown. Additional work would provide better constraints on tectonic history of terranes in southern Vancouver Island. This work could include:

- Field work, microstructural, and geochemical analysis of along-strike variations in the metamorphism and deformation in the LRSZ to address regional changes in P-T, strain, or tectonic context
- Geochemical analyses of amphibole-plagioclase pairs to constrain the syn-kinematic P-T conditions for the metabasalt mylonites from the LRSZ
- Geochronological analyses on metamorphic porphyroblasts of garnet and, if possible, staurolite and andalusite to determine the age of peak metamorphism and define a P-T-t path for the LRSZ
- Regional-scale detrital zircon geochronology investigation of the Leech River Complex to identify patterns in the MDA to address any internal structure or deformation

Future work for Chapter 4

This chapter identifies the importance of fluids, hydrous minerals, and grain-size sensitive creep in weakening the paleosubduction interface, but further investigation is needed to better understand the mobility of fluids, the role of those fluids in mobilizing quartz along the plate interface, and the strength of polymineralic rocks. Additionally, more experiments are needed to define flow laws for under-studied minerals and deformation mechanisms. These studies could include:

- Microstructural and geochemical analyses to investigate the apparent increase in silica at the lithologic contact to address channelization of pore fluids and fluid flow through the shear zone, fluid-rock interactions, and the weakening effect of small-scale variations in water content within shear zones
- High-temperature creep experiments on hornblende under wet conditions to measure the strength of dislocation creep and develop a flow law

- High-temperature creep experiments on phyllosilicates (i.e., muscovite, chlorite, and/or biotite) to investigate dynamic recrystallization as a possible recovery mechanism
- High-temperature creep experiments on fine-grain mixtures of quartz, plagioclase, and phyllosilicates to activate grain-size sensitive creep, measure the strength of polymineralic aggregates, and develop a flow law

CHAPTER 6

Conclusions

Deformation on the subduction interface above and below the seismogenic zone is traditionally presumed to accommodate stable fault creep while the seismogenic zone accumulates and releases strain through cycles of large earthquakes. The constitutive behavior and strength of these creeping zones is fundamental to understanding subduction dynamics, but primary controls on slip behavior (i.e., lithology, mineralogy, microstructure, etc.) cannot be directly observed with geophysical methods. Instead, experimental deformation of representative materials and investigation of exhumed rocks can estimate the material properties at depth. This thesis, using the Cascadia subduction zone as a case study, contributes to an improved understanding of the constitutive behavior of subduction zones by presenting experimental constraints on the high velocity mechanical properties of the subduction interface updip from the seismogenic zone and field and microstructural constraints on the rheology of the interface downdip.

Updip from the seismogenic zone, earthquake rupture to the surface produces displacement of the seafloor that increases the likelihood of tsunamigenesis. Estimates of fracture energy determined from high velocity rotary shear experiments for the input sediments from Cascadia, a suite of individual clay species, and a compilation of samples from other subduction margins demonstrate the low fracture energy of clay-bearing fault gouge. Fracture energy is particularly low in clay-bearing rocks because they have very low frictional strength, and the impermeability of clay increases the efficacy of dynamic weakening via thermal pressurization. Low fracture energy facilitates earthquake propagation, so subduction faults localized in clay-rich rocks may be susceptible to rupture to the trench. But fracture energy of the Cascadia sediments is nearly an order of magnitude larger than estimates from other subduction zones, likely due to their lower clay content (~35-45%), possibly inhibiting earthquake rupture propagation. These results represent the first experimental investigation into the subduction megathrust frictional properties relevant to seismic slip rates for the Cascadia subduction zone.

Downdip from the seismogenic zone, field, petrological, microstructural, and geochronological data establish that the Leech River Shear Zone (LRSZ) was a dominantly reverse-sense structure. The compositions of syn-kinematic porphyroblasts record growth on a prograde path. These results confirm the LRSZ as a subduction interface exhumed from P-T conditions corresponding to the downdip transition from the seismogenic zone into the creeping zone. The rheology of the shear zone is estimated from dominant deformation mechanisms within the schist and metabasalt mylonites. Microstructural observations demonstrate that deformation required multiple mechanisms operating in different mineral phases, which combined to produce a bulk strength of ~1-10 MPa. This low shear stress is attributed to the weakness of hydrous phases like phyllosilicates and amphibole, the very small grain sizes maintained by phase mixing within the polymineralic rocks, and the operation of diffusion-based mechanisms. The very low shear stress is consistent with the weak plate interface inferred from geophysical data and required by numerical modelling of subduction. Together, these new constraints provide realistic estimates of strength and constitutive behavior of the subduction interface that will better inform modeling of seismic and tsunami hazard and subduction dynamics.

APPENDIX A

Supplementary Materials for Chapter 2

This supplement includes supplementary methods and data for x-ray diffraction analysis, high velocity experiments, and the experimental data compilation.

A1 Supplemental methods for x-ray diffraction analyses

Sample mineralogy and dominant clay species of the selected core samples were characterized using X-ray diffraction (XRD) on whole rock powders and separated clay fractions. These results are presented in Figures S1 and S2, respectively. The core samples were ground into <90 μm powders with an alumina mortar and pestle followed by 4 minutes in the McCrone micronizing mill. Randomly oriented whole rock powders and oriented clay mounts were prepared following the methods set forth by the USGS laboratory manual for XRD (Poppe et al., 2001) to assure meaningful results. Samples were analyzed in a Rigaku SmartLab® high resolution X-ray diffractometer with Cu$K\alpha$ radiation at 40 kV and 30 mA with a 0.5° divergence slit at a continuous scan rate of 1°2θ per minute. Oriented clay mounts were analyzed untreated, expanded with ethylene glycol, and heated to 400 ˚C for clay mineral identification. Spectra collected for the whole rock powders were analyzed with Rigaku PDXL software for phase identification and composition was determined from Rietveld refinement. The uncertainty of the percentages is on the order of 5%.

A2 Supplemental methods for the high velocity friction experimental procedure

Cascadia core sample experiments were conducted in the low to high velocity rotary shear apparatus (“PHV”) at Kochi/JAMSTEC (Tanikawa et al., 2012). The machine consists of an upper stationary side from which normal load is applied and torque is measured, and a lower rotational side which is controlled by a servo motor and rotations are measured. Individual clay species experiments were conducted in the high velocity rotary shear apparatus (“HVR”) at Kochi/JAMSTEC (for more detail see Tsutsumi and Shimamoto (1997)). The machine consists of a stationary side from which normal load is applied and torque is measured, and a rotational side which has a magnetic clutch to engage the sample assembly with the motor once the desired rotation speed has been reached. The normal load is supplied by an air actuator that has the advantage that when the sample shortens during rapid slip, the normal load is maintained due to the high compressibility of air. Sample shortening was measured using a displacement transducer.

Experiments were conducted on the PHV and HVR apparatuses without gouge material, without applied normal stress, and with a gap between the sliding blocks to test the mechanical contribution of Teflon present in the sample assembly. O-rings and a Teflon jacket were components of the PHV sample assembly (Fig. 2-2), and a Teflon sleeve was wrapped around the gouge and adjacent sliding blocks for the HVR sample assembly. Tests conducted on the PHV apparatus used for the Cascadia core samples show negligible shear stress contributed by the O-rings and Teflon jacket (Fig. A-3a). Tests conducted on the HVR apparatus used for the individual clay species shows that the shear resistance contributed by the Teflon sleeve decreases with displacement from 0.26 to 0.1 MPa (Fig. A-3b). To avoid complex corrections, we have not corrected the data for the contribution of the Teflon sleeve in this study. Although the Teflon sleeve affects the mechanical data, the contribution is almost always less than the gouge and does not affect the calculated values of breakdown stress drop or breakdown work because these values are measured based on relative changes in shear stress.

For each Cascadia core sample, shear stress-normal stress pairs of the initial stress, peak stress, and steady state stress were fit to the equation $\tau = \mu\sigma + b$ to check the shear stress contribution of the O-rings and Teflon jacket (Fig. A-3c). Offsets to the linear fit (b) of the initial and peak stress data for each sample is near zero, suggesting the contribution of friction between the gouge and the Teflon jacket is negligible. Offsets to the linear fit of the steady state shear stress data are non-zero, but we consider this friction to be contributed mainly by viscous shearing within the gouge layer (see Section 2.4). Additionally, any contribution of friction from gouge that was sheared into the space between the upper loading column and the Teflon jacket does not affect the reported values of breakdown stress drop or breakdown work in this work.

A3 Supplemental methods for the data compilation of high velocity friction experiments

High velocity experimental data and estimates of slip weakening distance and fracture energy were compiled from existing literature. This compilation focused on fault gouges, especially clay-bearing gouges, and separated the data into gouge experiments run under wet and dry conditions and intact rock experiments. The compilation included: core samples of input sediments from the Cascadia subduction zone (this study), individual clay species (this study; Faulkner et al., 2011), drill core from the Nankai megasplay (Ujiie and Tsutsumi, 2010) and plate boundary (Ujiie et al., 2013), drill core from the Japan trench (Ujiie et al., 2013), SAFOD core from the San Andreas Fault (French et al., 2014), synthetic smectite-rich gouge (Oohashi et al., 2015), drill core of input sediments from the Costa Rica margin (Vannucchi et al., 2017), drill core of input sediments from the Japan Trench (Sawai et al., 2014), talc gouge (Boutareaud et al., 2012), Nojima Fault gouge (Mizoguchi et al., 2007; Sawai et al., 2012), fault gouge from the Median Tectonic Line (Brantut et al., 2008), Longmenshan fault gouge (Togo et al., 2011), and serpentinite (Hirose and Bystricky, 2007) as well as the experiments on anhydrite gouge, dolomite gouge, gypsum gouge, Carrara marble, dolomite, gabbro, peridotite, and tonalite previously complied by Di Toro et al. (2011).

All experiments in this compilation were run either on the horizontal high velocity rotary shear machine at Kochi/JAMSTEC ("HVR"), the high velocity rotary friction apparatus at Kyoto University, the low to high velocity rotary friction apparatus ("PHV") at Kochi/JAMSTEC, the low to high velocity rotary friction apparatus ("HDR") at Hiroshima University, or the slow to high velocity apparatus ("SHIVA") at the National Institute of Geophysics and Volcanology (INGV). All experiments conducted on intact rock and the majority of gouge experiments were run on the HVR apparatus. Experiments conducted on the HVR, HDR, and Kyoto apparatuses used solid cylinders of rock (sandstone or gabbro) as sample holders. Experiments conducted on the PHV apparatus and SHIVA used impermeable steel ring-shaped sample holders that have a larger diameter than the solid cylinders used on the other machines. This introduces some inconsistency in the permeability of the sample holders, thermal conductivity of the apparatus, and the slip velocity gradient. Additionally, we are unable to evaluate any effects due to differences in the acceleration ramp during experiments because acceleration is often not reported. Previous work on acceleration found that the acceleration path does affect the stress evolution. Faster acceleration rates result in more rapid weakening (i.e., shorter characteristic slip distances) and a higher peak shear stress but does not change the steady state shear stress (Chang et al., 2012; Hirose et al., 2011; Liao et al., 2014; Niemeijer et al., 2011; Sone and Shimamoto, 2009). These combined effects may cancel each other and produce minor changes in the breakdown work (Hirose et al., 2011).

Reported slip weakening distance data was converted to thermal weakening distance to estimate breakdown work. The conventional method for estimating slip weakening distance (D_c) defines a threshold for the reduction of shear stress to 5% of the breakdown stress drop ($\tau_p - \tau_{ss}$), whereas the method for estimating the thermal weakening distance (D_{th}) defines this threshold based on the e-folding distance (a reduction to ~36%). Both models use the same exponential decay curve and the same starting (τ_p) and ending (τ_{ss}) values (Fig. A-5), so D_{th} can be determined from the conventionally reported data. To convert from D_c to D_{th}, the shear stress curve was modeled with reported τ_p, τ_{ss}, and D_c values according to the slip weakening model

$$\tau(\delta) = \tau_{ss} + (\tau_p - \tau_{ss})e^{\frac{\ln(0.05)\delta}{D_c}} \qquad (A-1)$$

Then, the thermal weakening model (Eq. 2-4) was solved at $\delta = D_{th}$ to find the shear stress value

$$\tau(D_{th}) = \tau_{ss} + (\tau_p - \tau_{ss})e^{-\frac{D_{th}}{D_{th}}} \qquad (A-2)$$

Next, D_{th} was determined by finding the slip along the model where $\tau = \tau(D_{th})$. Finally, breakdown work (W_b) was then estimated with the newly converted D_{th} by integrating under the model from zero to $\delta = D_{th}$ (Eq. 2-5).

A4 References

Boutareaud, S., Hirose, T., Andréani, M., Pec, M., Calugaru, D.-G., Boullier, A.M., Doan, M.L., 2012. On the role of phyllosilicates on fault lubrication: Insight from micro- and nanostructural investigations on talc friction experiments. J. Geophys. Res. 117, B08408. https://doi.org/10.1029/2011JB009006.

Brantut, N., Schubnel, A., Rouzaud, J.-N., Brunet, F., Shimamoto, T., 2008. High-velocity frictional properties of a clay-bearing fault gouge and implications for earthquake mechanics. J. Geophys. Res. 113, B10401. https://doi.org/10.1029/2007JB005551.

Chang, J.C., Lockner, D.A., Reches, Z., 2012. Rapid acceleration leads to rapid weakening in earthquake-like laboratory experiments. Science 338, 101-105. https://doi.org/10.1126/science.1221195.

Di Toro, G., Han, R., Hirose, T., De Paola, N., Nielsen, S., Mizoguchi, K., Ferri, F., Cocco, M., Shimamoto, T., 2011. Fault lubrication during earthquakes. Nature 471, 494-498. https://doi.org/10.1038/nature09838.

Faulkner, D.R., Mitchell, T.M., Behnsen, J., Hirose, T., Shimamoto, T., 2011. Stuck in the mud? Earthquake nucleation and propagation through accretionary forearcs. Geophys. Res. Lett. 38, 1-5. https://doi.org/10.1029/2011GL048552.

French, M.E., Kitajima, H., Chester, J.S., Chester, F.M., Hirose, T., 2014. Displacement and dynamic weakening processes in smectite-rich gouge from the Central Deforming Zone of the San Andreas Fault. J. Geophys. Res. Solid Earth 119, 1777-1802. https://doi.org/10.1002/2013JB010757.

Hirose, T., Bystricky, M., 2007. Extreme dynamic weakening of faults during dehydration by coseismic shear heating. Geophys. Res. Lett. 34, L14311. https://doi.org/10.1029/2007GL030049.

Hirose, T., Mukoyoshi, H., Tanikawa, W., Lin, W., Tadai, O., Noda, H., 2011. Frictional response of accreted sediments to seismic slip propagation along subduction plate boundary faults, Abstract T21B-2359 presented at 2011 Fall Meeting, AGU, San Francisco, California.

Liao, Z., Chang, J.C., Reches, Z., 2014. Fault strength evolution during high velocity friction experiments with slip-pulse and constant-velocity loading. Earth Planet. Sci. Lett. 406, 93-101. https://doi.org/10.1016/j.epsl.2014.09.010.

Mizoguchi, K., Hirose, T., Shimamoto, T., Fukuyama, E., 2007. Reconstruction of seismic faulting by high-velocity friction experiments: An example of the 1995 Kobe earthquake. Geophys. Res. Lett. 34, L01308. https://doi.org/10.1029/2006GL027931.

Niemeijer, A., Di Toro, G., Nielsen, S., Di Felice, F., 2011. Frictional melting of gabbro under extreme experimental conditions of normal stress, acceleration, and sliding velocity. J. Geophys. Res. 116, B07404. https://doi.org/10.1029/2010JB008181.

Oohashi, K., Hirose, T., Takahashi, M., Tanikawa, W., 2015. Dynamic weakening of smectite-bearing faults at intermediate velocities: Implications for subduction zone earthquakes. J. Geophys. Res. Solid Earth 120, 1572-1586. https://doi.org/10.1002/2015JB011881.

Poppe, L.J., Paskevich, V.F., Hathaway, J.C., Blackwood, D.S., 2001. A laboratory manual for X-ray powder diffraction. U.S. Geological Survey.

Sawai, M., Hirose, T., Kameda, J., 2014. Frictional properties of incoming pelagic sediments at the Japan Trench: implications for large slip at a shallow plate boundary during the 2011 Tohoku earthquake. Earth Planets Space 66, 65. https://doi.org/10.1186/1880-5981-66-65.

Sawai, M., Shimamoto, T., Togo, T., 2012. Reduction in BET surface area of Nojima fault gouge with seismic slip and its implication for the fracture energy of earthquakes. J. Struct. Geol. 38, 117-138. https://doi.org/10.1016/j.jsg.2012.01.002.

Sone, H., Shimamoto, T., 2009. Frictional resistance of faults during accelerating and decelerating earthquake slip. Nat. Geosci. 2, 705-708. https://doi.org/10.1038/ngeo637.

Tanikawa, W., Mukoyoshi, H., Tadai, O., 2012. Experimental investigation of the influence of slip velocity and temperature on permeability during and after high-velocity fault slip. J. Struct. Geol. 38, 90-101. https://doi.org/10.1016/j.jsg.2011.08.013.

Togo, T., Shimamoto, T., Ma, S., Hirose, T., 2011. High-velocity frictional behavior of Longmenshan fault gouge from Hongkou outcrop and its implications for dynamic weakening of fault during the 2008 Wenchuan earthquake. Earthquake Science 24, 267-281. https://doi.org/10.1007/s11589-011-0790-6.

Tsutsumi, A., Shimamoto, T., 1997. High-velocity frictional properties of gabbro. Geophys. Res. Lett. 24, 699-702. https://doi.org/10.1029/97GL00503.

Ujiie, K., Tanaka, H., Saito, T., Tsutsumi, A., Mori, J.J., Toczko, S., Expedition 343 and 343T Scientists, 2013. Low coseismic shear stress on the Tohoku-Oki megathrust determined from laboratory experiments. Science 342, 1211-1214. https://doi.org/10.1126/science.1243485.

Ujiie, K., Tsutsumi, A., 2010. High-velocity frictional properties of clay-rich fault gouge in a megasplay fault zone, Nankai subduction zone. Geophys. Res. Lett. 37, L24310. https://doi.org/10.1029/2010GL046002.

Vannucchi, P., Spagnuolo, E., Aretusini, S., Di Toro, G., Ujiie, K., Tsutsumi, A., Nielsen, S., 2017. Past seismic slip-to-the-trench recorded in Central America megathrust. Nat. Geosci. 10, 935-940. https://doi.org/10.1038/s41561-017-0013-4.

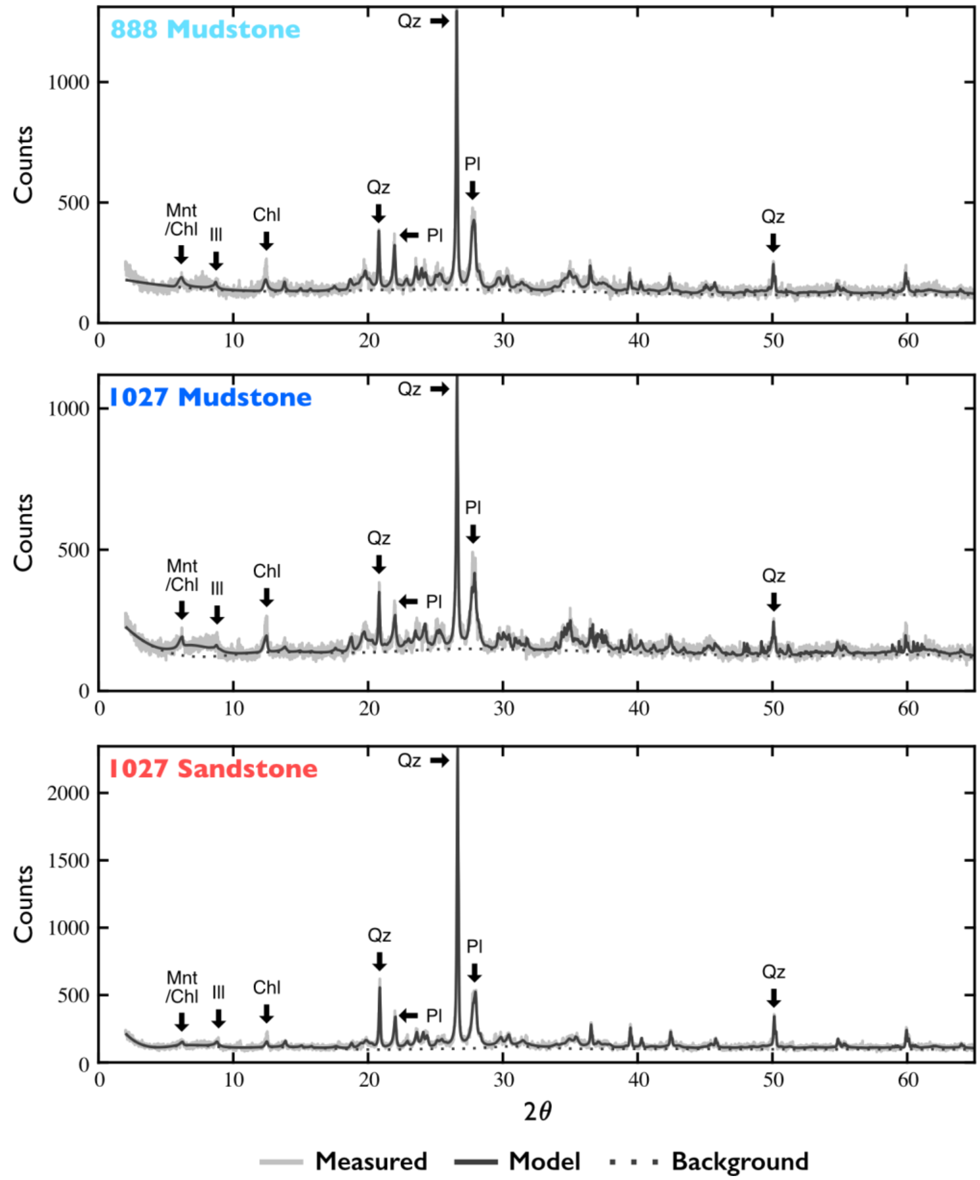

Figure A-1: Composition of Cascadia core samples. X-ray diffraction (XRD) spectra from random powder mounts prepared from the whole rock showing mineralogy identified based on characteristic d-spacings at a given 2θ (indicated with arrows). Quartz (Qz), plagioclase (Pl), montmorillonite (Mnt), chlorite (Chl), and illite (Ill) were identified in all three samples.

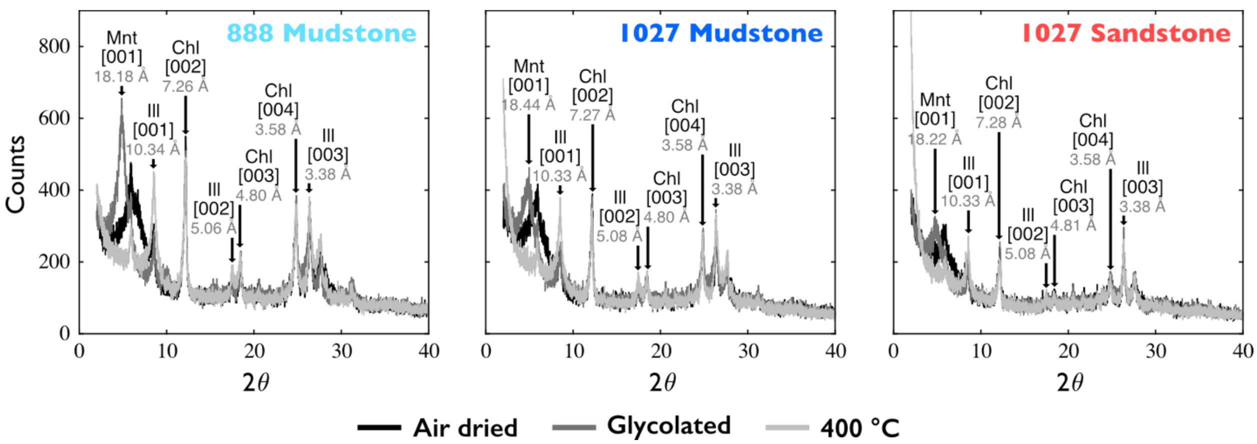

Figure A-2: Clay fraction of Cascadia core samples. X-ray diffraction (XRD) spectra from oriented mounts prepared from the clay fraction. Data was collected after samples were air dried (black line), glycolated (dark grey line), and heated to 400°C (light grey line). Clay minerals are identified based on characteristic d-spacings determined by the spacing width in ångstroms (indicated by labelled arrows). Montmorillonite (Mnt), chlorite (Chl), and illite (Ill) were identified in all three samples.

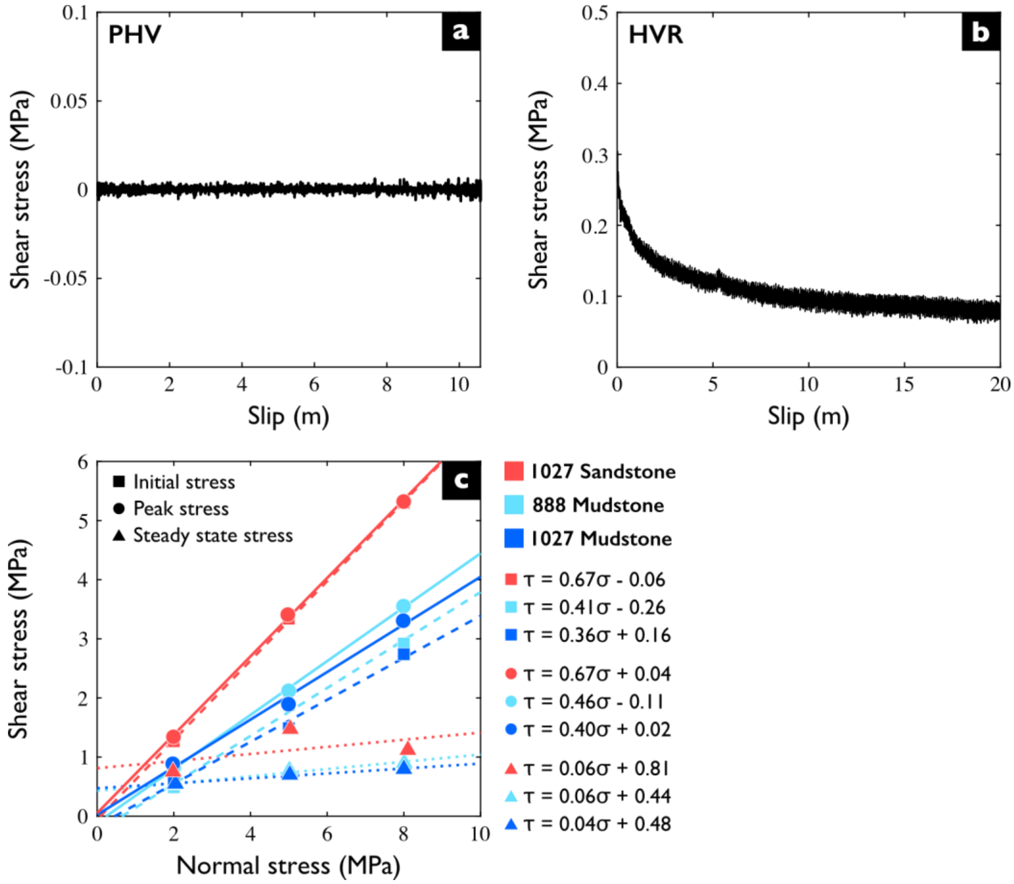

Figure A-3: Negligible contribution of Teflon to friction during experiments. Mechanical data from experiments conducted without gouge material, without applied normal stress, and with a gap between the sliding blocks to test the mechanical contribution of Teflon present in the sample assembly. **(a)** Test conducted on the low to high velocity rotary shear apparatus (PHV) used for the Cascadia core samples shows negligible shear stress contributed by the Teflon O-ring. **(b)** Test conducted with a Teflon sleeve (2 mm length) on the high velocity rotary shear apparatus (HVR) used for the individual clay species shows that the resistance contributed by the Teflon sleeve is almost always less than the gouge, so the contribution of the Teflon sleeve is negligible. **(c)** For each of the Cascadia core samples, shear stress-normal stress pairs for the initial stress (τ_0) during v_e = 500 µm/s (squares and dashed lines), peak stress (τ_p) (circles and solid lines), and steady state stress (τ_{ss}) (triangles and dotted lines) are fit with a linear equation and listed in the format $\tau = \mu\sigma + b$, where μ represents the friction coefficient.

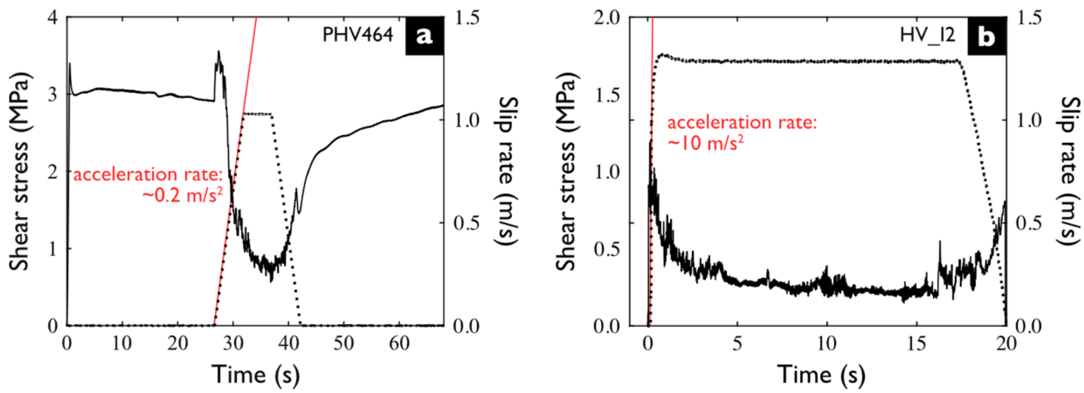

Figure A-4: Velocity and acceleration paths during experiments. **(a)** Mechanical data (solid black line) and slip rate (dotted black line) from experiment PHV464. The acceleration ramp has a rate of ~0.2 m/s^2. **(b)** Mechanical data (solid black line) and slip rate (dotted black line) from experiment HV_I2 (dry illite). The acceleration ramp has a rate of ~10 m/s^2.

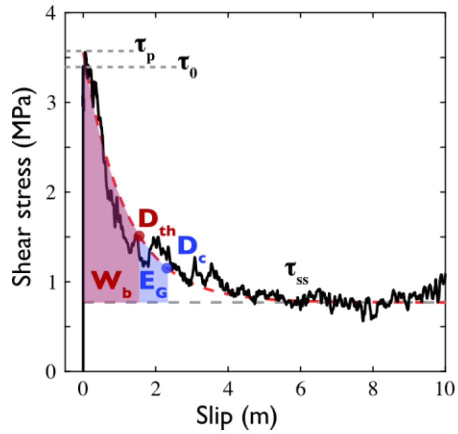

Figure A-5: Conversion of slip weakening distance (D_c) to thermal weakening distance (D_{th}). Mechanical data (black solid line), model of shear stress evolution (red dashed line), residual shear stress (grey dashed line), and slip rate (black dotted line). τ_0 is the initial shear stress before the acceleration ramp, τ_p is the peak shear stress after acceleration begins, and τ_{ss} is the steady state shear stress achieved during slip at 1 m/s. Blue shaded area represents the fracture energy (E_G) estimated from the model between slip at the onset of acceleration and D_c. Red shaded area represents the breakdown work (W_b) estimated from the model between slip at the onset of acceleration and D_{th}. Red shaded area appears purple due to the overlap with the blue shaded area. Thermal weakening distance can be determined from D_c, τ_p, and τ_{ss} using Eq. A-1 and A-2.

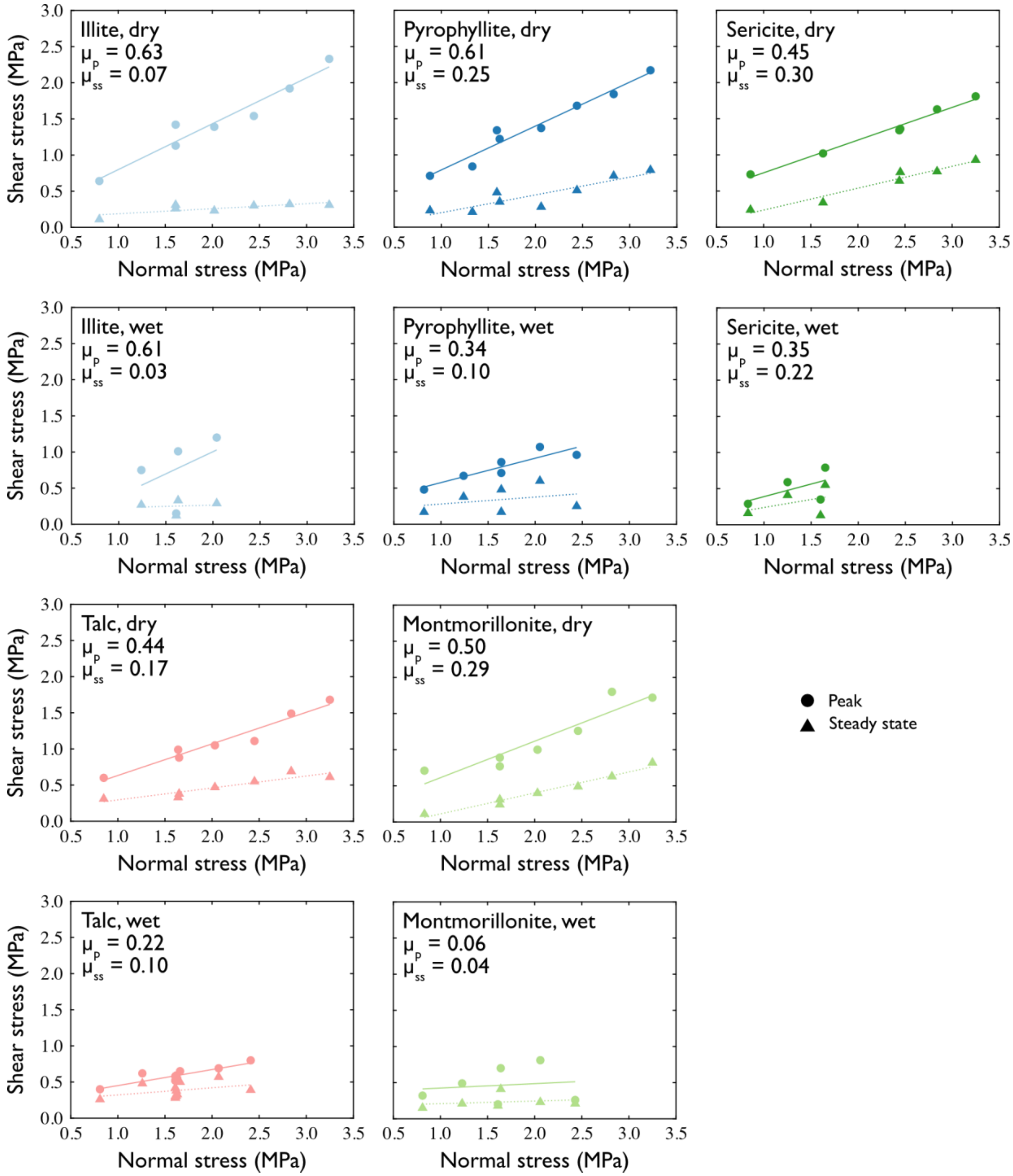

Figure A-6: Friction coefficients of individual clay species. Shear stress scaling with normal stress for peak shear stress (circles) and steady state shear stress (triangles). Friction coefficients for each sample are defined as the linear scaling between shear stress and normal stress and are determined from the peak shear stress (solid lines) and steady state shear stress (dotted lines).

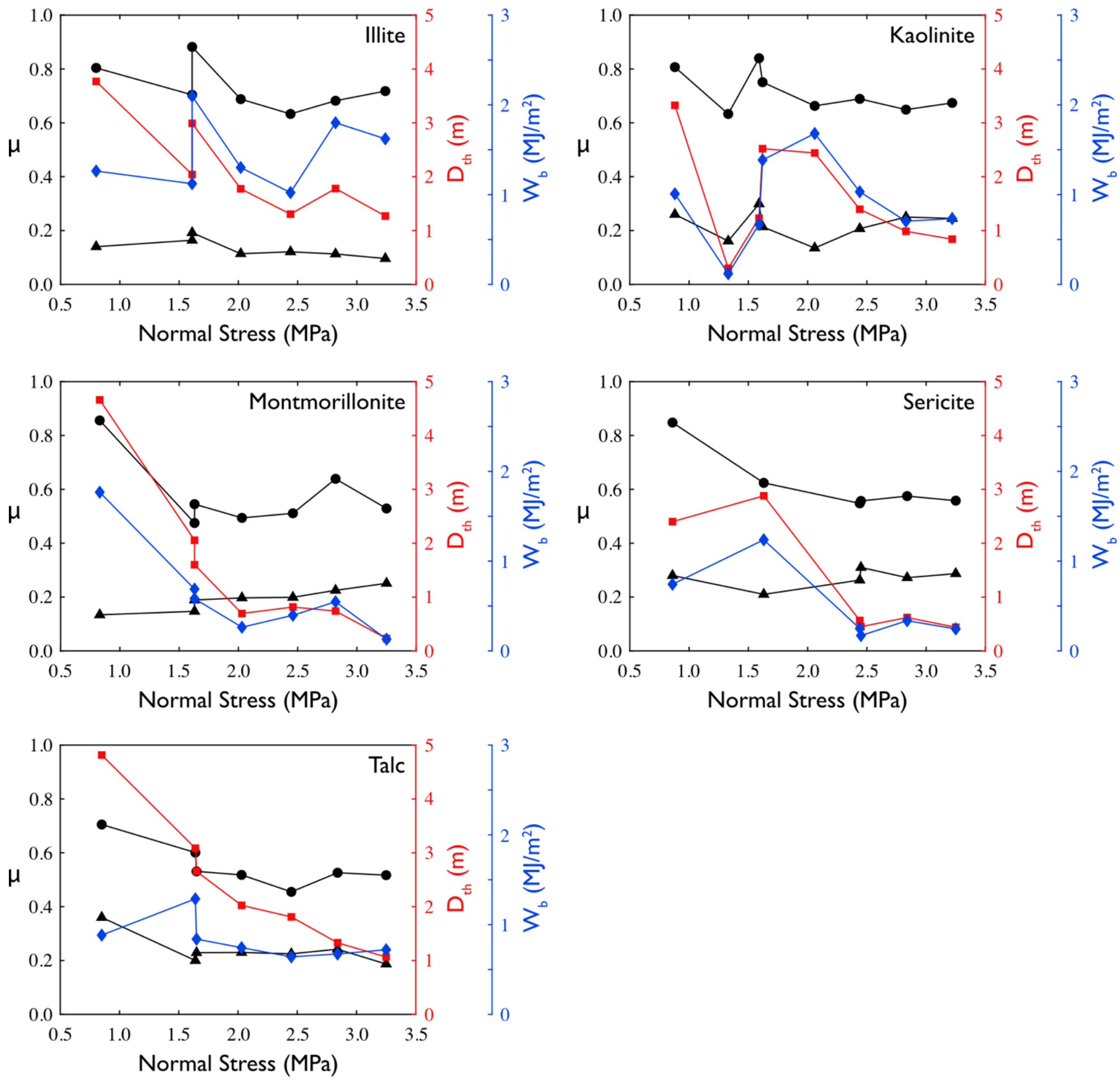

Figure A-7: Friction and fracture energy parameters from experiments conducted on individual clay species under dry conditions.

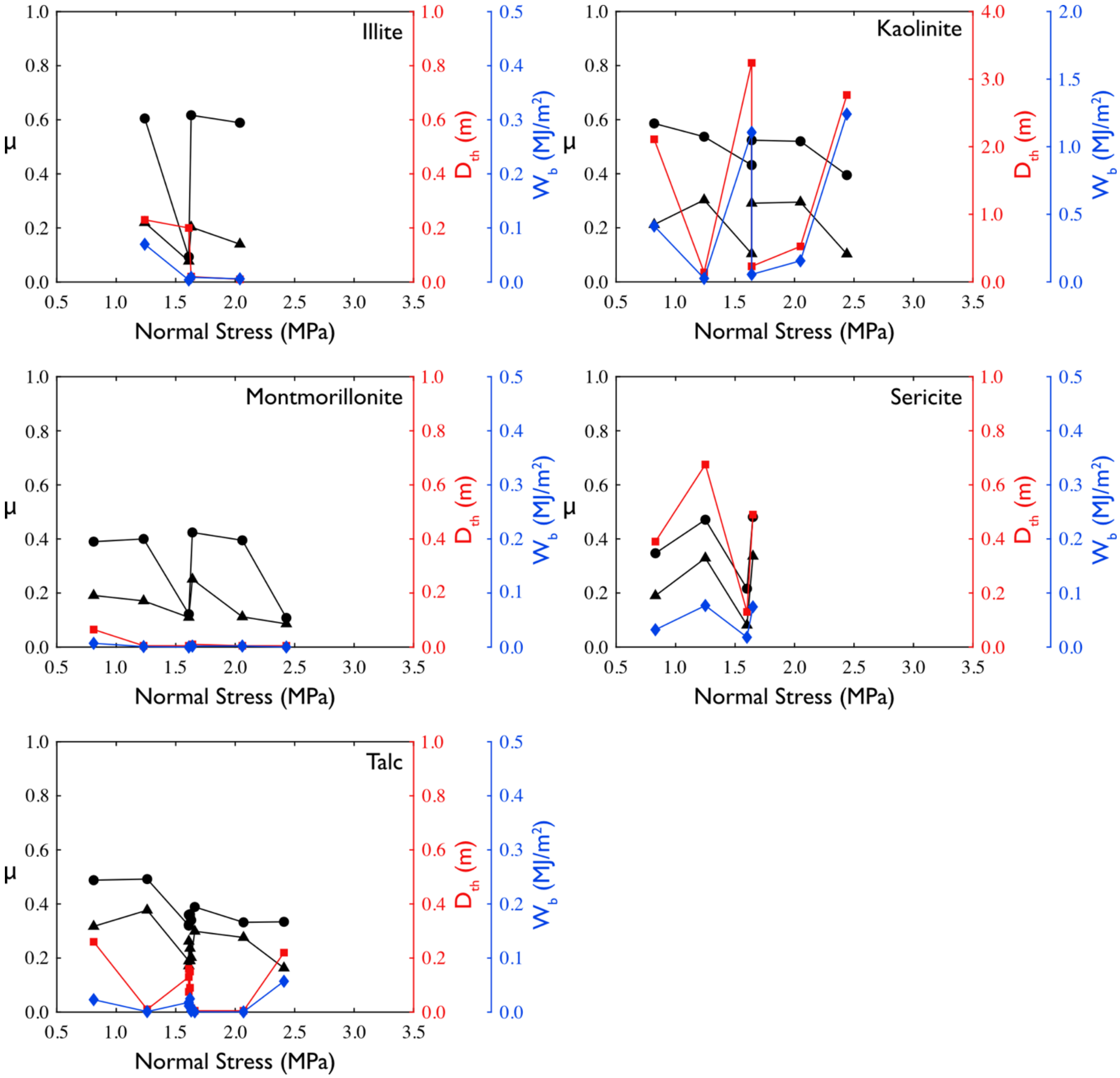

Figure A-8: Friction and fracture energy parameters from experiments conducted on individual clay species under wet conditions.

Table A-1: Composition of core samples from Cascadia from XRD analysis and Rietveld refinement

Sample	Qz (%)	Fsp (%)	Clays (%)
888B-62X-2	20	35	45
1027B-03H-3	30	35	35
1027B-53X-2	20	35	45

Table A-2: Composition of individual clay species samples from XRD analysis

Sample	Purity	Other components	Supplier/source
Illite	44%	Quartz 31%, calcite 24%, chlorite 1%	Peach Pig illite clay, Japan
Pyrophyllite	49%	Quartz 32%, kaolinite 14%, muscovite 5%	Nakarai Chemicals, Japan
Montmorillonite	77%	Quartz 15%, albite 8%	Na-bentonite, Yamagata Prefecture, Japan
Sericite	85%	Calcite 13%, chlorite 2%	JCSS-5101, Japan
Talc	88%	Chlorite 9%, quartz 2%, dolomite 1%	J.T. Baker, USA

Table A-3: Compilation of laboratory data from high velocity rotary shear experiments

This table is deposited in the OSF data repository at: https://osf.io/gj8u2/

APPENDIX B

Supplementary Materials for Chapter 3

This supplement includes supplementary figures and tables for mineral composition EPMA analyses, zircon U-Pb analyses, and additional photomicrographs of the Jordan River unit.

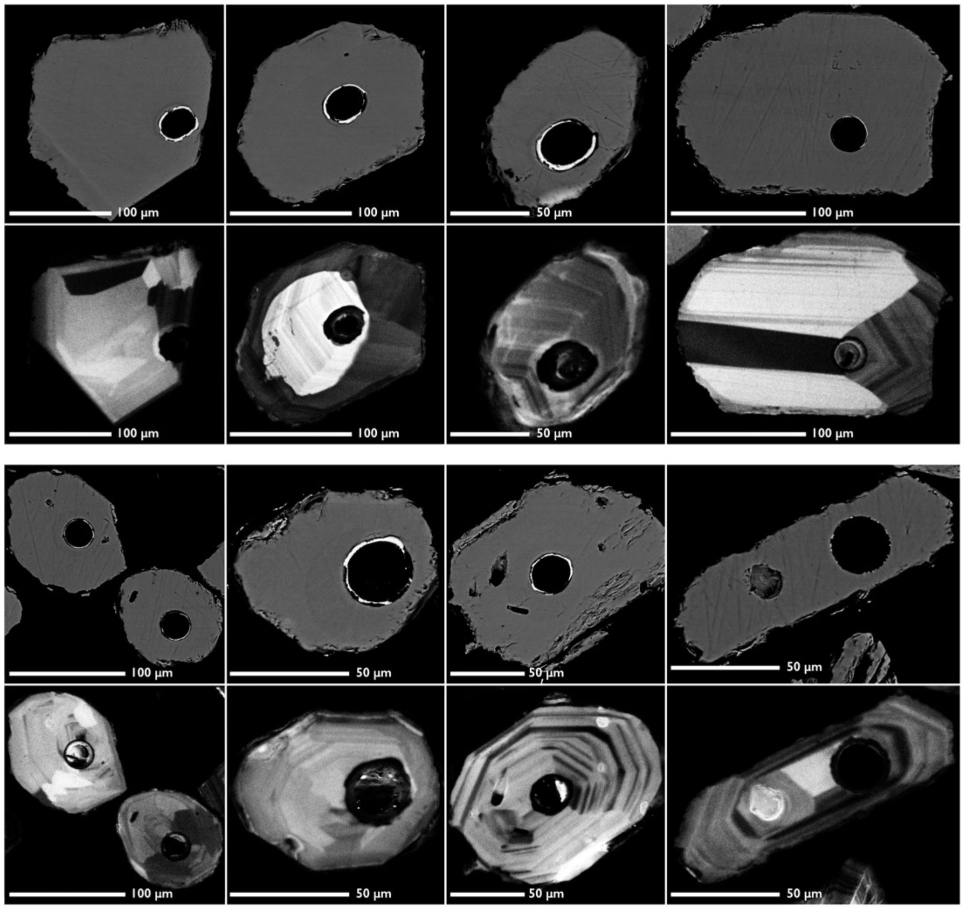

Figure B-1: Backscattered electron and cathodoluminescence images for a subset of zircon grains analyzed for U-Pb geochronology.

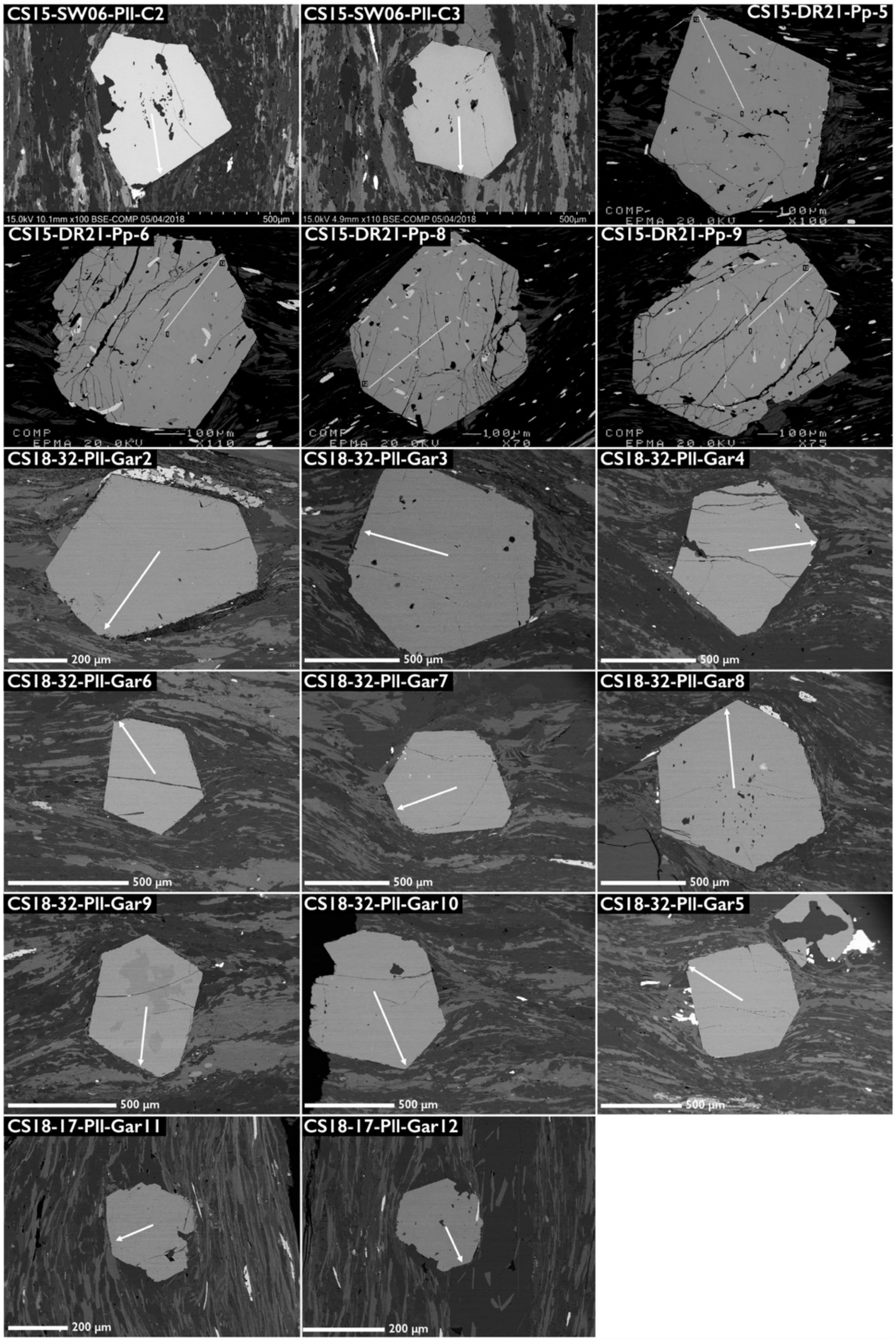

Figure B-2: Transect locations across garnet grains with spots ~30 µm apart.

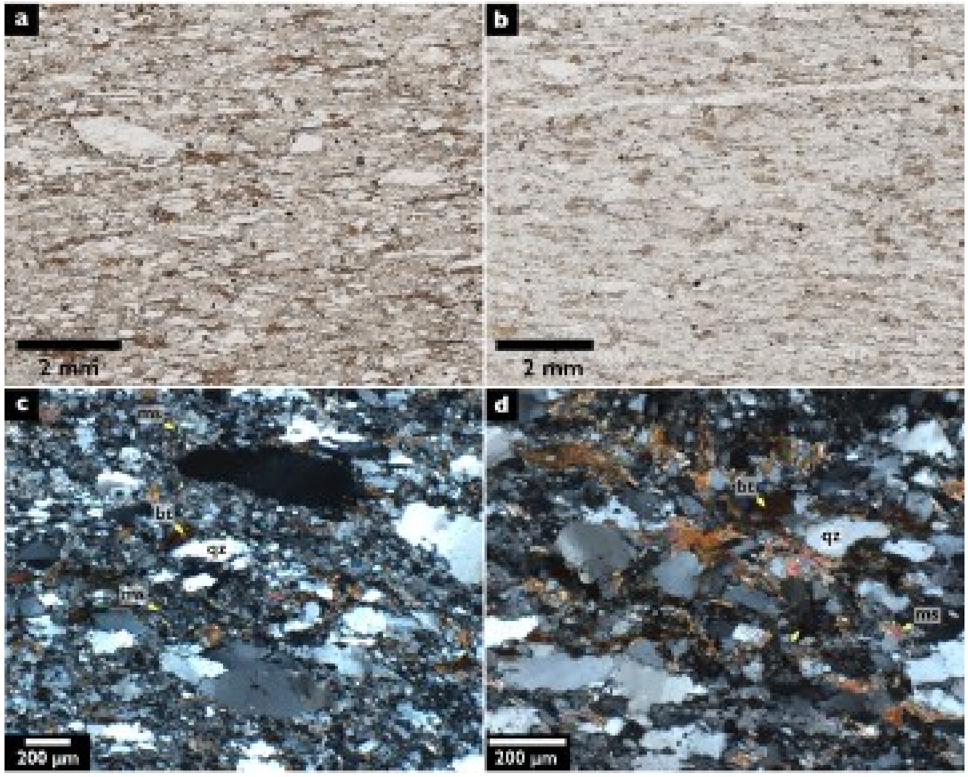

Figure B-3: Photomicrographs of the Jordan River unit in the Leech River Complex.

Table B-1: Garnet compositions determined from EPMA analyses

This table is deposited in the OSF data repository at: https://osf.io/2px6w/

Table B-2: Biotite compositions determined from EPMA analyses

This table is deposited in the OSF data repository at: https://osf.io/2px6w/

Table B-3: Amphibole compositions determined from EPMA analyses

This table is deposited in the OSF data repository at: https://osf.io/2px6w/

Table B-4: Plagioclase compositions determined from EPMA analyses

This table is deposited in the OSF data repository at: https://osf.io/2px6w/

Table B-5: Zircon U-Pb ages

This table is deposited in the OSF data repository at: https://osf.io/f7bv4/